Polarized Proton Capture on Tritium at Proton Energies below 80 KeV

by

Richard Shane Canon

Department of Physics
Duke University

Date

Approved:

Henry R. Weller, Supervisor

Berndt Mueller

Calvin Howell

Vladimir Litvinenko

Stephen Teitsworth

Dissertation submitted in partial fulfillment of
the requirements for the degree of
Doctor of Philosophy in the Department of
Physics in the Graduate School
of Duke University

2001

Abstract

(Physics – TUNL)

Polarized Proton Capture on Tritium at Proton Energies below 80 KeV

by

Richard Shane Canon

Department of Physics
Duke University

Date

Approved:

Henry R. Weller, Supervisor

Berndt Mueller

Calvin Howell

Vladimir Litvinenko

Stephen Teitsworth

An abstract of a dissertation submitted in partial
fulfillment of the requirements for the degree
of Doctor of Philosophy in the Department
of Physics in the Graduate School
of Duke University

2001

Abstract

A Study of Polarized Proton Capture on Tritium at Low Energies

The ^{3}H$(\vec{\mathrm{p}},\gamma)^4$He reaction was studied at energies below $E_p = 80$ keV at Triangle Universities Nuclear Laboratory (TUNL) using the polarized ion source. The current study was the logical progression of a previous study of the ^{2}H$(\vec{\mathrm{p}},\gamma)^3$He reaction done by the radiative capture group at TUNL. One result from that study was the recognition of the importance of meson exchange currents (MEC) in that reaction. In fact, theoretical calculations have shown that approximately 50% of the magnetic dipole transition strength observed in that reaction at $E_p = 80$ keV can be attributed to MECs. The contribution of MECs to the M1 strength in the ^{3}H$(\vec{\mathrm{p}},\gamma)^4$He reaction at very low energies is expected to be even stronger.

The use of a polarized proton beam allows for the observation of the analyzing power in this reaction. The angular distribution of the cross section, $\sigma(\theta)$, and the analyzing power, $A_y(\theta)$, were measured at incident proton beam energies of 40 keV and 80 keV. In both cases the beam was stopped in the target. The angular distribution in the cross section and analyzing power were fit to a Legendre and Associated Legendre polynomial expansion, respectively. A transition matrix element analysis,

which expands all of the observables as a set of amplitudes and phases, was performed on the data as well. The magnetic dipole transition strength was determined from this analysis. The explicit MEC effects are contained in this strength. By comparing this strength with similar reactions in the case of three-bodies, we are able to interpret the MEC origin of this strength.

In addition, the absolute cross section has been determined. A parameterization of the Astrophysical S-factor, which factors out the rapidly varying effects due to the Coulomb potential from the cross section, has been performed. Previous measurements of the absolute cross section extended down to beam energies of 100 keV. The present study extends the measured cross section data closer to zero energy and, therefore, makes the extrapolation into the energy regime typically of interest to astrophysicists more reliable.

Finally, this reaction can be used as a source of 20 MeV γ-rays. A reliable measurement of the cross-section at low energies will be very useful in future designs of sources using high-voltage power supplies to accelerate the proton beam.

Acknowledgements

During my graduate "career" I have relied on the help and assistance of many people who I am deeply indebted. My advisor, Henry Weller, helped direct and assist me in all aspects of the project. One only needs to look at the multiple iterations of my thesis to grasp his patience. John Dunham, Richard O'Quinn, Paul Carter, Sidney Edwards, and Patrick Mulkey's efforts to keep the source running, equipment functioning, and modules operating are extremely appreciated.

I will always have fond memories of Duke and this is entirely due to the graduate students, post-docs, and faculty that I encountered there. Bryan Rice and Mark Godwin taught me how to have an upbeat outlook on things. Eric Wulf and Eric Schreiber always made things interesting. Steve Nelson, Konstantin Sabourov, and Brendan Crowley stuck with me until the bitter end. I was also fortunate to have the assistance of great post-docs, John "Ned" Kelley and Sally Gaff. The "Georgia boys", Dick Prior and Mark Spraker, were always there in a pinch. And Dr. Tilley seemed willing to sit even the worst shifts. Far beyond the technical expertise that each of these individuals offered, I appreciate there friendship.

Finally I want to thank those who provided personal support and motivation: my wife, daughter, and parents. Stephanie deserves a title for the seven years as a graduate student spouse. She already has my complete respect and admiration. Finally, I want to thank my parents. Even when my choices have differed from their own wishes, they have still given me their support and encouragement. I hope that I provide the same for my daughter, Rachel.

Contents

List of Figures

List of Tables

Chapter 1

Introduction

A description of the experimental study of the $^3\mathrm{H}(\vec{\mathrm{p}},\gamma)^4\mathrm{He}$ reaction at low energies by the Triangle Universities Nuclear Laboratory (TUNL) radiative capture group will be given in this thesis. There were several motivating factors for this study. First, a study of this reaction is a logical progression of previous work done by the radiative capture group. Secondly, *ab initio* calculations of nuclei are beginning to progress beyond three-body reactions. The present reaction, especially at low energies, could provide an early testing ground for the capture aspects of these theories. Finally, from an application perspective, this reaction can be used as a source of moderate energy γ-rays. A better understanding of the cross section at low energies is important in developing this type of source. In this chapter an explanation of these points will be given. In addition, an outline of the goals of this experiment will be presented. Finally, a brief description of the chapters will be given.

1.1 Background

1.1.1 The ^{3}H(p, γ)^{4}He reaction

The radiative capture of protons on tritium at the very low energies of the present study is expected to proceed primarily via electric dipole (E1) radiation. Since the channel spin for the incoming channel is either S=0 or S=1, and since the intrinsic parity of the channel is even, the formation of an intermediate state having $J^\pi = 1^-$ requires that the capture occurs in a p-wave (l=1) state. Furthermore, since the dominant E1 transition has $\Delta S = 0$, this state will have S=0, since the ground state of ^{4}He is primarily S=0. In addition to this p-wave (E1) capture strength, some s-wave capture is expected. This can give rise to an intermediate state having $J^\pi = 0^+$ (l=0, S=0) or 1^+ (l=0, S=1). The former is forbidden to γ-decay to the ground state (0^+), while the 1^+ state will decay via magnetic-dipole radiation (M1) to the ground state. We therefore expect the γ-rays produced via the capture of 80 keV protons on tritium to be a mixture of E1 and M1 multi-polarities.

The Q-value of the reaction is 19.8 MeV, so the γ-ray energy in the case of an 80 keV proton beam is 19.86 MeV. This is well above the energy of typical terrestrial background sources. Therefore, only cosmic ray background will contribute substantially to the background. At the energies of the present study, the capture reaction is the only open channel beside elastic scattering. The threshold for the ^{3}H(p,n)^{3}He reaction is close to 1.0 MeV. As a result, there is no additional background generated by the interaction of the proton beam with the tritium target. Finally, based on extrapolations from previous measurements performed at higher energies, the cross section for the reaction is quite large compared to other proton capture reactions at similar energies.

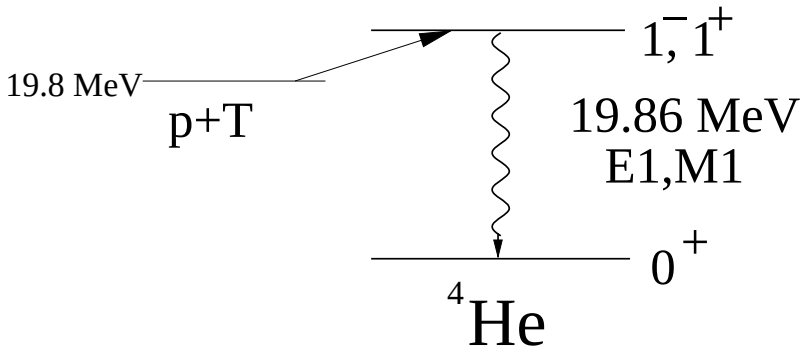

Figure 1.1: A level diagram illustrating proton capture on tritium decaying to the ground state of ^{4}He.

1.1.2 TUNL Radiative Capture Group

During the past decade, the TUNL radiative capture group has performed detailed studies of few-body capture reactions at low energies. Radiative capture reactions encompass the group of reactions that involve an incident particle being captured by a target nucleus and subsequently emitting electromagnetic radiation. These reactions play critical roles in astrophysical processes such as stellar evolution and big bang nucleosynthesis. Also, these reactions can provide rigorous testing grounds for few-body theories.

TUNL's unique capabilities and resources are well suited to performing these types of studies. Specifically, TUNL's atomic beam polarized ion source (ABPIS) has made many of these studies possible since it is capable of delivering relatively high beam current with high polarization. The ABPIS's ability to deliver both polarized protons and deuterons has also been important. For example, this allowed a complete set of polarization measurements to be made for the ^{1}H$(\vec{\mathrm{d}},\gamma)^3$He and ^{2}H$(\vec{\mathrm{p}},\gamma)^3$He reaction [Wul99a]. The results from that study have provided a fertile testing ground for developing few-body theories and have raised interesting questions

about the underlying dynamics [Wul99b].

1.1.3 Few-body physics

Modern few-body theories predominantly attempt to extend realistic nucleon-nucleon (NN) potentials to systems with more than two nucleons. Many of these approaches have only recently become feasible with the advent of faster computers.

Theorists have developed sophisticated two-body potentials that accurately describe a large body of two-nucleon reactions. The potential often has an electromagnetic part, a one-pion exchange part, and a phenomenological part which contains intermediate- and short-range terms [Wir95]:

$$v(r) = v^{em}(NN) + v^{\pi}(NN) + v^{R}(NN) \tag{1.1}$$

The potentials are typically parameterized and these parameters are adjusted to fit a large body of NN scattering data. While these potentials could successfully describe NN reactions, an obvious question is whether or not these potentials can also describe more complicated reactions.

Extending the NN potential model to systems with more than two nucleons is difficult and ultimately fails to fully reproduce experimental data [Fri91]. Faddeev provided the first description of an approach to extending the NN potential models to a three-body system [Fad60]. This approach results in the construction of three coupled equations. When theorists attempted to employ this approach with the already existing NN potentials for three-body systems, problems were immediately encountered. The most serious discrepancy being that the theories under-predicted the bound-state binding energies of ^{3}H and ^{3}He by about 10% [Fri91].

In order to resolve this discrepancy theorists added a nuclear three-body force

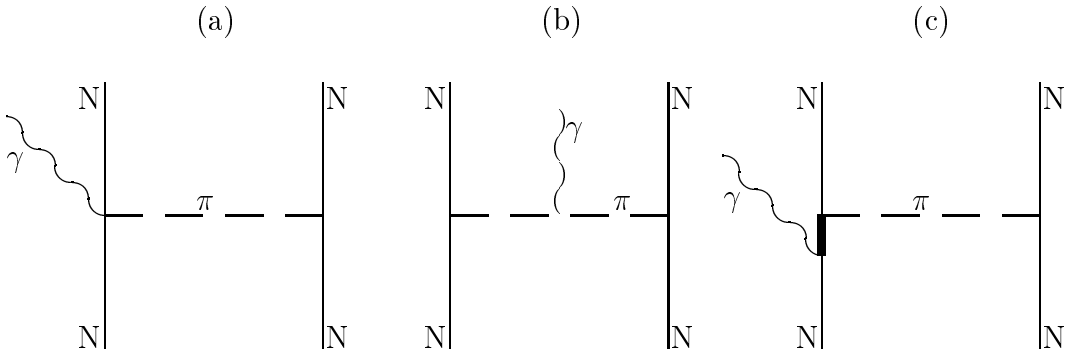

Figure 1.2: Relevant pion-exchange processes for three nucleon reactions [Wul99a, Tor83].

(TBF) [Coo79, Coe83]. The concept of a TBF was not a radical idea. The basic idea is that if the presence of a third body alters the force between the other two, then we have a three-body force. Classic examples of TBF already existed, with perhaps the most familiar example being the earth-moon-satellite system, where the presence of the moon distorts the shape of the earth due to tidal forces. The exact orbit of the satellite will be different as a result of this distortion. Note that if one includes the tidal effect explicitly, then there is no need for a three-body force. Therefore we see that the existence of a three-body force is connected to freezing certain degrees-of-freedom. In the nuclear system the nucleons have internal states which can be excited, which is the nuclear analog to the distortion of the earth. By adding models based on pion exchange mechanisms (see Figure 1.2) to the existing NN potentials theorists were able to accurately reproduce the three-body bound state binding energies [Fri91].

Having resolved the binding energy problem, the next question is how well can the theories describe other three-body reactions such as scattering, break-up, and capture reactions. Here the improved theories have encountered problems. Perhaps the most dramatic discrepancy is in the vector analyzing power for n-d scattering.

Although calculations can accurately reproduce unpolarized observables, as well as tensor analyzing powers, these same calculations consistently under-predict the vector analyzing power ($A_y(\theta)$). This problem has been termed the "A_y Puzzle." Discrepancies have also been noted in the deuteron vector analyzing power, iT_{11}, for a vector polarized deuteron scattering off a nucleon.

While there has been some speculation on solutions to this problem, some of which show great promise, the theoretical community has yet to reach a consensus. One possibility which was considered was attempting to make small modifications to the NN potential which would allow it to still fit the two-body NN data and simultaneously fit the three-body scattering data. However, an analysis concluded that the NN potentials could not be changed in such a way as to allow it to reproduce both sets of data [Hüb98] . In [Hüb98], it was concluded that an explicit three-body force effect should be examined to resolve the problem.

1.1.4 Lessons from the Study of p-d Capture and Other Reactions

Several lessons learned from the study of the $^2H(p,\gamma)^3He$ reaction can be useful in the study of the $^3H(p,\gamma)^4He$ reaction. The two most relevant lessons are the importance of meson exchange currents and the determination of the phase shifts.

Meson Exchange Currents

The final states of the $^2H(p,\gamma)^3He$ and $^2H(n,\gamma)^3H$ reactions are eigenfunctions of the one-body M1 operator which is used in the impulse approximation (IA). This is simply a result of the M1 operator in the IA only depending on the magnetic moments

and orbital motion of the nucleons [Sch37]. Therefore when the one-body M1 operator operates on the final state wave functions, the radial wave functions are unchanged except for some multiplicative factors. As a result, the contribution from this operator is simply the overlap of the initial and final state wave functions. Since the initial and final states are quasi-orthogonal, the result is very small. However, two-body currents can give rise to M1 radiation. As a result, meson exchange currents, a type of two-body current, become very important in determining the M1 part of the cross section in these reactions.

Studies of the ^{2}H(n, γ)^{3}H reaction at thermal energies (E$\sim$0) have revealed large effects due to MECs. At very low energies neutron capture reactions become almost exclusively s-wave (in this case, s-wave capture implies an M1 transition). As mentioned above, the contribution to the M1 strength from one-body currents is greatly quenched. Therefore the MEC effects should be more noticeable. Furthermore, the cross section becomes very large, nearly 0.25 b, at thermal energies. These factors, taken together, have made this one of the most thoroughly studied three-body reactions involving MEC effects. Theoretical studies have shown that by including MEC effects, there is nearly a factor of two enhancement in the cross section at thermal energies [Fri90, Tor83].

Fewer attempts have been made to observe the same effects in the charged particle capture reactions for A=3. This is due to the fact that the ^{2}H(p, γ)^{3}He reaction, for example, is both more difficult to measure and to calculate theoretically. These difficulties can be attributed to Coulomb effects, since the Coulomb repulsion reduces the cross section at low energies and the Coulomb interaction introduces convergence issues in theoretical methods. These factors also impact studies of the ^{3}H(p, γ)^{4}He reaction.

The ^{3}H(p,γ)^{4}He reaction is expected to exhibit these same MEC effects at very low energies. Like the ^{2}H(p,γ)^{3}He and ^{2}H(n,γ)^{3}H reactions, the final state of the ^{3}H(p,γ)^{4}He reaction is an eigenfunction of the one-body M1 operator. In fact, in studies of the ^{3}He(n,γ)^{4}He reaction, which the ^{3}H(p,γ)^{4}He reaction should resemble, this quenching of the contribution from one-body currents to the M1 strength ($\sim$90%) is even more manifest. Nearly all of the M1 strength has been attributed to MEC in the ^{3}He(n,γ)^{4}He reaction [Car90]. Therefore, MECs are expected to contribute even more strongly to the M1 strength in the ^{3}H(p,γ)^{4}He reaction in comparison to the ^{2}H(p,γ)^{3}He reaction.

Watson's Theorem and Coulomb Phases

Another lesson learned from the ^{2}H(p,γ)^{3}He study involved determining the phases for the capture reaction. Watson's Theorem states that a relationship can be made between the phases of a capture reaction and phase shifts from elastic scattering [Wat54]. The relationship is derived from the S-matrix and time-reversal invariance. The phases, ϕ, of the capture reaction are seen in the transition matrix element (TME) representation of the reaction which represents the reaction as a set of amplitudes and phases, $|R|e^{i\phi}$. The "observables" (cross section, analyzing power, etc) are written as expansions in terms of Legendre and Associated Legendre polynomials. The coefficients of these expansions can be written in terms of the amplitudes and relative phases of the contributing TMEs. These phases are varied along with the amplitudes to fit the experimental data. For the ^{2}H(p,γ)^{3}He and ^{3}H(p,γ)^{4}He reactions at low energies, the only open inelastic channel is radiative capture. Therefore, the relative phases of the capture TMEs can be determined from the scattering phase shifts and the mixing parameter, which describes mixing between different scattering

amplitudes[Knu99]. At low energies the mixing is strongly reduced, so the difference in the scattering phase shifts between different partial waves will yield the relative capture phases. Note that the observables in a capture reaction depend only on the relative phases of the matrix elements involved, so the absolute values of the phases are arbitrary.

The full utility of this theorem is somewhat reduced due to the lack of scattering measurements done at these low energies. However, in an experimental study of the ^{2}H(p,γ)^{3}He reaction the capture phases were found to be almost entirely due to the Coulomb term [Wul99a]. One can express the phases in terms of a Coulomb contribution and a nuclear contribution, where the first is the portion of the phase that comes from the presence of the Coulomb potential and the latter is everything else. When this is done, it was found in the case of the ^{2}H(p,γ)^{3}He reaction that the nuclear portion was extremely small ($\leq 0.5^\circ$), which is well beyond the sensitivity of most experimental studies. Therefore, the phases should be predominantly determined by the Coulomb portion which is on the order of tens of degrees. This portion can be easily determined and calculated by the following approximation which describes the phase shifts for a point charge Coulomb potential, [McC68],

$$\sigma_l - \sigma_0 = \sum_{s=1}^{l} \tan^{-1} \frac{\eta}{s}, \tag{1.2}$$

where η is the Sommerfeld parameter (see Equation 2.2 later). An extraction of the relative phases directly from the ^{2}H(p,γ)^{3}He data [Wul99a] using an unconstrained TME fit to the data found excellent agreement with the phases calculated assuming a point charge Coulomb potential. The ^{3}H(p,γ)^{4}He reaction is expected to behave in a similar manner. The study of the ^{2}H(p,γ)^{3}He reaction resulted in an abundance of measured observables which allowed for a less constrained TME analysis. Angular distributions in the cross section, analyzing power, and several tensor analyzing powers

were obtained. Unfortunately, this will not be the case for the ^{3}H(p, γ)^{4}He reaction, since only the angular distribution in the cross section and the vector analyzing power can be measured. Therefore, it will be necessary to rely on some well tested assumptions, such as using the Coulomb phase, to constrain the TME fit, in order to perform an accurate analysis.

1.2 Previous Measurements

While the ^{3}H(p, γ)^{4}He reaction has been studied experimentally in the past, most of these studies have been performed at higher energies. Furthermore, the few low-energy measurements that exist used unpolarized beams. Therefore the new measurements should provide important new details, as well as verifying and extending aspects of previous measurements.

Throughout the 1980s and early 1990s, the ^{3}H(p, γ)^{4}He reaction received attention because of differences between theory and experiment in the ratio of the cross sections for the ^{4}He(γ, p)^{3}H and ^{4}He(γ, n)^{3}He reactions, R_γ. Since the p-T capture reaction is the inverse of the photo-disintegration of ^{4}He into $p+^3$H, the reactions are simply related by detailed balance [Roy67]. While the non-charge-symmetry breaking models yielded an $R_\gamma \sim 1.1$, an analysis of the data available at the time by Calarco *et al* [Cal83] yielded a value varying between 1.7 and 1.2 over the excitation energy range between 25-35 MeV. An implication of this result was a non-zero charge symmetry breaking term in the nuclear force. Later measurements of both the capture and photo-disintegration reactions obtained results that were closer to the conventional theoretical result of 1.1, thus obviating the need for charge-symmetry breaking in ^{4}He. However, some debate still continues, as not all of the discrepancies have been

explained. Unfortunately, the results from this experiment may not provide any additional insight into this question, since most of the discrepancies occur at excitation energies above those of the current experiment.

While many of the measurements of the ^{3}H(p,γ)^{4}He reaction which addressed questions about R_γ were performed at high energies, a measurement by Hahn *et al* did extend down to proton energies as low as 100 keV [Hah95]. In addition, older measurements by Perry and Bame [Per55] and a more recent measurement by Poon [Poo91] also exist. The beam energies for these measurements extended down to 100 keV and 30 keV, respectively. However, all of the measurements were performed with unpolarized beams, therefore no analyzing power measurements exist for this reaction at low energies (less than 1 MeV). While the results by Hahn *et al* and Perry and Bane agree reasonably well with each other, the result by Poon found a large discrepancy of a factor $\sim$50 in the absolute cross section. Although some explanations were given for this discrepancy, it was largely left unexplained. Since this measurement was performed at an extremely low energy ($E_p < 30$ keV), it was possible that, if this discrepancy were genuine, there could be important implications. This discrepancy was one of the motivating factors for the present study of this reaction.

1.3 Goals for the Current Study of p-T Capture

Based on the previously described motivations, it was desirable to achieve the following results:

- To measure an absolute cross section at low energies, i.e. energies below E_p=100 keV. This is needed primarily to address the uncertainties in the mea-

surement by Poon [Poo91]. Since the expected cross section for this reaction is reasonably large even at low energies, gathering enough statistics should be possible. However, uncertainties about the density of tritium nuclei will complicate matters.

- Use the new measurements of the absolute cross section to obtain a new parameterized S-factor. Despite the reaction's relatively minor role in astrophysical processes, the reaction does occur. In addition, the S-factor representation has usefulness outside of astrophysics. A new parameterization should also fit with existing data taken at higher energies. Some consideration should be given as to how these previous measurements were performed. Since the beam was stopped in the target during other low energy measurements, some assumption had to be made about the form of the S-factor in order to extract the cross section. If our results invalidate these assumptions, then the cross sections that were based on those assumptions may require further analysis.

- The angular distributions in the cross section and in the analyzing power should be measured. These measurements will be needed to understand what transitions are significant. This is important because $A_y(\theta)$ is often sensitive to very small effects since it arises from interference between different transition amplitudes. The ability to produce a polarized proton beam allows measurement of the analyzing power.

- Perform a transition matrix element analysis of the data. This analysis will explicitly indicate the strength of the various transition amplitudes. Furthermore, future theoretical work will likely be compared with the results from the transition matrix element (TME) analysis.

- From the TME results, explore the possible contribution of meson exchange currents to the M1 strength. Studies of the $^{2}\mathrm{H}(\mathrm{p},\gamma)^{3}\mathrm{He}$ reaction found these effects to be significant, likewise for studies of the $^{3}\mathrm{He}(\mathrm{n},\gamma)^{4}\mathrm{He}$ reaction. Will the M1 strength obtained from the current study be consistent with the strength expected as a result of large MEC contributions?

1.4 Current Experiment

The chapters that follow will detail the various aspects of the study of the $^{3}\mathrm{H}(\mathrm{p},\gamma)^{4}\mathrm{He}$ reaction at low energies. In Chapter 2, various theoretical models and techniques being used to describe few-body nuclear physics and capture reactions are presented. In Chapter 3, a detailed description of the experimental methods and techniques are given. This includes descriptions of the facilities at TUNL, tritium targets, scattering chamber, detectors systems, and electronics. Chapter 4 explains how the raw spectra obtained from the detectors are processed to extract the observables of interest, including the angular distributions in the cross section and analyzing power, as well as the absolute cross section. This chapter also includes a new determination of the Astrophysical S-factor from these data. In Chapter 5, an explanation of the TME analysis and the results from this analysis will be presented. This chapter also includes a comparison to the results of a direct capture calculation. Also, a consistency check for the presence of MECs will be presented. A brief summary of the important points will be given in the final chapter.

Chapter 2

Theory

Theorists have made great strides in understanding few-nucleon systems in the past decade. These advances have been possible due to a combination of new methods and the rapid increase in computational power. Data from three nucleon capture reactions, such as ^{2}H(p,γ)^{3}He, compare very well with recent theories with only a few discrepancies remaining to be resolved [Wul99b]. These theoretical advances are now being extended to four-body systems. Significant progress has been made on four-body scattering reactions, and the next step will likely be low-energy capture reactions [Kie99a]. At this point in time there are no *ab initio* calculations available for the ^{3}H(p,γ)^{4}He reaction. However, since a simple direct capture (DC) model can adequately describe some aspects of the reaction, the DC model will be examined and used as a basis for a comparison with the data.

2.1 Low energy capture

Capture reactions, especially those at low energy, are generally dominated by a few fundamental effects. This has led to preferred representations that separate the interesting details of a specific reaction from generic features of capture reactions. The two most prominent effects that show up in low energy capture reactions of charged particles are the Coulomb and angular momentum barriers.

A projectile particle can be captured into a state with some relative angular momentum, l. This will result in a potential barrier whose height increases with increasing l. A low energy capture particle (both charged and uncharged) is less likely to tunnel through this barrier for cases of large relative angular momentum. Therefore, low energy capture reactions generally occur through s-wave capture (l=0), with sometimes significant admixtures of p-wave ($l = 1$) capture.

As the energy of an incoming charged particle is reduced, the Coulomb repulsion it experiences becomes more significant. The probability of tunneling through this barrier will largely determine the cross section for a capture reaction. This tunneling probability was first determined by Gamow in 1928. The probability is derived by solving the Schroedinger equation for the Coulomb potential. For low energy s-wave capture the following proportionality can be obtained,

$$P \propto \exp(-2\pi\eta) \tag{2.1}$$

where P is the probability and η is the Sommerfeld parameter [Gam28]. The Sommerfeld parameter is defined as follows,

$$\eta = \frac{Z_1 Z_2 e^2}{\hbar v} \tag{2.2}$$

where Z_1 and Z_2 are the atomic numbers of the two nuclei, e is the charge of the

electron, and v is the relative velocity. The parameter η is also frequently described as follows,

$$\eta = \frac{1}{2\pi}(31.29)Z_1 Z_2 \sqrt{\frac{\mu}{E_{cm}}} \tag{2.3}$$

where μ is the reduced mass in AMU, and E_{cm} is the center of mass energy in keV. The value 31.29 comes from evaluating the constants e and $\hbar$ in Equation 2.2.

2.1.1 S-factor

As was mentioned earlier, it is desirable to represent the cross section in terms that separate features specific to a reaction from those features exhibited in "generic" capture reactions. The standard approach used is the astrophysical S-factor, which is often referred to as simply the S-factor. It is defined as follows,

$$\sigma(E_{cm}) = \frac{S(E_{cm})e^{-2\pi\eta}}{E_{cm}} \tag{2.4}$$

where $S(E_{cm})$ is the S-factor and η is defined by either Equation 2.2 or Equation 2.3 [Rol88]. The exponential term originates from the Coulomb barrier mentioned previously (see Equation 2.1). The $1/E_{cm}$ comes from geometrical area considerations. Classically this cross section would take the form $\sigma = \pi(r_1 + r_2)^2$, where the r's are the radii of the particles involved. The quantum mechanical analog replaces the radii with the reduced de Broglie wavelength, $\lambda\!\!\!^{-}$ or $\sigma = \pi\lambda\!\!\!^{-2}$. Since $\lambda\!\!\!^{-} \propto E_{cm}^{1/2}$, $\sigma \propto E_{cm}^{-1}$.

By following this recipe, the S-factor isolates kinematic effects of the capture reaction. It is often found that in the absence of any resonance structure, the energy dependence of the S-factor can take a very simple form. A quadratic form for the

S-factor is often all that is needed to accurately describe most reactions. In many cases even a linear form is sufficient. As a result, such reactions can easily and accurately be extrapolated to extremely low energies. This is significant in astrophysically important reactions.

Reaction rates for stellar burning are determined by integrating the product of the cross section, velocity, and the Maxwell-Boltzmann distribution of the nuclei in the star (see Figure 2.1). This integral is dominantly determined by the region between a few to tens of keV, which is where the integrand peaks. This is in contrast to most experiments which are often carried out above several hundred keV due to count rate considerations. The ability to accurately extrapolate from typical lab energies to typical astrophysical energies is essential in order for stellar and big-bang nucleo-synthesis models to make accurate predictions. These extrapolations can be unrealiable if resonances are not properly accounted for.

The results from this study will frequently be presented in terms of the astrophysical S-factor. In addition, the S-factor will be used to compare the results with previous measurements and compilations.

2.2 Direct Capture Model

One of the models that has been used to describe capture reactions is the direct capture model. In this model the incident projectile makes a "one-step" (direct) transition from the initial scattering state to the final (bound) single-particle state of the residual nucleus. The scattering state is described using the "optical model". A real and an imaginary potential, described using Woods-Saxon and derivative Woods-Saxon form factors, along with a spin-orbit and a Coulomb potential are used to

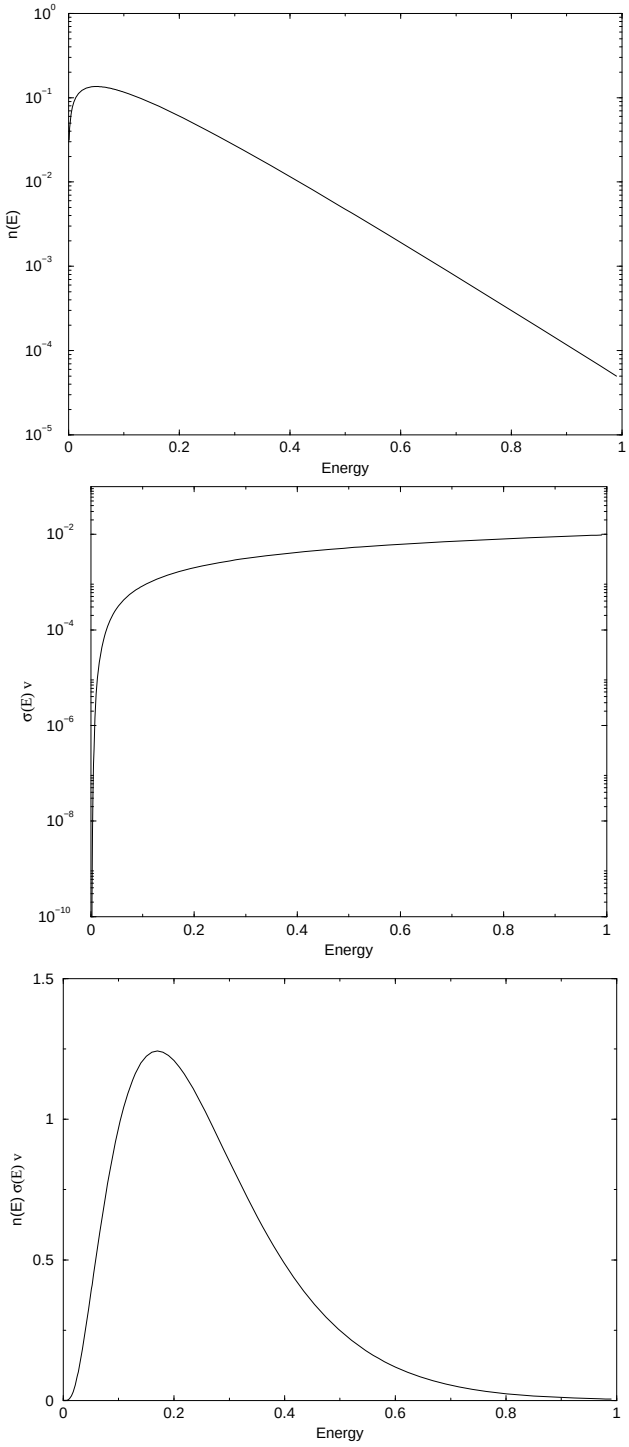

Figure 2.1: Three plots illustrating the reaction rate for in a star. The top graph is a plot of the thermal distribution for the nuclei. The middle plot is of the product of the cross section and the velocity. The bottom plot is of the product of the top two graphs. The plots do not represent a specific reaction and the units are arbitrary.

generate the incident distorted wave function. The bound state is described using a single-particle wave function obtained by adjusting the parameters of a real Woods-Saxon potential in order to reproduce the quantum numbers and binding energy of the final state. An electromagnetic operator is used to describe the interaction that converts this continuum state to the bound state, emitting a photon in the process. The "direct" nature of the reaction comes from the assumption that the interaction occurs on the same time scale as the nuclear transit time, around 10^{-22} seconds. As will eventually be seen, the direct capture model can reasonably describe certain characteristics of this reaction, such as the cross section. However, due to the absence of important processes such as meson-exchange currents, it will fail to accurately predict certain details, such as the analyzing power.

The three pieces that are needed in the direct capture model are the initial continuum state wave function, the electromagnetic operator, and the final bound state wave function. The development of these pieces will be described below and will follow the treatment given in [Laf82].

Calculations of the direct capture process employ the extreme single particle description. In this representation, the effect of the target nucleus is contained in the optical model potential. This potential describes how the target nucleus distorts the incoming plane wave of the projectile particle. The angular momentum coupling can be described as follows. In the initial state the projectile spin, $\vec{s}_p$, couples with its relative orbital angular momentum, $\vec{l}$, to form the single particle state of angular momentum, $\vec{j}$. In the final state the spin of the projectile, $\vec{s}_p$ couples with its orbital angular momentum $\vec{l}'$, to form a single particle angular momentum, $\vec{j}'$. The single particle angular momentum, $\vec{j}'$, can then couple with the target spin, $\vec{s}_t$, to form the good quantum number of the total angular momentum, J'. This is the total angular

momentum for the residual nucleus which in the present reaction is ^{4}He. This coupling scheme is often referred to as the j-j coupling scheme. Another scheme is the channel spin coupling scheme, which is used in Section 5.2.

The Hamiltonian for a direct capture reaction can be written as

$$H = H^0 + H', \tag{2.5}$$

where H' is the interaction Hamiltonian which describes the electromagnetic interaction between the projectile and the γ-ray, and H^0 is the Hamiltonian describing the kinetic energy and potential for the projectile and the free electromagnetic field. Since H^0 involves nuclear forces and H' involves electromagnetic forces, H' will be reduced by the fine structure constant, α, relative to H^0. Since, the magnitude of the interaction is much smaller than H^0 ($\alpha \sim 1/137$), perturbation theory can be used to perform the calculations. Fermi's Golden Rule, which can be derived from first order perturbation theory, states that the transition rate from an initial state, i, to a final state, f, can be described by the following relation,

$$W_{fi} = \frac{2\pi}{\hbar} |T_{fi}|^2 \rho_f, \tag{2.6}$$

where W is the transition rate, T is the transition matrix element, and ρ_f is the density of final states. The transition matrix element, T, is defined as follows,

$$T_{fi} = \langle \Psi_f | H' | \Psi_i \rangle , \tag{2.7}$$

where Ψ_i and Ψ_f are the wave functions for the initial and final state respectively. Since the differential cross section is defined as a production rate per unit incident flux, it can be stated as follows,

$$\frac{d\sigma_{if}}{d\Omega} = \frac{W_{fi}}{\Phi_i}, \tag{2.8}$$

where Φ_i is the flux of incident particles. The incident flux is simply given by the product of the particle density, n_i and the velocity, v_i, with respect to the target nuclei. Assuming an arbitrary normalization volume for ρ_f and Ψ_i, one obtains Ψ_i=v_i. By averaging over the initial spins for the projectile and target and summing over the final spin projections, $\vec{J}'$, and the circular polarization states of the photon, C, the following result is obtained for the total direct capture cross section,

$$\frac{d\sigma}{d\Omega} = \frac{2\pi}{\hbar v_i}\rho_f \frac{1}{(2s_p+1)(2s_t+1)} \sum_{m_p,m_t,m_{j'},C} \left|\langle \Psi_f | H' | \Psi_i \rangle\right|^2, \tag{2.9}$$

where m_p,m_t, and m_j are the spin projections of the projectile, target, and final spins respectively. If Equation 2.9 is integrated over Ω for an E1 transition, it simplifies to [Rol77]

$$\sigma(E1) = 0.0716\mu^{3/2}\left(\frac{Z_1}{M_1} - \frac{Z_2}{M_2}\right)^2 \frac{E_\gamma^3}{E_p^{3/2}} \frac{(2J_f+1)(2l_i+1)}{(2j_p+1)(2j_t+1)(2l_f+1)} (l_i 010|l_f 0)^2 R^2_{l_i 1 l_f}[\mu b], \tag{2.10}$$

where μ is the reduced mass, M is the atomic mass, Z is atomic charge, E_γ is the energy of the γ-ray, E_p is the projectile energy in the c.m. reference frame, l is the relative orbital angular momentum, j is the spin of the particle, J is the total angular momentum of the final state, the expression $(l_i 010|l_f 0)$ represents the Clebsch-Gordan coefficient for an E1 transition, and the R represents the reduced radial matrix element. The subscripts i, f, p, and t denote the initial, final, projectile, and target, respectively. $R_{l_i 1 l_f}$ can be determined from the following integral expression,

$$R_{l_i 1 l_f} = \int_0^\infty u_b(r) O_{E1}(r) u_c(r) r^2 dr, \tag{2.11}$$

where u_c and u_b are the continuum and bound state radial wave functions, respectively, and O_{E1} is the E1 operator. Likewise, performing the integral of Equation 2.9

over Ω for the M1 transition yields [Wel82]

$$\sigma(M1) = \frac{2\pi}{3}(2\mu - \alpha)^2 \frac{E_\gamma^3}{E_p k_p} \frac{e^2}{\hbar c} \frac{1}{(mc^2)^2} \frac{(2J_f + 1)}{(2j_t + 1)(2j + 1)} \frac{l_f(l_f + 1)}{2l_f + 1} |I(M1)|^2 \delta_{l_f l_i}, \tag{2.12}$$

where the parameters are defined as in Equation 2.10 with the exception that now μ is the magnetic moment of the nucleon in units of μ_o, j is the residual spin, α is defined as

$$\alpha = \frac{Z_t + A_t^2 Z_p}{A_t(1 + A_t)}, \tag{2.13}$$

and the radial integral $I(M1)$ is given by

$$I(M1) = \int_0^\infty u_c(r) u_b(r) dr. \tag{2.14}$$

Continuum and Bound State Wave Functions

The initial (continuum) and final (bound) states are described by wave functions. These wave functions are generated by solving the Schroedinger equation for the appropriate potentials. The initial state is a product of a nuclear wave function and a distorted plane wave. The potential for the nuclear wave function is the same as that used to describe the bound state wave function and will be discussed below. The distorted plane wave is determined by solving the Schroedinger equation for the optical potential, an empirically derived model potential. The optical model potential is defined as follows,

$$\begin{aligned} V(r) = -V_0 f(a_0, r_0, r) + i4a_d V_d \frac{d}{dr} f(a_d, r_d, r) + \\ \left(\frac{h}{m_\pi c}\right)^2 V_{so} \frac{1}{r} \frac{d}{dr} f(a_{so}, r_{so}, r) \vec{L} \cdot \vec{S} + V_c(r_c) \end{aligned} \tag{2.15}$$

where V_0 is the central potential strength, V_d is the imaginary potential strength, V_{so} is the spin-orbit potential strength, V_c is the Coulomb potential strength, the function

f is a form factor, the a_n's and r_n's are parameters for the form factor, and r_c is the Coulomb radius parameter. The form factor that is used is the Woods-Saxon form factor which is defined as follows,

$$f(a', r', r) = \frac{1}{1 + \exp\left(\frac{r - r' A^{1/3}}{a'}\right)}, \tag{2.16}$$

where A is the mass number of the target nucleus. The imaginary part of Equation 2.15 is used to account for absorptive processes in the reaction. For this experiment the only absorptive process is ^{3}H(p, γ)^{4}He, which is small compared to elastic scattering, so this term should be extremely small. Furthermore, it has been found that in low energy reactions the Coulomb potential is typically dominant. The dominance is pronounced enough that the distorted wave can be considered a "Coulomb distorted" plane wave.

The parameters for Equation 2.15 are determined from other experimental studies of the reaction. The parameter set that is used for the ^{3}H(p, γ)^{4}He reaction will be explained in Section 5.5.1.

As was stated earlier the nuclear wave function portion of the initial state and the wave function for the final state are determined from the same potential form. This potential form is a Woods-Saxon potential that includes a Coulomb potential and a spin-orbit potential. The parameters for the Coulomb potential, the spin-orbit potential, as well as the form factors for the central potential are determined from previous experiments. The central potential depth is then searched in order to match the known binding energy for the final state nucleus. In addition, the bound state wave function was constructed to have a node at the origin and infinity. A plot of the radial part of the bound state wave function for a single proton in a $1s_{\frac{1}{2}}$ state is shown in Figure 2.2.

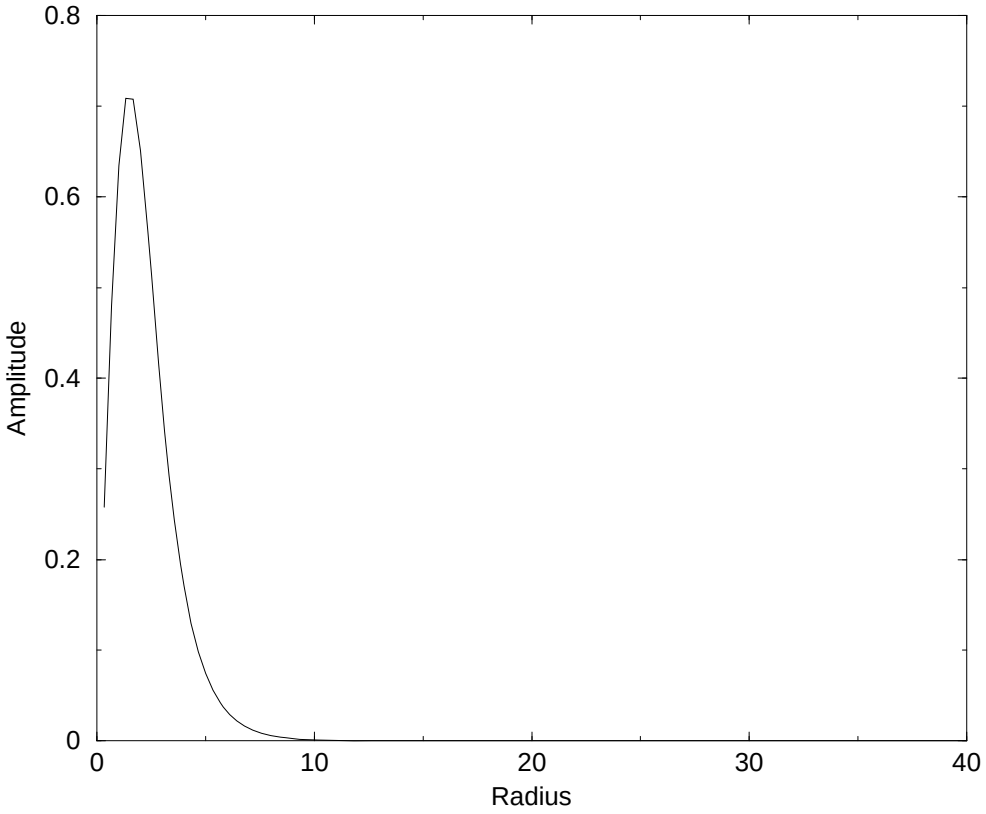

Figure 2.2: A plot of the bound state wave function of ^{4}He used in the direct capture calculations.

Electromagnetic operator

The Hamiltonian, H', used in the direct capture calculations can be stated as follows,

$$H' = -\frac{1}{c}\int \vec{J}(\vec{r}) \cdot \vec{A}(\vec{r}) d\vec{r}, \tag{2.17}$$

where $\vec{J}$ is the nuclear current density, $\vec{A}$ is the electromagnetic vector potential, and $\vec{r}$ is the relative position vector for the two particles. A multipole expansion can be performed on the Hamiltonian. After this expansion is performed it is reasonable to neglect certain terms. For example, the E1 (electric dipole) term is found to be much larger than the next order electric term, E2 (electric quadrupole). In fact, it is larger by several orders of magnitude. Higher order transitions will be even smaller. Therefore, only the E1 electric transitions will be considered. For the magnetic transitions only the dipole term (M1) will be included. By invoking Siegert's theorem the expression can be further simplified, since it allows the current density operator to be replaced with a density operator. Additionally, the long wavelength approximation can be applied, since the product of the wave number and the nuclear radius are much less that unity. Applying this approximation simplifies the radial part of the M1 operator to unity and the radial part of the E1 operator to r.

2.3 NN models and techniques

Perhaps the most intuitive picture of the nucleus and nuclear reactions can be viewed as arising from nucleon-nucleon (2-body) interactions. Various potential models describing these interactions have been proposed and each successive model has generally offered additional potential terms and additional parameters. While the

potential models often involve large sets of free parameters, for example AV18 has 40, the potentials manage to accurately match nucleon-nucleon(NN) reactions and even extend to three-body systems without major modifications to the potential or the parameters. The promise of one generic NN potential to describe a broad set of experimental data makes these models appealing. Just how well the models will extend to larger systems remains to be seen. We already know, for example, that small additions/corrections are needed in the case of three-body systems ("three-body forces"). However, initial results from studies of four-body systems suggest that no additional terms are needed beyond three-body forces [Pud97]. Experimental data from the $^3\mathrm{H}(\vec{\mathrm{p}},\gamma)^4\mathrm{He}$ reaction at low energies can help verify these results.

2.3.1 Overview of NN potentials

As experimental nuclear data have increased in accuracy and as additional observables have become available through the advent of polarized beams and targets, nucleon-nucleon (NN) potentials have become more sophisticated and complex in an attempt to match these observations. For example one of the most recent potential models, AV18, includes 18 separate terms and has 40 free parameters. These parameters are determined from data for NN scattering experiments, and manage to match the data extremely well. For example, AV18 obtains a χ^2per datum of 1.09 for 4301 data points [Wir95].

2.3.2 Three-body potentials

In the past decade with the advent of greater computational power, these NN models have been applied to three-body systems. While these models have had great

successes, discrepancies are found in some observables. The most glaring is an under-prediction of the three-body binding energy in ^{3}He and ^{3}H. In an effort to fix these anomalies various three-body forces (TBF) have been proposed.

If the presence of a third nucleon deforms the other nucleons by affecting their internal structure, then the need for TBF could arise. This is similar to the tidal deformation of the earth due to the presence of the moon (see Section 1.1.3). Since the N-N models typically absorb the internal degrees of freedom into the various potential terms, this distortion would not be accounted for in the NN potential model. One of the first attempts to resolve the discrepancies in the ^{3}He binding energy through the addition of a TBF came from Friar *et al* [Fri91]. This approach included a two pion exchange mechanism along with the AV14 NN potential, the state of the art N-N interaction at the time. While this didn't eliminate the discrepancy, it did reduce it greatly. Remaining discrepancies were attributed to sensitivities in the calculation to the short-range behavior of the TBF, which is not well known.

The next logical step in testing the new TBF was to compare the results with scattering experiments. Here the TBF was successful in describing unpolarized observables, but some disagreements were seen in polarization observables. One of the clearest disagreements has been termed the "A_y puzzle" which involves the inability of the TBF models to describe the analyzing power for polarized neutron scattering off of deuterium [Tor98](Figure 2.3).

More recently rigorous calculations have been performed for the $^1\mathrm{H}(\vec{\mathrm{d}},\gamma)^3\mathrm{He}$ reaction as well [Viv96]. While the experimental data and theoretical calculations agree reasonably well, certain discrepancies have been noted. In some observables, such as $\sigma(\theta)$and T_{20}, disagreements between theory and data are apparent [Wul99a]. Another indirect observable, the GDH sum rule integral, has indicated very strong disagree-

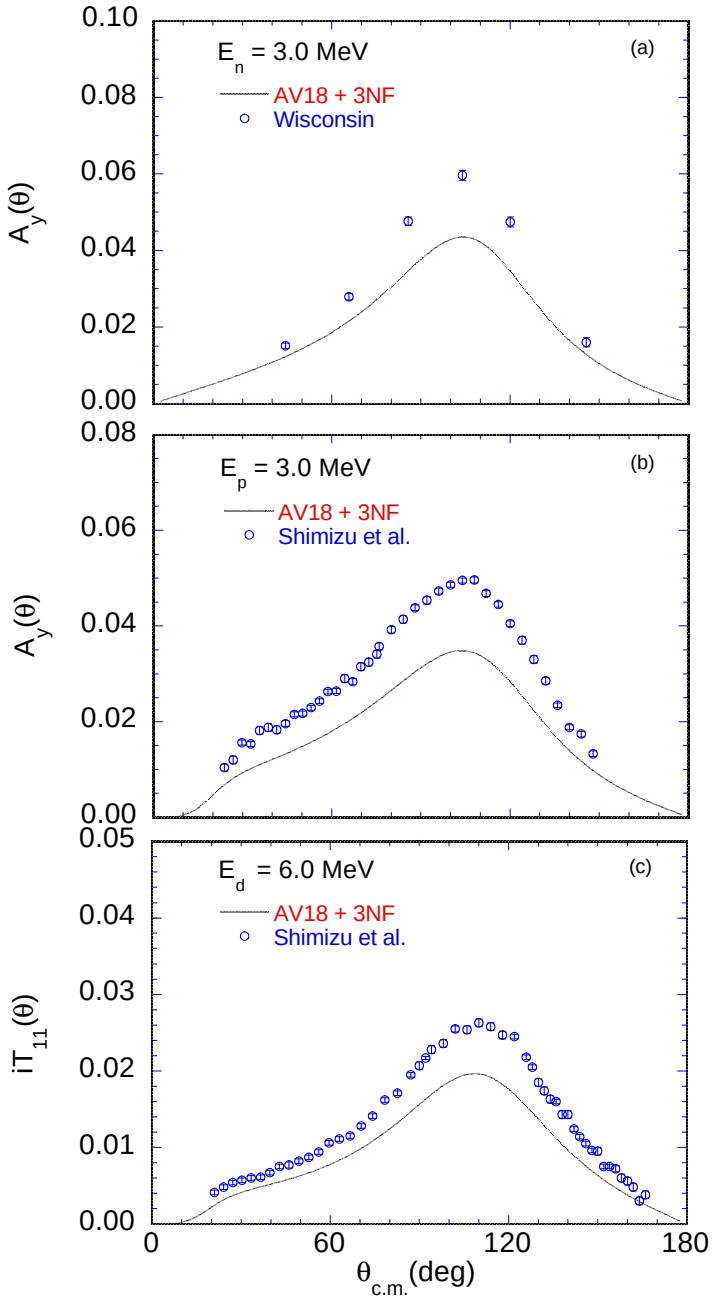

Figure 2.3: The analyzing power puzzle: (a) Comparison of rigorous three-body calculations [Kie95] and data [McA94] for the n-d analyzing power $A_y(\theta)$ at $E_n = 3$ MeV; (b) Comparison of rigorous three-body calculations [Kie95] and data [Shi95] for the p-d analyzing power $A_y(\theta)$ at $E_p = 3$ MeV; (c) Comparison of rigorous calculations [Kie96] and data [Shi95] for the deuteron vector analyzing power $iT_{11}(\theta)$. In the calculations the Argonne v_{18} (AV18) NN potential and the Urbana three-nucleon force (3NF) is used [Wir95].

ment between theory and data [Wul99b].

The issues with the current TBF models have yet to be resolved. Some speculation has been made about what additional three-body force terms may be required, but a clear consensus has yet to be reached. One solution suggested by a theorist is the addition of a three body spin-orbit term [Kie99b]. However, no justification other than empirical necessity has been given for the addition of such a term.

2.3.3 N-N Model Techniques

In addition to the abundance of potential models, there are various techniques that are used to perform the calculations. Sometimes different techniques will even employ the same models. The two major techniques used are the Faddeev and variational methods. Each of these techniques possess certain features that have made them useful in certain studies, yet cumbersome in others. These features, as they apply to low-energy capture reactions, will be discussed in the next section.

The Faddeev technique was the first successful approach at solving a three-body system using a NN model. This technique solves a three-body Schroedinger equation for a given potential. An outline of this technique can be found in [Pay86]. Since the wave functions obtained from the Faddeev technique are determined without making any approximations other than the form of the potential, this technique is considered "exact." The Faddeev approach extends the techniques used to solve the two-body Schroedinger equation by breaking the three-body equation into three coupled equations. Following the methodology of the Faddeev technique, Yakubovsky generalized Faddeev's method to N bodies [Yak67]. The equations that result from Yakubovsky's generalization are typically called the Faddeev-Yakubovsky equations.

Recently theorists have successfully employed this approach in the N=4 case for solving n-T elastic scattering. A brief description of the equations obtained for the N=4 case will be given. This will closely follow the description outlined in [Cie98].

The Faddeev-Yakubovsky (F-Y) equations provide solutions to the Schroedinger equation for N particles acting in a pairwise potential V_{ij}

$$(E - H_0)\Psi = \sum_{i<j} V_{ij}\Psi \tag{2.18}$$

In order to find a solution, the total wave function must first be split into Faddeev amplitudes Ψ_{ij} which are associated with each interacting pair,

$$\Psi = \sum_{i<j} \Psi_{ij} = \Psi_{12} + \Psi_{13} + \Psi_{14} + \Psi_{23} + \Psi_{24} + \Psi_{34}. \tag{2.19}$$

Furthermore, these amplitudes must be a solution to a system of coupled equations

$$(E - H_0)\Psi_{ij} = V_{ij} \sum_{k<l} \Psi_{kl} \tag{2.20}$$

Each of these Faddeev amplitudes must then be split into three parts, the F-Y amplitudes. These parts represent the different asymptotics of the remaining two particles,

$$\Psi_{ij} = \Psi^l_{ij,k} + \Psi^k_{ij,l} + \Psi_{ij,kl}, \quad i < j, k < l \tag{2.21}$$

and can be associated with the following set of coupled equations,

$$(E - H_0 - V_{ij})\Psi^l_{ij,k} = V_{ij}(\Psi^l_{ik,j} + \Psi^j_{ik,l} + \Psi_{ik,lj} + \Psi^l_{jk,i} + \Psi^i_{jk,l} + \Psi_{jk,il}) \tag{2.22}$$

$$(E - H_0 - V_{ij})\Psi^k_{ij,l} = V_{ij}(\Psi^k_{il,j} + \Psi^j_{il,k} + \Psi_{il,kj} + \Psi^k_{jl,i} + \Psi^i_{jl,k} + \Psi_{jl,ik}) \tag{2.23}$$

$$(E - H_0 - V_{ij})\Psi_{ij,kl} = V_{ij}(\Psi^j_{kl,i} + \Psi^i_{kl,j} + \Psi_{kl,ij}). \tag{2.24}$$

For these equations, an amplitude $\Psi^\delta_{\alpha<\beta,\gamma}$ which is not defined by Equation 2.21 is defined to be identical to $\Psi^\delta_{\beta\alpha,\gamma}$. If the appropriate permutation for the indices

are made, a set of 18 coupled equations will result. These are the F-Y equations. Solutions to these equations will also be solutions to the initial problem as given by Equation 2.18.

To solve the F-Y equations one must choose a representation such as momentum space, coordinate space or a combination of the two. If momentum space is chosen the wave functions and the potentials, V_i, must be expanded in terms of momentum "channels" [Pay86]. One consequence of this choice for charged particle capture reactions is that since the potential contains a Coulomb term, the potential will converge slowly. In practice, the groups that use the Faddeev technique have had to rely on help from calculations from the variational method to correctly calculate some reactions, such as ^{2}H(p, γ)^{3}He [Fri91].

The other prominent method is the variational method. This is the method employed by the Pisa group which has had great success in calculating many scattering and radiative capture reactions. The primary difference between the methods is in how the wave function is computed. The bound state wave function is determined using the Rayleigh-Ritz variational principle and the scattering state is determined using the Kohn variational principle.

As was mentioned earlier, theorists employing the Faddeev method encounter difficulties with slow convergence of the partial wave in the Coulomb terms. This method avoids those problems since the Coulomb operator is never expanded in terms of partial waves. In this method, only the wave functions are expanded.

The variational method works by assuming some parameterized form for the wave function, Ψ. The appropriate parameters are determined by finding a stationary point

for a function, $F[\Psi]$, with respect to all of the parameters. Stated mathematically,

$$\frac{\partial F[\Psi]}{\partial \rho_i} = 0, \tag{2.25}$$

where ρ_i are the parameters being varied.

An appropriate function, $F[\Psi]$, must be determined. One option is the Rayleigh quotient, $E[\Psi]$, which for a bound state is defined as follows,

$$F[\Psi] = E[\Psi] = \frac{\langle \Psi | H | \Psi \rangle}{\langle \Psi | \Psi \rangle}, \tag{2.26}$$

where H is the appropriate Hamiltonian for the bound state. Determining the parameters ρ_i simply requires substituting Equation 2.26 into Equation 2.25 with the correct H, and finding the solution.

The solution that is determined from the variational method is not an exact solution. Instead it is an approximation of the solution. Since one characteristic of the exact solution is that it minimizes the ground state eigenvalue, E_0 for the Hamiltonian, H, any inexact solution will meet the following inequality,

$$E[\Psi] \geq E_0. \tag{2.27}$$

This condition is often derived in standard quantum text books such as [Sha80]. The derivation starts by expanding the wave function in terms of eigenfunctions of H, ϕ_m,

$$|\Psi\rangle = \sum_m a_m |\phi_m\rangle, \tag{2.28}$$

where the eigenfunctions are defined by

$$H |\phi_m\rangle = E_m |\phi_m\rangle. \tag{2.29}$$

If Equation 2.28 is substituted into Equation 2.26, one obtains the following expression,

$$E[\Psi] = \frac{\sum_m |a_m|^2 E_m}{\sum_m |a_m|^2}. \tag{2.30}$$

Subtracting E_0 from each side yields the following,

$$E[\Psi] - E_0 = \frac{\sum_m |a_m|^2 E_m}{\sum_m |a_m|^2} - \frac{\sum_m |a_m|^2 E_0}{\sum_m |a_m|^2} = \frac{\sum_m |a_m|^2 (E_m - E_0)}{\sum_m |a_m|^2}. \quad (2.31)$$

Since the ground state, E_0, is by definition the lowest energy eigenvalue, it can be seen that the right hand side of Equation 2.31 must be greater than or equal to zero and therefore Equation 2.27 must be true.

The practical importance of Equation 2.27 comes from that fact that a determination of Ψ can be achieved by performing a random search on the parameter space ρ_i looking for a minimum in $E[\Psi]$.

The application of this method for the case of the ^{2}H(p,γ)^{3}He reaction are discussed in [Kie93, Kie94]. Calculations for the ^{3}H(p,γ)^{4}He reaction will likely employ a similar approach.

2.4 The Few-Body Problem and Capture reactions

2.4.1 Lessons from p-d

As was stated earlier, previous experimental work with the ^{2}H(p,γ)^{3}He reaction by Schmid and Wulf coupled with theoretical work by Friar *et al* and the Pisa group has greatly expanded the understanding of this reaction at low energies [Sch97, Wul99b, Fri91, Viv96]. Some of the lessons learned from these studies should extrapolate to the ^{3}H(p,γ)^{4}He reaction. One aspect is the pseudo-orthogonality between the bound and continuum state wave functions and its consequences on the importance of meson-exchange currents in the M1 strength. A second aspect is the dominance of the Coulomb phase in the determination of the phases for the transition matrix elements (TMEs).

Schiff first noticed that in thermal n-d radiative capture, the cross section was greatly reduced compared to that observed in n-p radiative capture [Sch37]. At thermal energies, neutron capture proceeds entirely via s-wave capture, which results in M1 radiation. In n-d capture the M1 strength is substantially suppressed. The explanation for this involves the M1 operator. In the impulse approximation, the dominant part of the final state of this reaction, ^{3}H in its ground state, is an eigenfunction of the one-body M1 operator. Since the initial continuum state wave function is orthogonal to the final state wave function, the contribution to the cross section from the one-body M1 operator is extremely small. As a result of this "pseudo-orthogonality" much of the strength must come from meson-exchange currents (MECs). As a result, n-d radiative capture is much weaker when compared to n-p radiative capture, where the one-body process contributes. It was later noticed that these conditions are also present in p-d radiative capture [Ver50]. In this reaction the Coulomb potential creates a significant E1 strength as well, but like the n-d system much of the M1 strength ($\sim$50%) is attributed to MECs. In looking at the ^{3}H(p,γ)^{4}He reaction, once again, the conditions are present for MECs to play a significant role in the M1 strength. In fact, it has been observed that this pseudo-orthogonality is exhibited more strongly in 4-body reactions compared to 3-body reactions [Car90, Kie99a].

The other lessons that can be gleaned from the ^{2}H(p,γ)^{3}He work was the dominance of the Coulomb phase in the transition matrix elements (TME). A more detailed explanation of the TME analysis will be given in Section 5.2. Briefly, the reaction is expanded into a set of amplitudes and phases of the TMEs. The values of these quantities can be determined by a fit to the experimental data. In the case of the TME analysis done for the ^{2}H(p,γ)^{3}He reaction by Wulf and Schmid, enough observables were measured so that an unconstrained fit could be performed. Therefore the phases

were extracted directly from the data. Another technique of determining the phases is from the corresponding scattering reaction. Both methods show that the phases are predominantly determined by the Coulomb phase. The Coulomb phase is the portion of the phase that can be attributed to the effect of the Coulomb potential on a given partial wave. The remaining portion, the nuclear phase, was typically found to be less important. Scattering data for the p-t system also show that the Coulomb phase is dominant. The usefulness of this dominance will be explained in Section 5.2.

2.4.2 p-Ts place in the scheme

While theoretical work on 4-body reactions has just recently begun, it is possible to make some prediction on the order in which the work will progress [Kie99a]. Some work has already been done by various groups studying scattering reactions. This is an obvious starting point since the scattering processes must be understood before capture reactions can be studied. The ^{3}He(n, γ)^{4}He reaction and ^{3}H(p, γ)^{4}He reaction at low energies will likely be the first capture reactions to be studied. The absence of open channels besides the reaction of interest make these appealing early testing grounds for the theoretical techniques. The ^{2}H(d, γ)^{4}He reaction will likely be the last 4-body reaction to calculated. However, it may provide the most sensitive testing ground since, like the ^{2}H(p, γ)^{3}He reaction, there is an abundance of measurable observables (e.g. tensor analyzing powers) that could be tested against theories.

Chapter 3

Instruments and Methods

Measurements of the $^3\mathrm{H}(\vec{\mathrm{p}},\gamma)^4\mathrm{He}$ reaction were performed at the Triangle Universities Nuclear Laboratory (TUNL) using the Atomic Beam Polarized Ion Source (ABPIS). This beam was directed onto a liquid nitrogen cooled, tritiated titanium target. The reaction was studied by detecting the resulting γ-rays using a combination of shielded and unshielded sodium iodide (NaI) detectors. The signals were processed by various electronics before being digitized and sent into a computer for analysis.

3.1 Polarized Beams

In early nuclear physics experiments, an understanding of nuclear structure was gained primarily by studying decay processes or by bombarding a target with a beam of charged particles. Since the beams and targets were typically unpolarized, only the total cross section or the angular distributions of the cross sections could easily be

measured. Therefore, only observables that could accurately be extracted from these measurements could be compared with theory. With the development of polarized beams and targets, additional information about a reaction could be extracted. In addition, polarized beams and targets allowed some observables to be determined to a greater precision than could be achieved with standard beams and targets. For example, analyzing powers, which can be measured with polarized beams, come about from interference between different transitions. Often a weak transition that would be difficult to extract from an angular distribution of the cross section, can be extracted from an analyzing power through its interference with a strong transition. In this experiment, a beam of polarized protons was utilized to measure the analyzing power as a function of angle for the $^3\mathrm{H}(\mathrm{p},\gamma)^4\mathrm{He}$ reaction. It will be seen that a weak transition that is almost undetectable in $\sigma(\theta)$ can be easily extracted from $\mathrm{A}_y(\theta)$.

3.1.1 Polarized Protons

For the proton there are two spin sub-states usually referred to as up and down or $m_s = +1/2$ and $m_s = -1/2$. If a collection of protons can be prepared such that there are more protons with one spin projection than another along a specific spin axis, then the collection is considered polarized. Mathematically, the polarization is defined as

$$\mathrm{p}_\zeta = \mathrm{N}_+ - \mathrm{N}_-, \tag{3.1}$$

where p_ζ is the polarization along the axis ζ and $\mathrm{N}_+$and $\mathrm{N}_-$are the fraction of protons in the $+1/2$ and $-1/2$ spin sub-states, respectively.

Figure 3.1: A cut-away view of the different parts of TUNL's ABPIS. The function of each section is explained in this section. The spin-filter polarimeter is not indicated in the diagram.

The stages are as follows: first, an atomic beam must be extracted; next, a nuclear polarization is created; thirdly, the beam is ionized; and finally, the polarization is rotated to the direction required for the experiment.

The atomic beam is created by dissociating a gas of hydrogen. Since hydrogen gas is naturally in a molecular state of H_2, it must be broken apart to create the atomic form, H. This occurs in the dissociator, where an RF discharge tube breaks the molecules apart. Once the gas is dissociated, it must be extracted from this region. Since the next stage prefers a beam of well-collimated, slow-moving particles, the extraction is performed using a copper nozzle which is cooled to roughly 30 K.

From Equation 3.1 it can be seen that to create a polarized beam one must define a spin axis and populate one spin state more than the other. The ABPIS accomplishes this through a combination of strong magnetic fields, RF transition units, and by utilizing the weak coupling between the atomic and nuclear spins.

In the polarization unit, the beam travels through two Stern-Gerlach magnets. The magnetic field produced by these magnets causes the atoms with an electronic spin projection, m_j, of $+1/2$ to be focused, while causing those with an electron spin projection of $-1/2$ to be defocused. Therefore, what remains when the beam exits this region is a beam of almost a pure electron spin of $m_j = +1/2$. The ultimate goal is to extract a beam with some chosen nuclear spin state, m_i. This is done using the adiabatic passage method[Phi87]. In this method, a hyperfine splitting of the different nuclear and electronic spin states is created. RF transition units are then used to pump certain states into the desired spin state. This creates a population inversion between certain pairs of hyperfine states and results in a beam of polarized protons (or deuterons).

To illustrate this method, the process for polarizing a proton in both spin states will be explained. To aid in this, the Breit-Rabi diagram shown in Figure 3.2 will be used. This plot shows the splitting that occurs when a magnetic field is applied to the atom. Splitting occurs in both the electronic spin, m_j, and the nuclear spin,

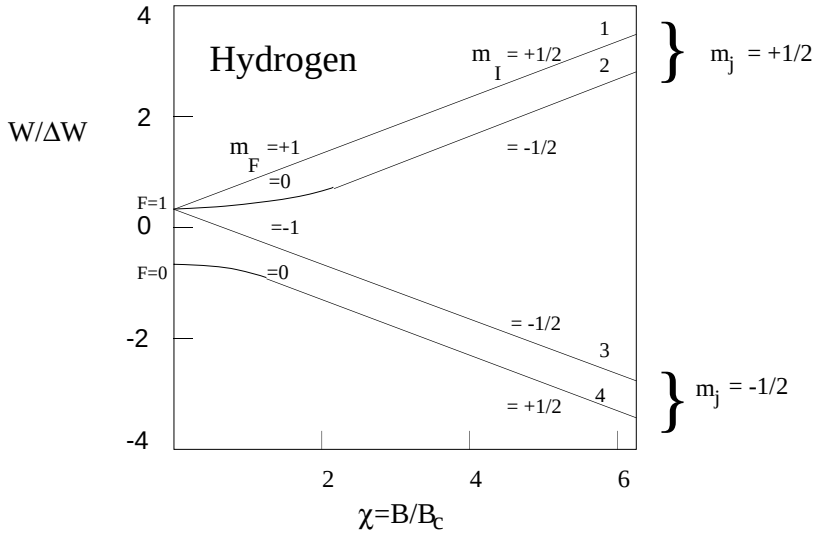

Figure 3.2: Breit-Rabi plot of hyperfine splitting. The axes and units are explained in the text.

m_i, for each m_j. The splitting in the electron spin is the Zeeman splitting and the splitting in the nuclear spins is hyperfine splitting. In the plot, the vertical axis is the energy given in units of ΔW. ΔW is the zero field splitting which is the energy difference between the triplet and singlet states in the absence of a magnetic field. The horizontal axis is the magnetic field strength, where the units are given in terms of the "critical field", B_c, which is the magnitude of the magnetic field due to the proton at the position of the electron. B_c is defined as follows,

$$B_c = \frac{\Delta W}{(g_j - g_i)\mu_b}, \tag{3.2}$$

where $g_j = -3.04 \times 10^{-3}$, $g_i = 2.002$, and μ_b is the Bohr magneton. For hydrogen, the critical field is 50.7 mT.

Following the polarization section is the ionization and charge exchange section. Here the neutrally charged atoms have their electrons stripped away or have electrons

added depending on the experiment. Negative beams are required for the tandem and mini-tandem accelerators. For the present study of the $^3H(\vec{p},\gamma)^4He$ reaction, positive beams were used since these beams are much more intense than the negatively charged beams. The stripping process works by passing the neutral beam through an Electron Cyclotron Resonance (ECR) ionizer. The ECR removes the electrons by colliding the beam with a nitrogen plasma. A series of electrostatic lenses are tuned to maximize transmission as the beam is extracted from this section. For the cases where negative beam is required, the beam passes through a cesium gas. The cesium atoms tend to easily give up electrons to protons or deuterons. Even in cases where positive beam is required, the cesium oven is used to minimize space charge effects that tend to disperse the beam. The spin filter polarimeter (SFP) is also incorporated in the ionization and charge exchange section. Its operation will be explained in Section 3.1.3.

The final stage of the ABPIS rotates the polarization axis to the direction required by the experiment and accelerates the beam to an energy as high as 80 keV. The rotation of the spin axis is performed by a Wein-filter. The Wein-filter creates a strong magnetic field and an electrostatic field that are normal to each other. The combination of the E and B fields work to select a small range of particle velocities. In addition, the magnetic field precesses the polarization axis. The polarization axis always starts out along the beam axis. Therefore, in order to rotate the axis to the desired direction, the direction of the magnetic field is rotated by mechanically rotating the electromagnetic coils. The field strength is tunable, so that the amount of precession can be adjusted. Finally, the electrostatic field must be tuned to maximize transmission.

After exiting the Wein-filter, the beam passes through an accelerator tube, which

accelerates the beam up to 80 keV. During this experiment beam energies between 40 keV and 80 keV were used.

3.1.3 Spin Filter Polarimeter

In order to determine an analyzing power for a reaction using polarized beams the beam polarization (see Equation 3.1) must be known. At TUNL, the beam polarization is determined either with a polarimeter placed along the beam line or using the spin filter polarimeter (SFP) in the ABPIS. For $^3\mathrm{H}(\vec{\mathrm{p}},\gamma)^4\mathrm{He}$, the SFP was relied on to determine the polarization, since the SFP has been carefully calibrated in the past [Men96]. In addition to providing a measure of the polarization, the SFP also allows the polarization to be tuned for maximum polarization.

The SFP uses an RF cavity and a variable magnetic field to filter out the different nuclear spin states, m_i. This is done by first tuning and setting the RF electric field to excite a resonance in the atom. Since the magnetic field strength determines which value of m_i is able to pass through the cavity, the axial magnetic field is used to select a particular value of m_i. Those that pass through are then allowed to decay back to their ground state by removing the electric field. The resulting photons are detected in a photomultiplier tube. The current out of the photomultiplier tube is plotted versus the magnetic field strength. The nuclear spin states show up as separate peaks (Figure 3.3). The asymmetry in these peaks after background subtraction is equivalent to the beam polarization. The SFP has been found to be accurate to 5% in previous calibration tests [Men96]

Since the SFP uses atomic effects to measure the polarization, a neutral beam is required. In this experiment positive beam was used, so the amount of Cs vapor

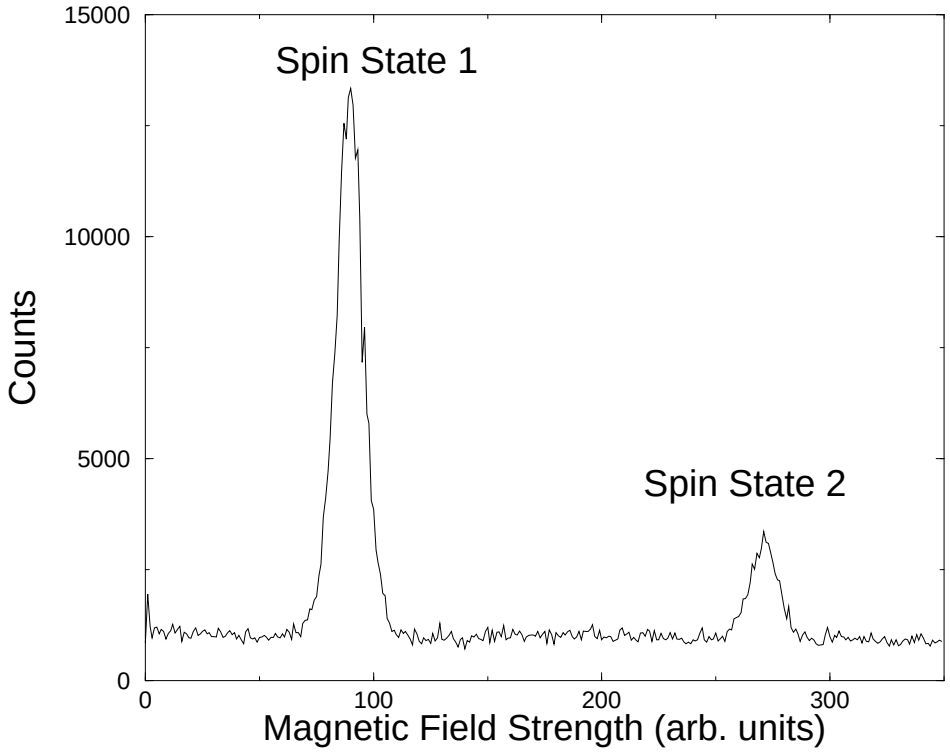

Figure 3.3: A plot of the output from the spin filter polarimeter. The two peaks correspond to the two nuclear spin states. In this case, spin state 1 is being selected by the ABPIS.

must be increased so that a reasonable amount of neutral atoms can enter the SFP unit. For negative beams the opposite is true, and the amount of Cs vapor must be decreased.

In order to carry out a polarization measurement, the following steps had to be performed. First the cesium vapor was increased. Next, the RF units, photomultiplier tubes, and magnetic field units were enabled. Finally, the measurement could be performed. This took about fifteen to thirty minutes, mostly due to the time needed to increase and decrease the amount of cesium vapor. Since the SFP does not require any changes in the final destination of the beam, it was far more convenient than using a beam line polarimeter.

3.2 Beam Transport

Once the beam has been created by the ABPIS, it is necessary to transport the beam to the target. This is accomplished through a combination of electrostatic fields and magnetic fields.

The experiment was performed on the low-energy capture (LECAP) line. This line is 60° off the axis defined by the ABPIS and approximately 30 feet long. A dipole magnet is used to deflect the beam down the LECAP line. For this measurement the polarization axis set by the Wein-filter was always oriented parallel to the magnetic field of the deflection magnet. Therefore, the inflection magnet did not precess the beam's spin axis. In order to maximize transmission through the deflection magnet, an electrostatic quadrupole placed directly before the deflection magnet is used to tightly focus the beam. After the deflection magnet, two more electrostatic quadrupoles are used to adjust the focus of the beam. Steering magnets are used to

make small adjustments in the direction of the beam. These steering units are used to position the beam along the center line of the final electrostatic quadrupole, so that it is only responsible for focusing the beam. Also, a set of adjustable slits are positioned between the last two quadrupoles to help define the beam spot. These slits were usually opened up to approximately a 1" square opening. However, in some cases the slits were closed more tightly to reduce the amount of beam without adversely affecting the focusing of the beam.

The beam was kept broadly focused across the target to minimize hot spots which might degrade the target. A beam scanner was positioned after the last set of focusing elements. This was used to monitor the beam profile. Before inserting the actual tritium target, a quartz crystal was placed in the chamber at the location of the target. Since the beam scintillates in the quartz, it was used verify that the beam was broadly focused and that no hot spots were present. Once verified, the crystal would be removed and the actual target would be inserted.

In order to maximize beam transmission as well as to reduce build up of contaminant particles on the target, it was important to have a reasonably good vacuum in the beam line. For this experiment the LECAP line was outfitted with two turbo-molecular pumps, as well as a small turbo-molecular pump placed close to the chamber. Vacuums from 10^{-6} torr to 10^{-7} torr were achieved. Also, cold traps were placed after the deflection magnet at the midpoint of the beam line along with a trap that surrounded the target (see Section 3.3). These cold traps served to further improve the vacuum and remove contaminants from the beam.

3.3 Tritiated Titanium Target and Chamber

The target used for the measurements was a tritiated titanium disk. This target is produced by first evaporating a thin layer of titanium on to a 3/4" diameter copper disk. The disk is then slightly heated in the presence of a tritium vapor. The hot titanium absorbs the tritium through a process identical to hydration. Theoretically, this would allow two tritium atoms to be absorbed by each titanium atom. However, the typical ratio is approximately 1.8 tritium atoms per titanium atom. This translates into a number density of approximately 1×10^{23}nuclei/cm^3. Most of the targets that were used had been acquired from Safety Light Corporation, and were intended to be used to create neutron beams through the ^{3}H(d, n)^{4}He reaction. Since the targets were several years old, as much as 30% of the tritium had been lost to the 12.5 year half-life β-decay process. Therefore, the expected number density was approximately 7.3×10^{22}nuclei/cm^3 for the targets. Since, in this case, the measurements were performed at beam energies of 80 keV or lower, the beam is stopped within the target. The implications of this for the determination of the cross section will be discussed in Section 4.5.1. Stopping the beam in the target can also generate a significant amount of heat in the target depending on the intensity of the beam which was typically around 15 μA. Dealing with this heat was a critical factor in the chamber design.

Minimizing contamination of beam line components and containing any tritium in the chamber system represented one of the more challenging aspects of the experiment. The radiation officers both for TUNL and for Duke University were involved in reviewing the final design of the chamber. Besides affecting the chamber design, other modifications and procedures were instituted to address these concerns. The exit ports on all of the mechanical backing pumps and roughing pumps were tied

to an exhaust system. This system included two tritium monitoring stations. One station was already in place to monitor tritium from neutron production lines which used the $^{3}\mathrm{H}(\mathrm{d},\mathrm{n})^{4}\mathrm{He}$ reaction. This monitor was situated near the end of the exhaust line before an exhaust stack. If the measured level reached a certain threshold, this monitor would engage a high volume exhaust fan to reduce the concentration of any tritium that was exhausted. The other station was installed specifically for this experiment and was located several feet downstream of the backing pumps for the turbo pumps. Its purpose was to quickly generate an alarm in the event that the tritium concentration exceeded a threshold. The threshold was set to a fairly low value (10 $\mu\mathrm{C/m}^3$), so that any problems could be quickly handled.

During the first run with the tritium targets, a liquid nitrogen reservoir was used to cool a paddle that held the target. Although some decrease in the yield was observed, the target appeared to perform well. However, in a subsequent run, a water cooled system was used. Yields quickly dropped and it was determined that water cooling was insufficient. There was also a concern that contaminants were building up on the target. Both of these issues were addressed in the final design for the chamber.

The final chamber consisted of three isolated sections (see Figure 3.4). The target was attached to a copper paddle that was in direct thermal contact with a liquid nitrogen reservoir. Since the bar which connected the paddle to the bath was short and thick, there was very little temperature drop from the bath to the paddle. The liquid nitrogen reservoir consisted of an inner can, surrounded by an evacuated region that was enclosed by a thin-walled stainless steel cylinder. The low thermal conductivity of the stainless steel kept the o-ring seals from getting too cold, which could potentially affect the vacuum.

An aluminum can surrounded the target. In addition, a copper tube extended

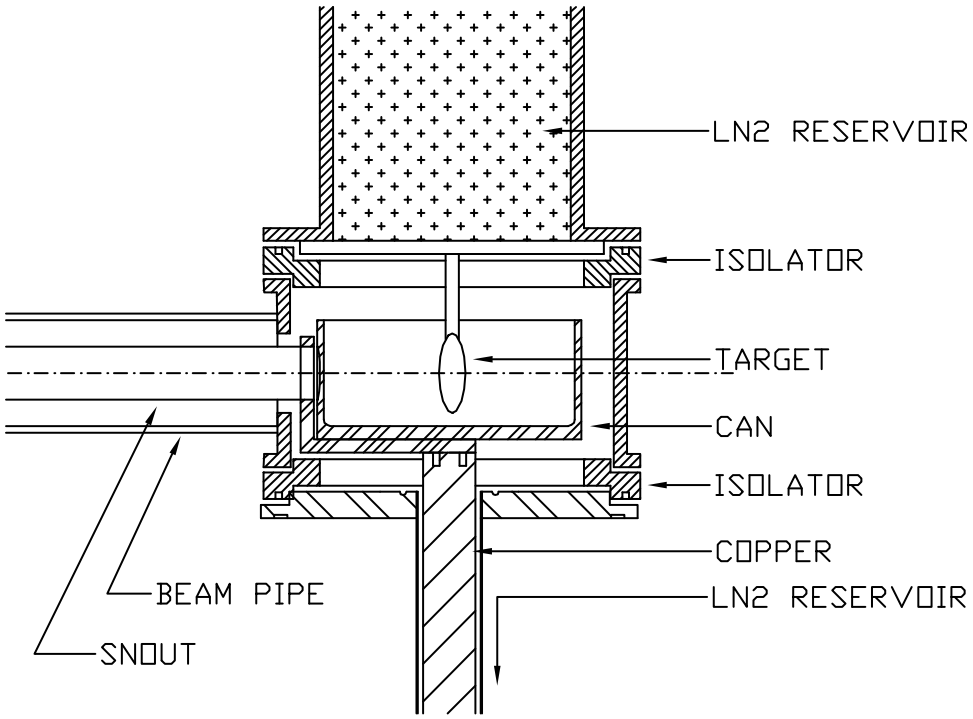

Figure 3.4: A cut-away view of the target chamber used in the experiment. The construction is explained in the text.

upstream of the target into the beam line. These two pieces were cooled by a liquid nitrogen reservoir that was separate from the reservoir that cooled the target. This assembly served two purposes. First, any tritium that escaped from the target would tend to be trapped by the cooled surfaces. Since the combination of the can and the copper tube covered most of the 4π solid angle surrounding the target, only a small amount of released tritium (less than 0.1% based on the geometry) could drift back up into the beam line. Secondly, the can and tube tended to function as an additional cold trap, absorbing water vapor and other contaminants and thereby improving the vacuum in the vicinity of the target.

A collimator was located roughly 1" in front of the target. This collimator was a thin piece of tantalum with a 5/8" diameter hole. The collimator was mounted inside the aluminum can and could be rotated so that it was parallel with the target. By keeping the collimator and target parallel, the collimator would block any beam which would hit the copper paddle. Since the collimator, snout, and can were in electrical contact with each other, the amount of beam hitting the assembly was determined by measuring the current on a wire connected to the assembly.

Once the final design was installed and the monitoring system was in place, it was found that the system performed very well. A drop in count rate of roughly 10% when a target was used after a long storage period was typically observed. This was attributed to a migration of tritium towards the surface of the target during the storage period which is then quickly sputtered out of the target. This initial drop would occur over a period of about an hour. However, after this initial drop, yields remained relatively steady with drops of only a few percent being observed over extended periods. During a run, the tritium monitors, beam current, beam profile, and γ-ray yields (see Figure 3.5) were closely monitored for any sudden changes. The

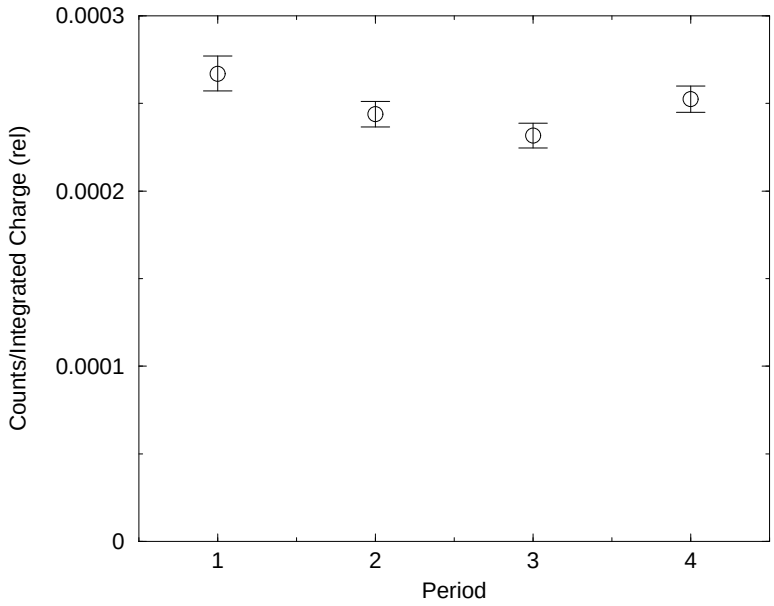

Figure 3.5: A plot illustrating the target stability. The plot spans four days and each point represents the true counts divided by the integrated charge for approximately a single day. The error bars represent the statistical uncertainty.

system functioned safely during all of the runs. The runs typically lasted 7 days and, for the productions runs, totaled 21 days.

In addition to the monitoring done during the run, wipe tests were performed on the chamber and beam-line at certain times. Wipes done on surfaces in close proximity to the target typically measured several tens of μCs/in^2. Upstream points measured at levels of tens of nC/in^2. For equipment to be handled without any special precautions it must measure below approximately 6 nC/in^2. Items that exceed this level must be properly tagged and stored or de-contaminated by a cleaning process.

3.4 Beam Integration

In order to make a determination of the cross section as well as to accurately relate data from different run conditions, the total number of projectile particles impinging on the target must be determined. Since the projectile particles are charged, integrating the charge during the duration of a run is an extremely accurate way to determine this. This is achieved by first connecting a wire to the target rod. This wire runs in series with a high voltage battery to suppress secondary electrons from easily leaving the target which would cause the measured charge to be incorrect. This line is then fed into a model 1000 Brookhaven Beam Charge Integrator. This unit samples the charge and produces a series of logic pulses whose number is proportional to the amount of charge. These pulses are then counted by both scalar units as well as count down units in the data acquisition system.

3.5 Sodium Iodide Detectors

As the projectile protons impinge on the tritium nuclei in the target, some of the protons will undergo the reaction of interest, $^3\mathrm{H}(\vec{\mathrm{p}},\gamma)^4\mathrm{He}$. By measuring the resultant γ-ray the reaction can be detected and studied. Since the energy of this γ-ray is 19.86 MeV, a sodium iodide (NaI) detector is the most practical choice, because a NaI detector has both a reasonable efficiency and resolution in this energy range. A large NaI detector typically consists of a NaI crystal that is optically connected to several photomultiplier tubes. The photomultiplier tubes are then electrically connected to bases that supply the power and collect the charge from the tube.

The resolution of a detector is measure of how closely the measured spectrum

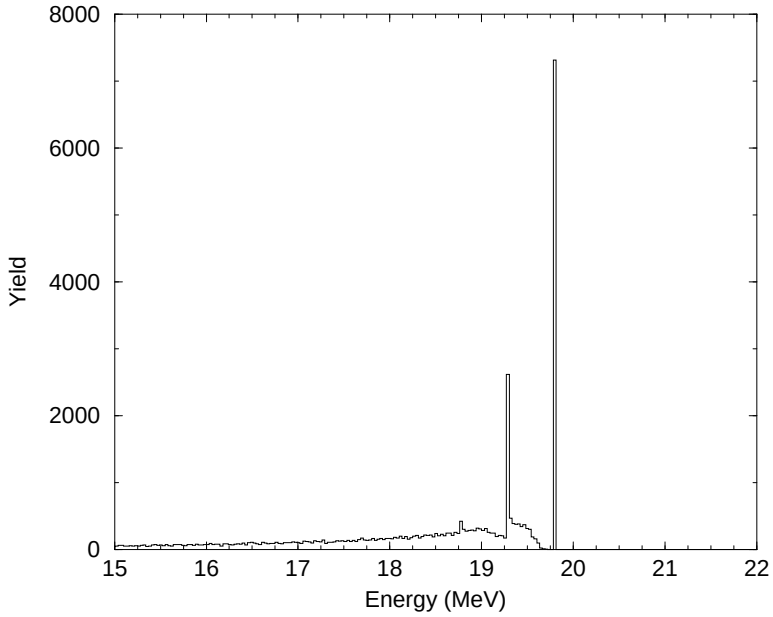

Figure 3.6: Monte-Carlo generated spectra which only includes geometrical effects for a 10"x10" NaI detector placed in front of a pencil beam source of 19.8 MeV γ-rays.

from detector corresponds to the actual spectrum. Material properties, light collection efficiency, as well as effects due to geometry determine a detectors resolution. A γ-ray spectrum has characteristic shape. There is typically a full energy peak, a series of escape peaks, and a Compton peak (see Figure 3.6). These attributes can be understood by examining how γ-rays interact with the detector material.

A γ-ray can undergo three basic processes when it interacts with matter: Compton scattering, pair production, and the photo-electric effect. Since these processes are well understood, there effect on the response function for a γ-ray detector is also well understood. In a NaI detector, γ-rays will interact with the detector material and deposit energy into the detector. During this process most or all of the γ-ray's energy is absorbed by the detector. Cases where the γ-ray deposits all of its energy in the detector will fall in the "full energy peak." γ-rays which undergo Compton

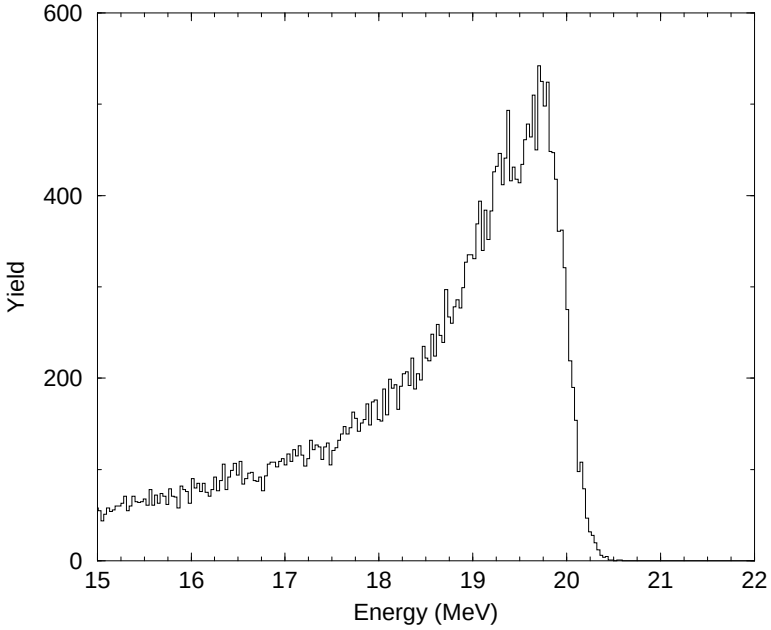

Figure 3.7: Monte-Carlo generated spectra which includes geometrical and smearing effects for a 10"x10" NaI detector placed in front of a pencil beam source of 19.8 MeV γ-rays.

scattering and subsequently escape the detector will leave a broad peak on the low energy of the full energy peak. This peak extends from zero energy up to the Compton edge. Additional peaks come from positrons, created from pair production, thermalizing and creating two 511 keV γ-rays. If one of these γ-rays escapes the detector, it will deposit exactly the full energy minus 511 keV. This peak is the first escape peak. When both 511 keV γ-rays escape the second escape peak is created. Each of these cases get folded together to create the response function of the detector. Since the three processes have a strong energy dependence, the ratios and sizes of these features strongly depend on the energy of the γ-ray being detected as well as the size of the detector and the collimation arrangement. For example, a small detector will experience more escapes of 511 keV γ-rays and therefore exhibit a larger escape peak when compared to a larger detector. The Compton peak behaves in a similar manner. A collimator can be used to block γ-rays which would pass through the edges of a detector. This results in less pair-production and Compton scattering events near the edges of the detector where they can easily escape and, hence, results in smaller escape peaks and Compton peaks.

Ultimately photo-ionization occurs and the resulting light is collected. This is the slowest process and strongly determines the duration of the resulting signal. This process also strongly determines the energy resolution of the detector, since the resolution for this type of detector is essentially determined from the statistical nature of the light collection. The resolution comes from the variation in the number of photons created from a specific γ-rayenergy and, therefore, proportional to the $\sqrt{n}$, where n is the number of photons collected. The average number of photons created for a specific energy γ-ray is determined from the detector material.

Figure 3.6 and Figure 3.7 illustrate the effects of geometry and resolution on the

response function. Figure 3.6 shows a simulated spectrum generated using the EGS4 code [Nel85]. This spectrum represents the energy deposited by a pencil beam of 19.8 MeV γ-ray in a 10"x10" cylindrical NaI detector with perfect resolution. After accounting for this uncertainty in the detector, the response function for the same case results in the spectra plotted in Figure 3.7.

Besides energy resolution, the other important attribute of a detector is its efficiency. For NaI detectors this is usually defined as the percentage of total γ-rays crossing the front face of the detector that are detected and fall inside some range around the peak. One convention for defining this range is the "one width up, two widths down" convention, where the width is the full width at half max of the peak and the range runs from two widths below the centroid of the peak up to one width above the centroid (see Figure 3.8). For a 10"x10" NaI detector this number is roughly 60% for a 20 MeV γ-ray(see Section 4.2), which is quite good. For comparison, a fairly large 4"x5" high purity germanium detector might have an efficiency of less than 0.1%. Other detectors, such as lead glass, might offer slightly better efficiency, but at the expense of having a worse energy resolution. Therefore, the NaI detector is often the preferred choice for detecting γ-rays in the energy range above 10 MeV.

For a NaI detector, atomic ionization and bremsstrahlung create photons which propagate through the crystal and can be detected by a photomultiplier-tube. The photomultiplier-tube consists of a cathode, an electron multiplier section, and an anode. The cathode is made of a photosensitive material which will emit an electron when a photon hits it. The multiplier section consists of a series of charged plates which takes the electrons from the cathode and creates a shower of electrons that are collected at the anode. The collected charge generates an electronic pulse which can

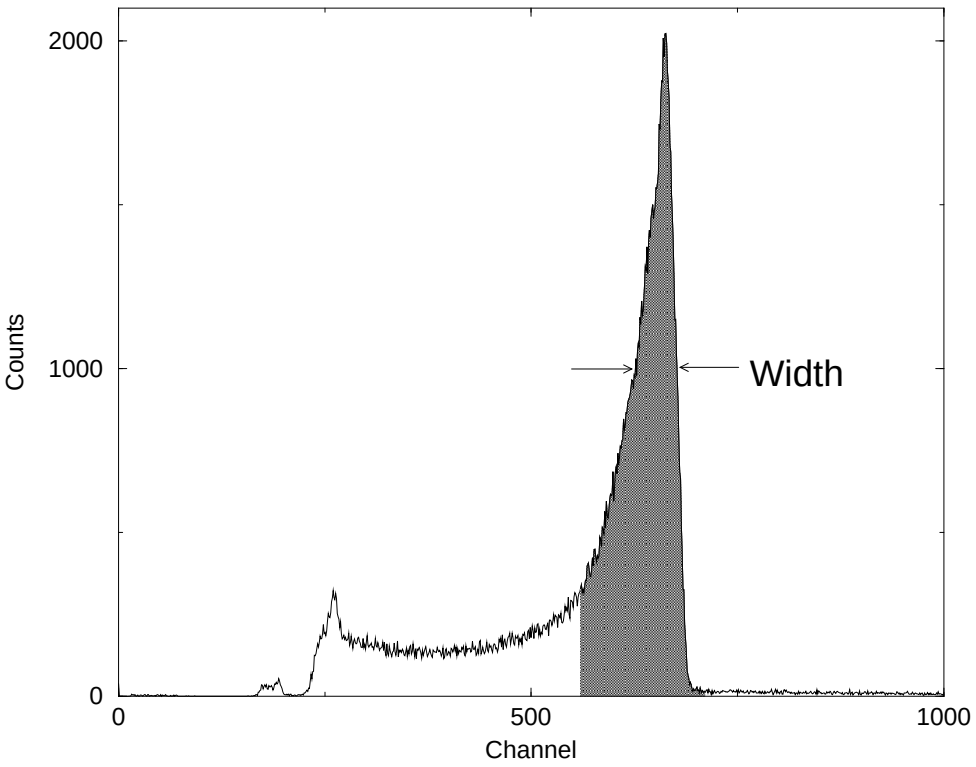

Figure 3.8: Plot illustrating the "one width up, two widths down" convention for NaI detector spectra. The shaded area indicates the "one-width up, two-widths down" region which was summed to obtain the yields. The low energy cutoff is the result of a discriminator which was set to this level in order to reduce pile-up in the region of the peak.

be discriminated and amplified using standard nuclear-physics electronics. A base unit connected to the tube provides the high voltage power that biases the plates in the photomultiplier-tube, as well as collecting the charge that is created by an event. The outputs from the bases are summed together and fed into the electronics that are responsible for converting the signal into a digital measurement of the total energy deposited into the crystal.

3.6 Other Detectors

The $^{3}\mathrm{H}(\mathrm{d},\mathrm{n})^{4}\mathrm{He}$ reaction was also measured during this experiment in order to determine the tritium density in the target (see Section 4.5.2). This measurement was performed at a deuteron lab energy of 80 keV. This results in roughly a 14 MeV neutron and a 3.5 MeV α-particle (^{4}He). Both of the residual particles were detected. Since the detectors used to study this reaction are secondary in nature to the primary experiment, they will not be explained to the extent of the NaI detectors.

The α-particles were detected using a gold plated silicon-surface barrier detector. A reverse bias is created in the material by applying a voltage to the solid-state diode. When an α-particle interacts with the material it creates an electron hole-pair. This reverse bias also establishes the sensitivity depth (depletion layer) of the detector. The potential created by the bias accelerates the electron which creates a small current– thus generating a signal. This signal is subsequently amplified in a manner similar to that of the NaI signals which is detailed in Section 3.7. A plot of the spectra from this detector setup is shown in Figure 3.9.

The neutrons were detected using a detector filled with Bicron 501A liquid scintillator. The properties for this detector have been carefully measured and calibrated

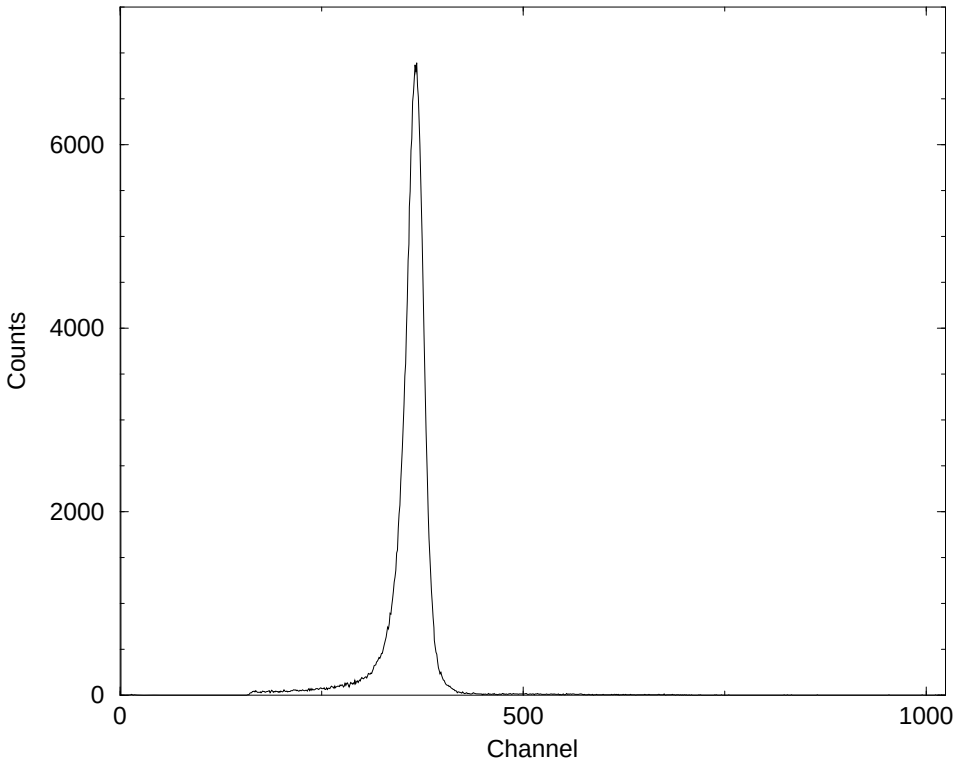

Figure 3.9: A plot of the spectra from the charged particle detector for the $^{3}\mathrm{H}(\mathrm{d},\mathrm{n})^{4}\mathrm{He}$ reaction.

by other TUNL researchers. Typically, the neutrons will interact with the protons in the scintillator. The probability for this type of reaction is small, so neutron detectors typically have efficiencies between 5% to 30% depending on the energy of the neutron and the threshold. The threshold is usually calibrated against the 662 keV γ-ray emitted from ^{137}Cs which is equivalent to a 341 MeV neutron. Therefore the threshold is normally specified in terms of a fraction of this energy (i.e. 1/2 Cs). The $^{3}\mathrm{H(d,n)}^{4}\mathrm{He}$ reaction was measured with various thresholds, however, since the energy of the neutron is relatively high, changing the threshold only had a small effect on the efficiency in this case. For the highest threshold setting of 1 Cs, an efficiency of roughly 7% was used, while at the lowest threshold setting of $\frac{1}{4}$Cs, an efficiency of roughly 6% was used. A plot of the spectra from the neutron detector for this setup is shown in Figure 3.10.

After analyzing the results from the two detectors, the $\alpha - particle$ detector results were deemed more reliable and were therefore given primary attention. Since the efficiency of the charged particle detector is essentially 100% and it is not necessary to make corrections for such things as attenuation and multiple scattering, extracted yields were more reliable than those from the neutron detector. However, the results from the two detectors were checked against each other and were found to be consistent within an accuracy of 10%.

3.7 Electronics

Before the data acquisition system can convert the analog signals from the detectors to digital values that can be analyzed, the signals must be processed by an electronics setup that is specifically tuned for the experiment. The electronics amplify,

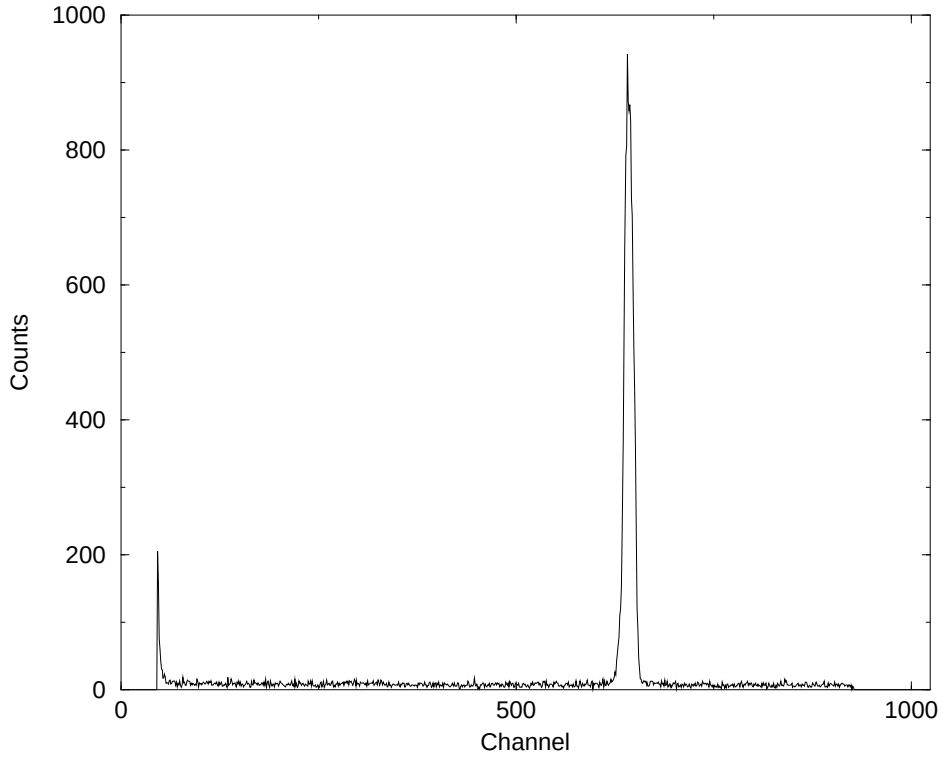

Figure 3.10: A plot of the spectra from the neutron detector for the $^{3}\mathrm{H}(\mathrm{d},\mathrm{n})^{4}\mathrm{He}$ reaction.

shape, and discriminate the signal before sending it to the data acquisition system.

The signals coming from the NaI detectors were typically a few 100 mV in size and several μs in length. Often, each signal was fed down a long terminated line to generate a delayed reflection that was joined with the original signal. This clipping technique reduces the signal length to the round-trip transit time of the reflection cable, which is usually about 100 ft long or approximately 200 ns. A resistor at the end of the cable is used to adjust the size of the reflected-inverted pulse so that is has the correct size to cancel the tail of the original pulse when the two are added together.

The signal, whether it was clipped or not, was then fanned out. One copy went to an amplifier circuit, that shapes and amplifies the signal so that it is more suitable for the analog-to-digital converter ADCs (see Section 3.8). The amplification is accomplished using a spectroscopy amplifier. These amplifiers are designed to linearly amplify the signal and not adversely affect the resolution of the pulse-height of the signals. The amplified signal is typically a few volts in size and around 1 μs in length. The other copy was discriminated and used to generate scalar signals, as well as a gate for the ADC. This signal is first sent through a timing filter amplifier (TFA). This amplifier is designed to amplify the signal and to generate an output pulse with short rise and decay times. The output from the TFA is sent to a constant fraction discriminator (CFD). A discriminator creates a logic signal whose output depends on whether or not the input signal is above a set threshold. A CFD can do this without introducing excessive "walk". Walk occurs when energy dependent time shifts are introduced in the output signal. The logic signal from the discriminator is sent to a gate and delay generator. The length and delay of the gate is adjusted to window the energy signal coming out of the spectroscopy amplifier. This gate is used to trigger

the ADC.

In cases where the count rate was low, a circuit was included to reduce pile-up. Pile-up occurs when two separate events occur within the timing resolution of the detector or the electronics. In this case, the goal was to keep two separate events from being digitized by the ADC. To accomplish this, a short gate ($\sim$400ms) is created which just encompasses the initial signal. The gate is triggered by the output of the discriminator, whose input came from the TFA. Since the TFA pulse lasts only 10-15 ns, pulses below the discriminator level which are greater than 10-15 ns apart, cannot "pile-up" since the gate will not open for them. Subsequently, a long gate is created to "hold-off" events above the discriminator level from adding together and getting digitized.

In certain cases, the count rate was so low that an active shield was required in order to reduce or eliminate the cosmic-ray background. In these cases, a logic signal was created from the shield signal in a manner similar to what was used for the NaI detector. The output from the phototubes were joined together and sent to a TFA. The output from the TFA was then sent to a CFD. This logic signal was used in conjunction with the signal from the NaI detector to form a logic circuit. When a coincidence was observed between the two signals, it was assumed that the event represented a cosmic-ray event and should therefore be vetoed. The CFD level for the shield had to be adjusted so that good events that deposited energy in the shield due to pair production or Compton scattering would not also get rejected. However, some good events will still be rejected. This must be accounted for in any cross section measurement.

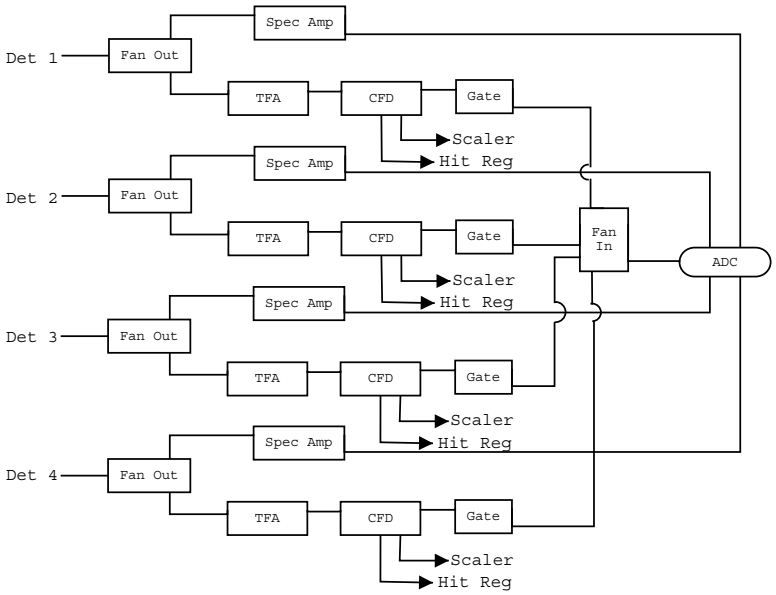

Figure 3.11: Schematic diagram of electronics for unshielded NaI detector set-up.

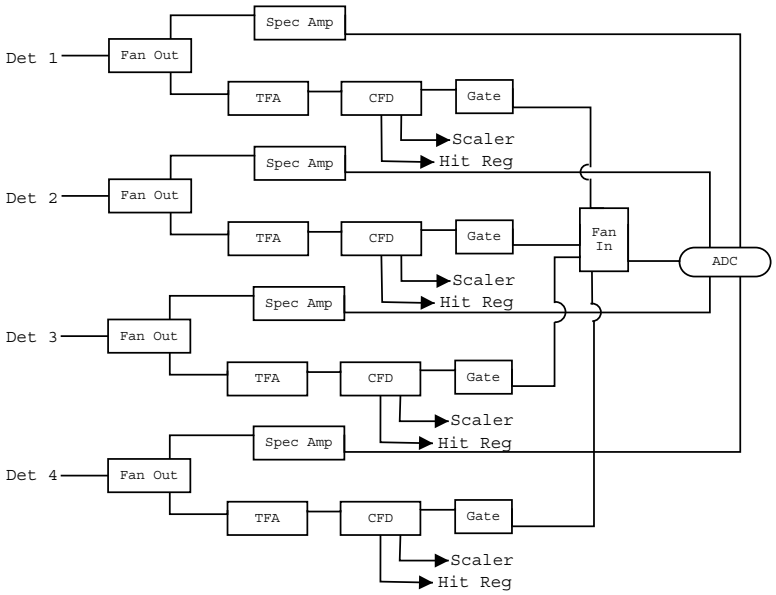

Figure 3.12: Schematic diagram of the electronics for the spin-state and BCI related circuitry.

3.8 Computer Interface

The next step in the process is to take the amplified and shaped pulse and digitize it into a form that can be understood by the computer. This was done using an Ortec 413a analog-to-digital converter (ADC) module that resides in a CAMAC crate that is part of the data acquisition (DAQ) system. The Ortec 413a is a peak-sensing ADC, meaning that it will attempt to determine the peak of a signal and then convert that height into a digital number. A gate generated from the logic portion of the electronic circuit helps the ADC to determine when to analyze the signal and look for a peak to digitize. Once the signal has been digitized, the ADC module generates a "look-at-me" (LAM) signal to notify the system that it has an event. A multi-branch driver (MBD) unit that is connected to a Micro-VAX 3200 is responsible for answering these requests, as well as sending the data that is acquired to the VAX. The LAM triggers a string of commands stored in the MDB to be sent to different CAMAC modules. These commands include reading out the ADC, the input register, and clearing and reseting the modules so that they are ready for the next event.

The MDB stores the data it has received from the CAMAC modules and transmits it to the VAX computer. A process running on the VAX takes the data and sorts it based on an evaluation (EVAL) procedure. The EVAL process can do such things as check that values are within certain ranges, look at certain flags, and then increment spectra based on these inputs. These spectra can then be viewed during the experiment to make sure everything is functioning correctly and that the experiment is proceeding as expected. Ultimately, these spectra are saved for analysis after the experiment. It is also possible to store the raw event data to a magnetic tape or hard drive. However this was not necessary for the measurement of the

$^3\mathrm{H}(\vec{\mathrm{p}},\gamma)^4\mathrm{He}$ reaction, since all of the required information could be extracted from the spectra generated during the run.

Chapter 4

Analysis of Observables

Several corrections had to be made to the raw data. These corrections included energy averaging effects arising from the fact that the beam stopped in the target; γ-ray attenuation effects from the chamber and other components, finite geometry effects, and detector efficiencies.

The angular distributions of the cross-section, $\sigma(\theta)$, and analyzing power, $A_y(\theta)$, have been extracted from measurements made at proton energies of 40 keV and 80 keV. The coefficients of a fit in terms of Legendre polynomials have been determined from these data. A transition matrix element analysis was also performed on the data. In addition, the absolute cross section was determined.

4.1 Background Subtraction

In a low count rate experiment where γ-rays are being detected, background is almost always present. For energies above several MeV, the largest source of back-

ground is from cosmic rays interacting in the detector (see Figure 4.1). Since these cosmic rays usually enter the detector in a mostly vertical manner, detecting signals in coincidence with a detector around the primary detector can eliminate many counts. Plastic scintillator is a cheap detector material that offers good timing but relatively poor energy resolution. However, since a precise measure of the energy is not needed for the anti-coincidence shield, plastic is an obvious choice. For a reasonably tuned electronics set-up that uses a 10 cm thick annular anti-coincidence shield, 95% cosmic ray rejection can easily be obtained.

In the ^{3}H($\vec{p},\gamma$)^{4}He reaction the yield is sufficient that in certain cases unshielded NaI detectors could be employed. For example at E_p=80 keV the count rate for true events was around 0.5 Hz which is about twice the cosmic ray event rate in the same energy range. However, during attempts to run without active shields at E_p=40 keV it was found that the background was too large (nearly an order of magnitude larger than true events), thus leading to large errors in the extracted values. Therefore, a subsequent run at 40 keV employed the shielded setup.

Once the background has been reduced as much as possible with instrumental techniques, including both active and passive shielding, a fit can be made to the shape of the background and this fit can be subtracted from the peak of interest. A true cosmic ray spectrum is relatively flat in the energy region of interest. However, pile up effects, where two different events in the detector get added together, distort the shape and create an exponential form. Therefore, a second order exponential form, as follows, is used.

$$Y(E) = A\exp(-(a + bE + cE^2)), \tag{4.1}$$

where A, a, b, and c are parameters that must be determined from the background. In some cases the fit can be performed on the background surrounding the peak. However, the best method is to carry out an extended background run and use the data from this run to determine the parameters a, b, and c. If a rejected spectra from active shielding is available, it can also be used to determine the background shape. The fit can be scaled to the actual data by adjusting a to fit the background on the high energy side of the peak. This is the best method, since a non-negligible low energy tail can be present in the data, while energies above the peak remain unaffected. One exception to this is when pile up effects are very large. This was not found to be an issue in this experiment.

An example of performing the background subtraction can be seen in Figure 4.1. In this example, a raw spectrum from a measurement performed at 40 keV is shown. The next plot shows the result of using the anti-coincidence shield to remove most of the background and a scaled fit to a background spectra. The final result of this procedure is shown in the final plot. As can be seen, the technique does a reasonably good job of eliminating the background and leaving just the peak of interest.

4.2 Detector Efficiency

As noted in Section 3.5, due to the finite size of an actual NaI detector, some γ-rays that enter the detector fail to interact or only deposit a small fraction of their energy in the detector. Therefore, the detector isn't 100% efficient. This has two effects on the experiment. One, it results in lost counts which reduces the amount of statistics, thus increasing the error. Secondly, it must be accounted for in any absolute rates and cross sections.

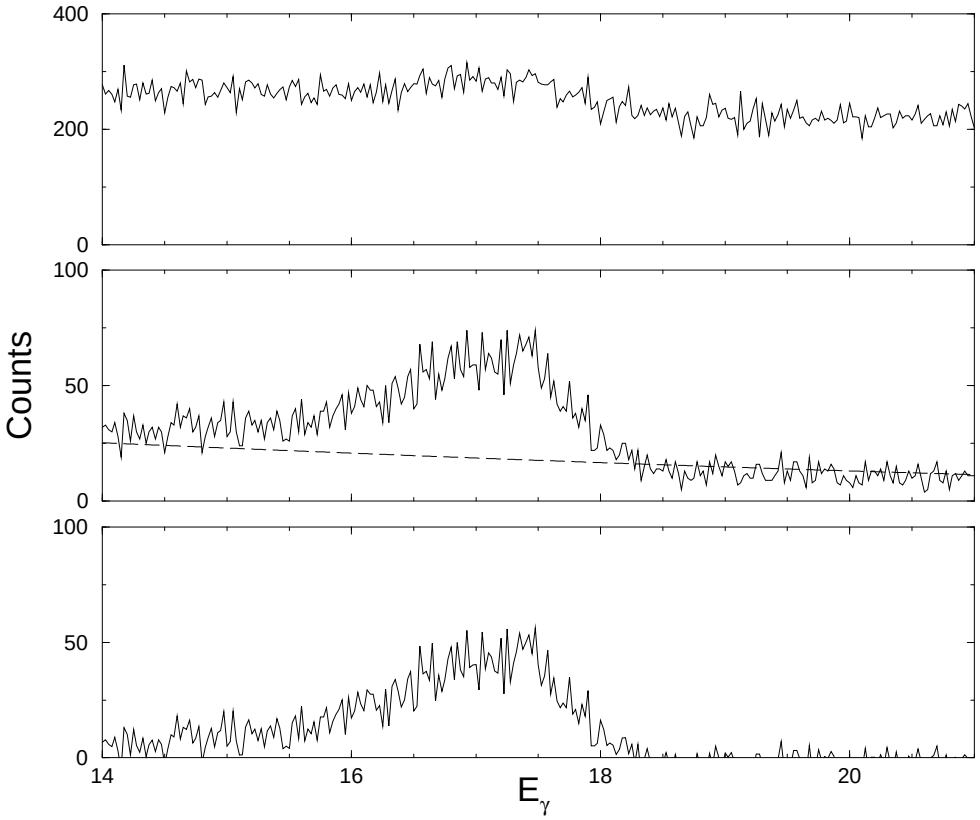

Figure 4.1: Three plots illustrating the process of background reduction for a γ-ray detector. The top figure shows the raw spectra. The middle plot is the spectra after cosmic-ray rejection and shows a fit to the background. The bottom plot is the final result.

The Monte-Carlo code, EGS4[Nel85], was used to simulate the detector for various conditions in order to determine the efficiency. EGS4 includes all of the relevant electromagnetic interactions for charged particles and photons and can handle particle energies from a few hundred keV up to several GeV. For interactions like pair-production that result in the creation of new particles, EGS4 will simulate the interaction of the new particles as well. In the past, the results from EGS4 have been carefully compared to experimental measurements and they were found to compare extremely well.

To determine the efficiency using EGS4, the experimental conditions are coded and an analysis of the output from the simulation must be performed. Describing the experimental conditions to EGS4 includes giving it the geometry and materials of the relevant objects and the initial energy of the γ-ray. Additional routines were written to properly account for phase space considerations as well as effects from the expected angular distribution of the γ-rays for $^3\mathrm{H}(\mathrm{p},\gamma)^4\mathrm{He}$. Also, since EGS4 does not include any detector resolution effects, the deposited energy had to be "smeared" to match the observed resolution. This was done by introducing an offset based on a Gaussian distribution to the energy. The width of the Gaussian distribution was adjusted to match the resolution of the detector. The efficiency was determined by taking the ratio of counts in the range from two widths below the peak to one width above the peak over the total number of cases run (see Figure 4.2). For 20 MeV γ-rays the efficiency was found to be 60%.

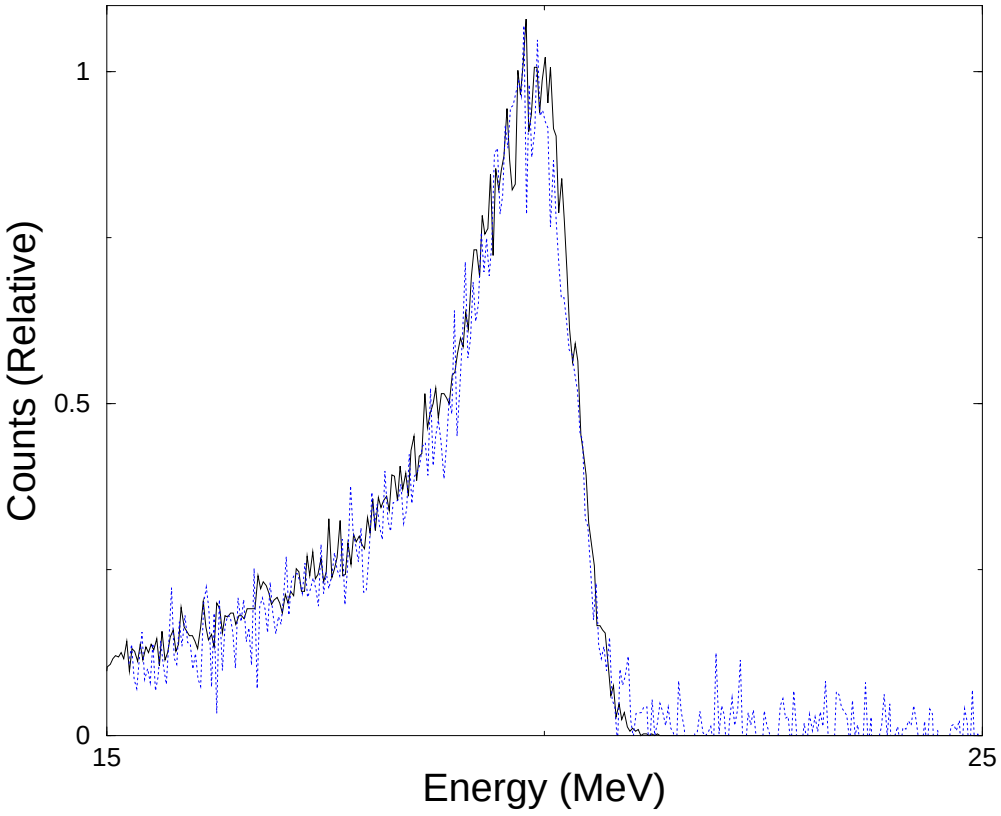

Figure 4.2: Comparison of actual spectra with simulated spectra from EGS4. The solid line is the simulated spectra. The dotted line is the actual spectra.

4.3 Differential Cross Section

Since ^{3}H(p,γ)^{4}He is predominantly an E1 reaction at low energies, the angular distribution of the cross section should be roughly $\sin^2\theta$. Since s-wave (l=0) capture is also expected due to barrier effects, the resulting M1 radiation will be isotropic, so that the form of the angular distribution of the cross section should be $\sigma(\theta) = A + B\sin^2\theta$. Measuring the relative angular distribution is fairly straight forward. Detectors are placed around the chamber at known angles. The integrated charge is carefully measured during each run. After enough statistics are collected for a group of angles, the detectors are placed at new angles. Usually, one detector is kept fixed, so that the yields can be easily normalized between the angle groupings. To determine a relative angular distribution of the cross section, corrections must be made for differences in solid angle, detector efficiency, integrated charge, and possible γ-ray attenuation effects. Most of these corrections are easily applied. The size of the detectors and their distances from the target allows the solid angle to be easily computed. Since the detectors used in this measurement were of similar size, the efficiencies are comparable within a percent and the effect can be ignored. As mentioned earlier, the integrated charge is measured for each run. Properly accounting for the attenuation effects is the only involved correction.

4.3.1 γ-ray Attenuation Effects

Correctly accounting for attenuation effects requires taking a close look at the chamber and target. Any variation in the thickness of any material through which the γ-ray must pass as a function of θ will distort the angular distribution. For the target system used in this experiment, the attenuation effects due to the target

paddle gave rise to the most significant correction. Another correction was required for the far forward angles due to a thick exit port on the chamber. To determine these corrections, the dimensions of the relevant components and their materials had to be known. Since the transmission of a γ-ray through a material is well described by the exponential relationship:

$$T = \exp(-\mu x), \tag{4.2}$$

where T is the fraction that is transmitted, μ is an absorption coefficient that depends on the material, and x is the thickness of the material [Leo94]. The absorption coefficient can be determined from various photon interaction cross sections and the material density and atomic weight. The absorption coefficients for relevant materials are given in Table 4.1.

Material	μ (cm^{-1})
Copper	0.304
Aluminum	0.0583
Sodium Iodide	0.272

Table 4.1: A summary of photon absorption coefficients for a 19.8 MeV γ-ray passing through various materials.

Due to the finite size of the detector, a γ-ray can pass through different thicknesses of materials and still be detected. To properly account for this, an integration was performed over the solid angle of the detector for the transmission. The integrated transmission for unattenuated γ-ray was also determined. Since T=1, the integrated transmission is simply the detector solid angle. The integrated transmission for the unattenuated case is divided by the attenuated case to determine the amount of correction that is required

$$C = \frac{\int 1 d\Omega}{\int\int T(\theta,\phi) d\theta d\phi}. \tag{4.3}$$

A plot of the required correction as a function of angle due to attenuation effects in the target paddle can be seen in Figure 4.3. Tests for sensitivities due to a finite beam spot and uncertainties in the distance between the detector and the target were performed. The correction was found to be very insensitive to these changes. However, uncertainty in the thickness or a lateral shift in the beam spot had a small effect on the correction. Reasonable estimates for the uncertainty in these values lead to a percentage error of 1% in the correction factor.

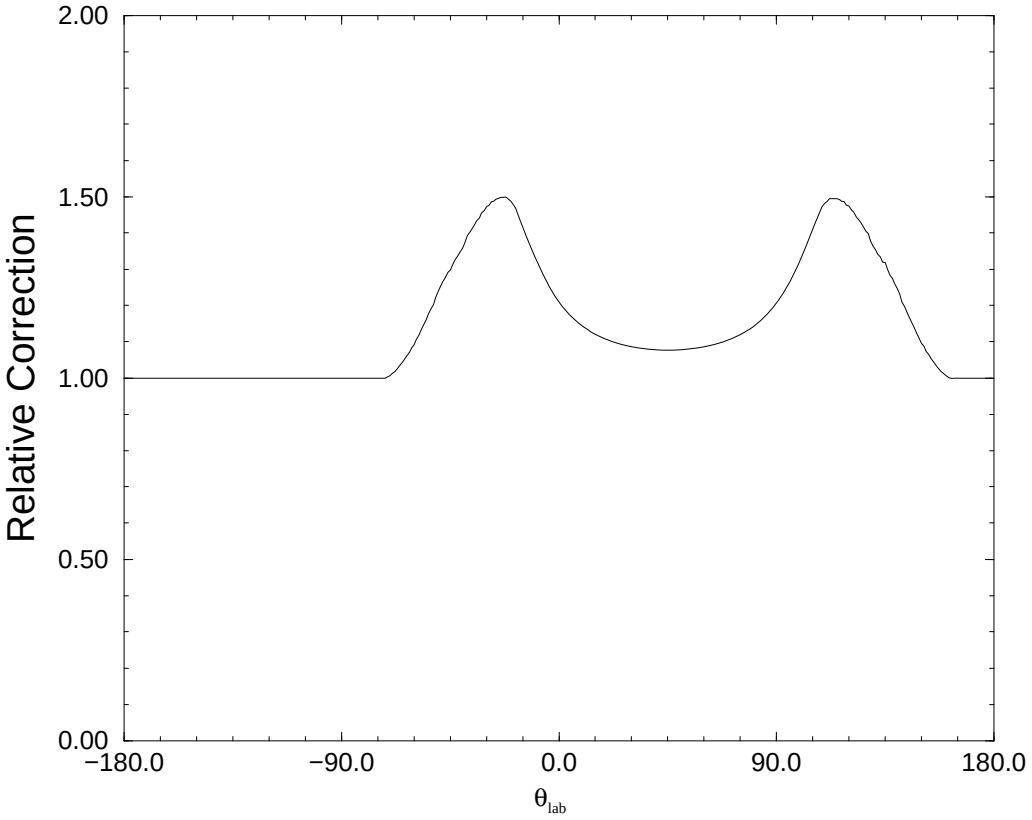

Figure 4.3: A plot of the correction required as a function of angle due to γ-ray attenuation in the copper target paddle.

4.3.2 Differential Cross Section Results

If a reference angle is chosen, here 90° has been used, the cross section at an angle θ relative to the cross section at the reference angle can be stated as:

$$\frac{\sigma(\theta)}{\sigma(90^\circ)} = \frac{\Omega(90^\circ)}{\Omega(\theta)}\frac{T(90^\circ)}{T(\theta)}\frac{C(90^\circ)}{C(\theta)}\frac{Y(\theta)}{Y(90^\circ)}, \tag{4.4}$$

where σ is the cross-section, Ω is the detector solid angle, T is the γ-ray transmission, C is the amount of beam-current integration (BCI), and Y is the yield or counts in the peak. The detector efficiencies are assumed to be the same in this equation. Plots of the angular distributions in the cross section at 40 keV and 80 keV are shown in Figure 4.4 and Figure 4.5. As expected, a strong $\sin^2\theta$ form is apparent, especially in Figure 4.5.

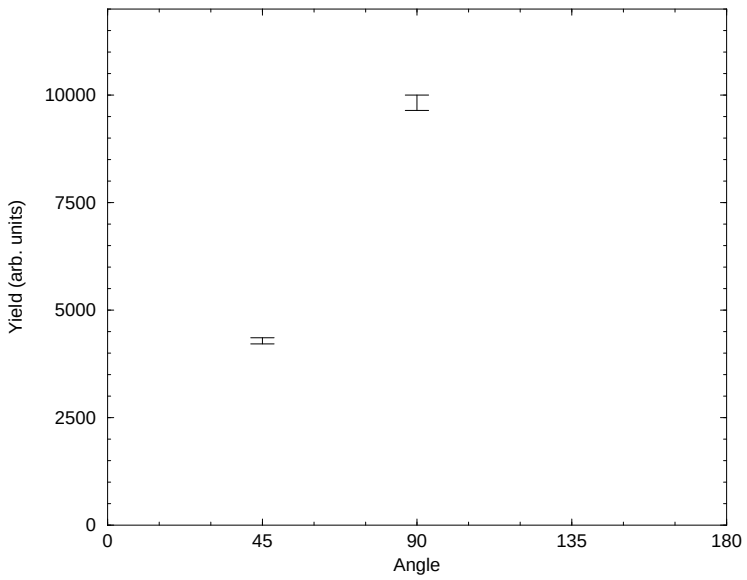

Figure 4.4: A plot of the angular distribution of the cross section for 40 keV for the ^{3}H(p, γ)^{4}He reaction. The error bars indicate the statistical uncertainties associated with the data points.

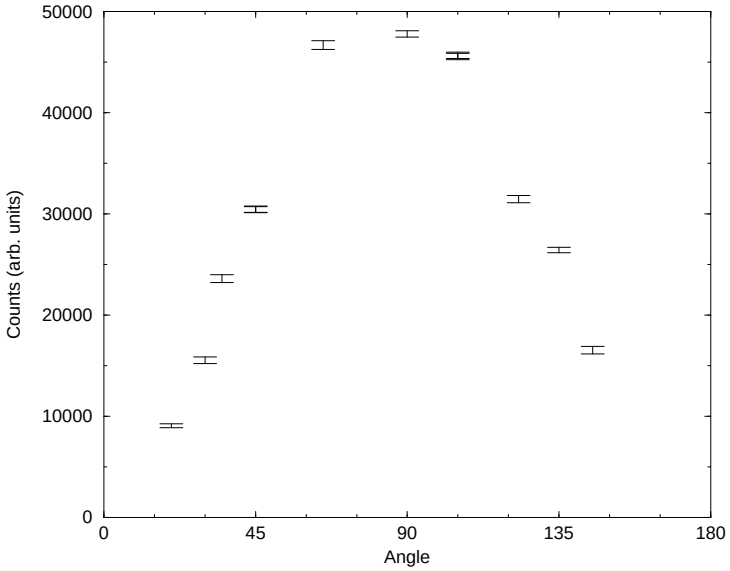

Figure 4.5: A plot of the angular distribution of the cross section for 80 keV for the $^3\mathrm{H}(\mathrm{p},\gamma)^4\mathrm{He}$ reaction. The error bars indicate the statistical uncertainties associated with the data points.

4.4 Vector Analyzing Power

The vector analyzing power describes the effect of a polarized beam on the cross section. The cross section for the case of a polarized beam can be written as:

$$\sigma_p(\theta) = \sigma_o(\theta)\left[1 + \vec{\mathrm{p}_\zeta} \cdot \vec{\mathrm{A}}(\theta)\right], \tag{4.5}$$

where σ_p is the cross section including polarization effects, σ_o is the unpolarized cross section, $\vec{\mathrm{p}_\zeta}$ is the beam polarization, and $\vec{\mathrm{A}}$ is the vector analyzing power. For the measurement of $^3\mathrm{H}(\vec{\mathrm{p}},\gamma)^4\mathrm{He}$ the beam polarization was aligned along the $\hat{y}$ direction and detectors were placed only in the plane perpendicular to $\hat{y}$ (see Figure 4.6). Under these conditions Equation 4.5 becomes:

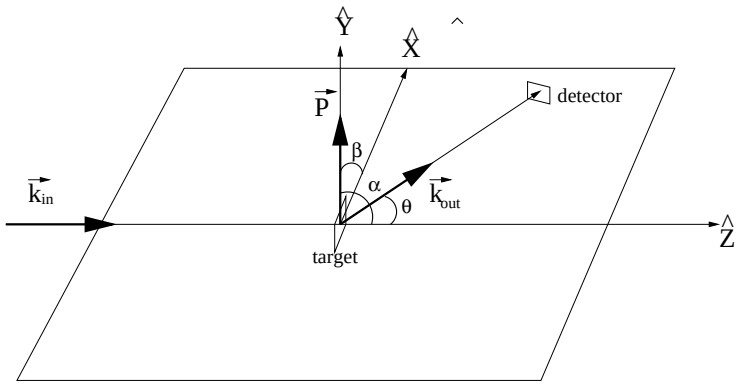

Figure 4.6: Diagram of the beam polarization and detector positions. This diagram follows the Madison Convention [BH71]. In this convention $\vec{k}_{in}$, the direction of the incident beam, defines the z axis. The y axis is defined by the cross product of $\vec{k}_{in}$ and $\vec{k}_{out}$, the direction of the outgoing γ-ray. The reaction plane, $\hat{X}$-$\hat{Z}$, is formed by $\vec{k}_{in}$ and $\vec{k}_{out}$. The angle between the detector, $\vec{k}_{out}$, and $\hat{Z}$ is defined as θ. In this case the polarization vector, $\hat{P}$, is aligned along the $\hat{Y}$ direction.

$$\sigma_p(\theta) = \sigma_o(\theta)\left[1 + \mathrm{p}_y \mathrm{A}_y(\theta)\right], \tag{4.6}$$

where p_y is the polarization of the beam along $\hat{y}$ and A_y is the component of the vector analyzing power along $\hat{y}$. During the experiment the beam polarization was flipped between two states. For the target, this corresponds to the spin aligned with $\hat{\mathrm{y}}$ and anti-aligned with $\hat{\mathrm{y}}$. If the polarization for the two states are denoted by $p_\uparrow$ and $p_\downarrow$ and the yield from each of this states is denoted as $Y_\uparrow$ and $Y_\downarrow$, Equation 4.6 can be rearranged into the following form:

$$A_y = \frac{Y_\uparrow - Y_\downarrow}{p_\downarrow Y_\uparrow + p_\uparrow Y_\downarrow}, \tag{4.7}$$

where $p_\uparrow$ and $p_\downarrow$ are both taken to be positive numbers. The raw yield can be used in place of the cross section because all of the corrections and systematic effects cancel

out, since all of these effects are incorporated in σ_o which is in both the denominator and the numerator.

For the case of ^{3}H(p,γ)^{4}He , where E1-M1 interference is expected (see Section 5.2), the product of $A_y(\theta)$ and $\sigma(\theta)$ should have a $\sin\theta$ form. This would imply that $A_y(\theta)$ should, to first order, have a $\sec\theta$ form. However, the finite size of the detectors will distort this form. A plot of the angular distribution of the analyzing power is shown in Figure 4.7 and Figure 4.8 for the two energies. Although less clear than the cross section case, the expected form is apparent, at least in the case of the 80 keV data.

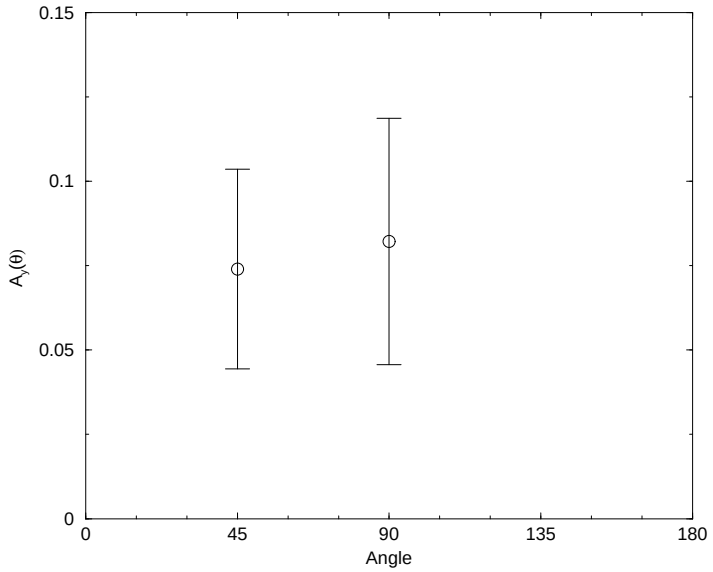

Figure 4.7: The angular distribution of the analyzing power at E_p=40 keV. The error bars represent the statistical uncertainties associated with the data points.

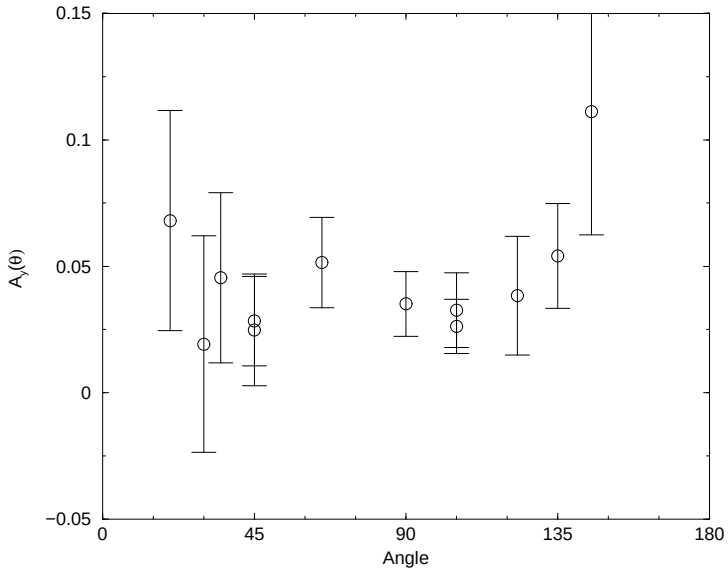

Figure 4.8: The angular distribution of the analyzing power at E_p=80 keV. The error bars represent the statistical uncertainties associated with the data points.

4.5 Absolute Cross Section

Determining absolute cross sections for nuclear reactions represents one of the most challenging tasks in nuclear physics. It requires knowledge about every aspect of the experiment, including detector efficiencies, target thickness, detector geometry, the angular distribution of the yield, dead-times, and the total amount of beam deposited on the target. In addition, the errors on all of these factors must be understood to properly assign an overall error to the measured cross section. A determination of the absolute cross section has been made for ^{3}H(p, γ)^{4}He. However, the precision of the measurement was limited due to uncertainties in the properties of the target.

4.5.1 Thick Target Considerations

A beam of low energy charged particles quickly loses energy as it passes through a target. This energy loss is a function of the stopping power of the target which defines the energy loss per unit length of material as a function of the energy of the projectile. Typical units for an energy loss might be keV/μm. The stopping power is normally given as a set of parameters for an assumed functional form. These parameters are determined by fitting the function to experimental measurements. In 1977, Andersen and Ziegler published a comprehensive list of these parameters for a variety of elements[And77]. In this study a large collection of experimental data was gathered. Various functional forms were tested until a generic form was found that was able to effectively describe all of the elements. The parameters for these functions for each element were then determined from the experimental data. The accuracy for the stopping power determined from these parameters is estimated to be around 10%.

In the present case, the target material of interest is tritium. The stopping power, however, is almost entirely determined by the titanium atoms in the target due to their higher charge. Applying the parameters for titanium, the stopping power for protons with energy between 10 keV and 999 keV is described by the following equation:

$$S_{low}(E) = A_2 E^{0.45} \tag{4.8}$$

$$S_{high}(E) = \frac{A_3}{E}\log\left(1 + A_4/E + A_5 E\right) \tag{4.9}$$

$$STP(E) = \frac{dE}{dx}(E) = \left(\frac{1}{S_{low}} + \frac{1}{S_{high}}\right)^{-1}, \tag{4.10}$$

where S is the stopping power, E is the energy of the projectile, and the A's are

Parameter	Value
A_1	4.862
A_2	5.496
A_3	5165
A_4	568.5
A_5	0.009474

Table 4.2: The stopping power parameters for titanium as determined by Zeigler *et al* assuming the parameterized form shown in Equation 4.8. The units are 10^{18} keV/cm^2.

parameters obtained from [And77]. The units for STP are energy over length. The A_n's for titanium are shown in Table 4.2.

In the case of low energy beams, the beam typically stops in the target. Therefore, the measurement is never made at just the energy of the beam. What is actually measured is the accumulated yield from 0 energy up to the beam energy. In some cases it is possible to resolve the energy at which the reaction occurred. However, in the case of this measurement the NaI detectors were not capable of resolving energy differences greater than several 100 keV. Therefore, the accumulated yield is smeared together for the various energies and the total yield is described by the following equation [Rol88]:

$$Y(\theta) = \epsilon n_p N_t \int \int_0^{E_b} \frac{d\sigma(E_p,\theta)}{d\Omega} \frac{1}{STP(E_p)} dE_p d\Omega, \tag{4.11}$$

where ϵ is the detector efficiency, n_p is the number of protons that hit the target, N_t is the atomic number density of tritium in the target, E_b is the energy of the beam, σ is the cross section, S is the stopping power, and Ω is the solid angle of the detector. Since the cross section falls off rapidly as energy decreases due the Coulomb barrier (see Equation 2.4), the energy range close to the beam energy contributes most of the

yield. In ^{3}H(p,γ)^{4}He for an 80 keV proton beam, the range from 60 keV to 80 keV contributes around half of the total yield. Equation 4.11 will be heavily employed in the next section to make a determination of the concentration of tritium in the target and to ultimately determine the cross section.

4.5.2 Determination of the Tritium Density

One parameter that must be known accurately for an absolute cross section measurement is the target density. For well behaved targets it is occasionally sufficient to compute the target density from known material densities and target composition. However, in a complex target like a tritiated disk being used at low energies, it is necessary to make some direct measurement of the target density. Often some other nuclear process which is well understood or measured is used to make this measurement. An obvious choice for the ^{3}H(p,γ)^{4}He reaction is to use ^{3}H(d,n)^{4}He as the calibration reaction. This reaction is well measured [Bro87], has a large yield at low energies and, by detecting the α-particles, can be measured with nearly 100% efficient detectors. The only drawback to this method is that two different beams must be employed. The tuning for the two beams will be different. Therefore, the beam spot's position and spatial distribution can be different. If there are large variations in the tritium loading across the surface of the target, large differences in the effective thickness for the two reactions could occur. In order to minimize this effect, broadly focused beams were used, so that most of the target surface was seen by both beams. Runs at deuteron beam energies of 40 keV, 60 keV and 80 keV were performed in order to analyze the target composition.

If the cross section is known for a reaction [Bro87], Equation 4.11 can be used to determine the density of target nuclei. If it is assumed that the target is homogeneous

and that the tritium loading extends from the surface of the target to a depth greater than the beam penetration, then Equation 4.11 can be easily inverted to determine the homogeneous tritium density. Table 4.3 summarizes the parameters used to determine the density and the results.

Parameter	E_d=40 keV	E_d=60 keV	E_d=80 keV
Solid Angle (mSR)		4.9±0.4	
Integrated Beam (mC)		6.60±0.04	
Observed Counts (10^6)	0.209	3.07	7.75
Optimum target density (nuclei/cm^3)		6.52×10^{22}	
Expected counts (10^6)	16.4	28.7	72.0
Fraction of expected counts	3.3%	10.71%	10.76%

Table 4.3: Summary of the parameters and results for the measurements of the ^{3}H(d, n)^{4}He reaction. The expected counts are based on an optimally loaded homogeneous target which has been corrected for natural decay. The statistical errors on the counts are less than half a percent.

Two discrepancies are immediately evident. One, the measured density is much lower than what is expected ($7.0 \pm 0.6 \times 10^{21}$ nuclei/cm^3 vs. 6.52×10^{22} nuclei/cm^3). Secondly, the density decreases with lower energy. Two effects are likely responsible for these discrepancies. First, a depleted layer has likely formed on the surface of the target. This could be expected because tritium near the surface could easily be sputtered out of the target. Since the depleted layer would lower the beam energy before reaching tritium nuclei and the cross section decreases with energy, the yield would be reduced. This would affect the lower energy measurements more strongly, since the beam would lose a larger fraction of its energy in the depleted layer before interacting with tritium nuclei. An overall reduction in the tritium loading would also reduce the yield. A combination of these two effects was likely responsible for the discrepancies.

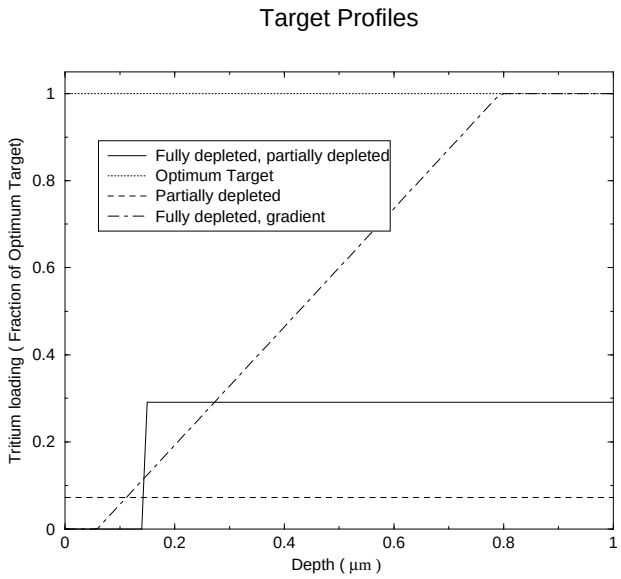

Figure 4.9: A plot of the profiles for some of the tritium density configurations that were tested. Parameters such as depletion depth and slope were adjusted for the various configurations. These plots use the parameters for the "best case" of each configuration. The y-axis is in terms of the fraction of an optimally loaded target which has been adjusted for the natural decay of tritium during the life of the target. Zero on the x-axis would correspond to the surface of the target.

In order to determine the tritium density configuration, various density profiles were tested. With each configuration relevant parameters were adjusted. A χ^2 minimization between the expected counts for the assumed form and the actual counts observed in the experiment was performed. The best cases for the various configuration were then compared. Several configurations were tried, such as various partially depleted forms, various forms involving linear gradients, and various exponential forms. Many of the forms also included some fully depleted layer. Figure 4.9 illustrates some of the forms that were tested. Parameters, such as the slope and offset for a gradient form, were varied. Ultimately it was found that a step function gave the best fit. A fully depleted region 0.15 μm thick followed by a region loaded to 0.46 tritium nuclei for each titanium nuclei gave a χ^2/ν of 1.5. Figure 4.10 illustrates the results for the

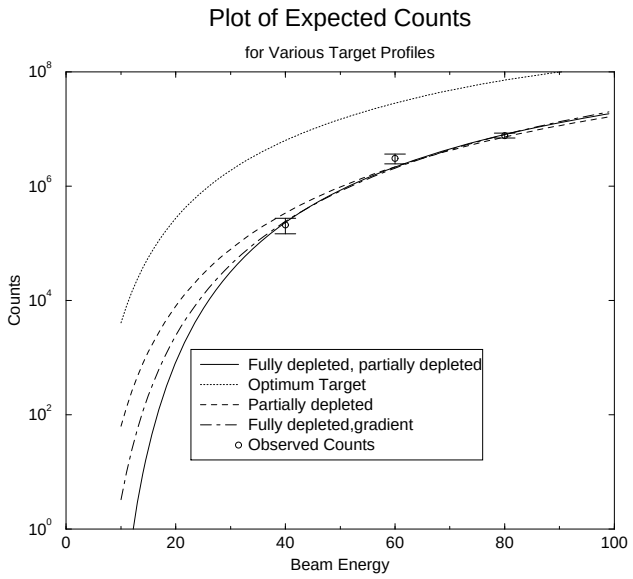

Figure 4.10: A plot of the expected counts for the various tritium density configurations shown in Figure 4.9. The counts correspond to the parameters shown in Table 4.3. The data points are the measured values. The errors bars are estimates based on the observed variation in the yield between runs. Statistical errors were negligible.

different target configurations. The form labeled "fully depleted, partially depleted" is the form that gave the best fit. This profile will be referred to as $L(d)$ in later sections. The uncertainty for the measured yields was based on an estimate of the variation in the tritium loading across the target. This was estimated to be around 5%. Other uncertainties were ignored since the yields at the different energies were compared in a relative manner for this analysis. However, the various systematic uncertainties must be accounted for in the final result. The only substantial systematic uncertainty is in the solid angle of the α-particle detector.

Folding the result from this analysis into Equation 4.11, the following is obtained:

$$Y(\theta) = \epsilon n_p N_t \int \int_0^{E_b} \frac{L(d(E))d\sigma(E_p,\theta)}{d\Omega} \frac{1}{STP(E_p)} dE_p d\Omega, \tag{4.12}$$

where L is the loading profile stated as a fraction of an optimally loaded target, $d(E)$

is the depth associated with the energy E. The relationship $d(E)$ is determined from the stopping power in the following manner:

$$d(E) = \int_{E}^{\mathrm{E}_b} \frac{dE}{STP(E)}. \tag{4.13}$$

As a result, the function $d(E)$ is also dependent on the beam energy. For this case, the beam energy is treated as a parameter.

4.5.3 Determining the Cross Section

As can be seen in Equation 4.12, a knowledge of the cross section as a function of energy is required to determine the absolute cross section of the reaction for a thick target. Consequently, a deconvolution must be performed in order to determine the cross section. For this case, a linear or quadratic form for the Astrophysical S-factor is used to describe the energy dependence of the cross section in the convolution integral. Two analyses will be presented. In the first case, the measurement from the present experiment at a proton beam energy of 40 keV and 80 keV are used to determine the parameterization of the S-factor. No other data is included in this fit. For the second case, data from [Hah95] are included in the fit. The need for including these data will be explained.

In order to extract the S-factor parameterization from the measured yields, a code which uses the MINUIT minimization package was written. First, the yields are normalized by correcting them for differences in solid angle, total integrated beam, detector efficiency, and γ-ray attenuation effects. The normalized yields are then input into the code. The code assumes some initial values for the S-factor parameters. It then performs the integral shown in Equation 4.12. Corrections for the tritium density obtained in Section 4.5.2 were also performed. For the case where only the

new data are used, the code computes the following:

$$\epsilon = \sum_i \left(\frac{Y_i - Y(S_0, S_1, E_i)}{\Delta Y_i} \right)^2 \tag{4.14}$$

where Y_i is a measured normalized yield, $Y(S_0, S_1, E_i)$ is the normalized result of Equation 4.12, E_i is the beam energy corresponding to the measured yield (Y_i), and ΔY_i is the uncertainty in the corresponding normalized yield. The parameters (S_0 and S_1) are adjusted in order to minimize ϵ. Notice that a linear parameterization is assumed (i.e. $S(E_{cm}) = S_0 + S_1 E_{cm}$). This is both reasonable, since the measurements were performed at low energies where the dependence is expected to be fairly linear, and necessary, since a quadratic form would have too many free parameters. The resulting fit agrees within uncertainty with previous parameterizations of the S-factor. However, due to the large uncertainties in the fit, the result is of limited value. The uncertainty in the slope of the S-factor is especially large. This is expected, since determining the slope requires taking the difference between two data points that are close together and have large uncertainties. The fit can be improved by simply including data at higher energies.

The second case combines the present measurements with data from Hahn *et al* to obtain a more accurate result. A table of the extracted differential cross sections with uncertainties, beam energy, and average beam energy is presented in [Hah95]. For this analysis, these data are converted to S-factors. In a manner similar to that described above, the code determines the following value:

$$\epsilon = \sum_i \left(\frac{Y_i - Y(S_0, S_1, S_2, E_i)}{\Delta Y_i} \right)^2 + \sum_j \left(\frac{S_j - S(S_0, S_1, S_2, E_j)}{\Delta S_j} \right)^2 \tag{4.15}$$

where the first term is the same as above with the exception that the function Y now includes a quadratic term (S_2), S_j is an S-factor from [Hah95], $S(S_0, S_1, S_2, E_j)$ is the computed S-factor at energy E_j (assuming the parameters S_0, S_1, and S_2),

E_j is the CM energy corresponding to the previously measured S-factor, and ΔS_j is the corresponding uncertainty in the measured S-factor. Notice that now a quadratic parameterization for the S-factor is assumed, i.e. $S(E_{cm}) = S_0 + S_1 E_{cm} + S_2 E_{cm}^2$. The quadratic term is included since higher energy data suggest some quadratic dependence in the S-factor and, by including the Hahn data, there is enough data to properly determine this dependence. The parameters were then adjusted in order to minimize ϵ. Also, note that the sums in Equation 4.15 are over two different types of measurements. The first sum uses yields and the second sum uses extracted S-factors. However, both sets are weighted by the inverse of their associated uncertainties, so the results are dimensionless.

One potential flaw to this approach is that the Hahn data were also taken at relatively low energies, although not as low as the current experiment. Therefore, the extracted cross sections make some assumptions about the form of the S-factor. If our results had disagreed with these assumptions, then the extracted results might require reexamination. Details about their target and how the yields were measured might be required in order to properly deconvolute their results. However, since both groups of measurements agree, this was deemed unnecessary and their extracted cross sections were used.

The results for both fits are summarized in Table 4.4 and Figure 4.11. For reference purposes, S-factors from Caughlan *et al* [Fow67], as well as a parameterized fit to the Hahn data [Hah95] are included. For the purposes of this plot, the average beam energy has been used for the present data points. Since the beam stops in the target, assuming the beam energy is not appropriate. The depleted layer, which was described in Section 4.5.2, also complicates matters. The standard approach for low energy measurements is to state the average beam energy. This is determined by

Source	S_0 keV mb	S_1 mb $\times 10^{-2}$	S_2 mb/keV $\times 10^{-4}$
Caughlan *et al* [Fow67]	2.56	3.87	1.14
Hahn *et al* [Hah95]	1.8	2.0	0.96
New data only (linear)	1.5±0.4	6.0±3.0	N/A
New data and Hahn data	2.0±0.2	1.6±0.4	1.1±0.3

Table 4.4: Summary of S-factors from this measurement and previous measurements. An explanation is given in the text.

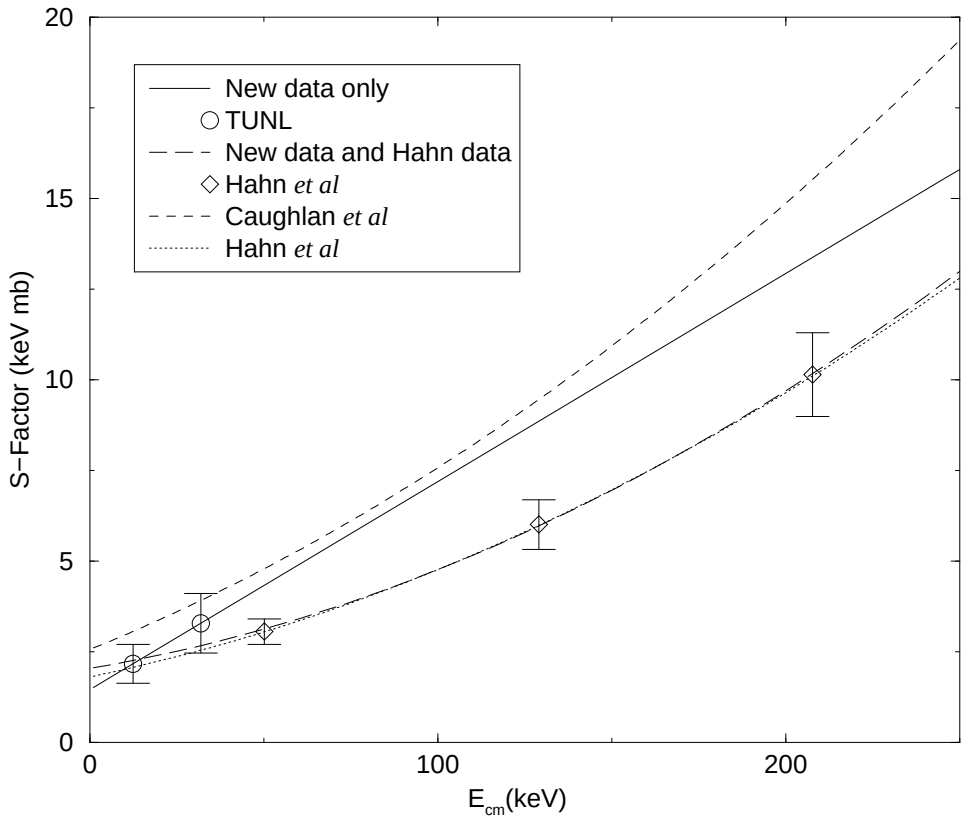

Figure 4.11: A plot of the new parameterization of the astrophysical S-factor. The new data points are determined from a linear parameterization. The error bars include statistical and systematic uncertainties. Data points for measurements by Hahn *et al* are plotted along with a fit. In addition, the parameterization of Caughlan *et al* is shown.

E_{cm} keV	S-factor ev b	σ_t μb	$\sigma(90\ ^\circ)$ μb/sr.
10.0	2.17	0.04	0.005
20.0	2.36	0.27	0.032
30.0	2.58	0.60	0.072
40.0	2.82	0.96	0.114
50.0	3.08	1.32	0.157
60.0	3.36	1.67	0.200
70.0	3.66	2.03	0.242
80.0	3.99	2.39	0.285
90.0	4.34	2.74	0.328
100.0	4.71	3.11	0.371

Table 4.5: Table of the cross sections and S-factors using the adopted parameters for the S-factor shown on the last line of Table 4.4.

performing the integral in Equation 4.12 from zero energy up to an energy where half of the total yield has been accumulated. One disadvantage of this method is that the result will depend on the form of the S-factor. For example, a positive slope in the S-factor would shift the average beam energy up. Due to the depleted layer that was described in the previous section, the average beam energy will be shifted down substantially. In fact, the depleted layer absorbs approximately 15 keV of an 80 keV beam.

4.5.4 Error Analysis

The errors in the determination of the absolute cross section are almost entirely due to the systematic errors. This is typical for an experiment which has a reasonable count rate like that in the present study of the ^{3}H(p,γ)^{4}He reaction. The systematic uncertainties can be split into two groups. One group includes the uncertainties related to the determination of the tritium density in the target and the other group

includes uncertainties related to measuring the ^{3}H(p,γ)^{4}He reaction.

Sources for uncertainties in determining the tritium density include determining the solid angle of the solid state detector, extracting the density from the yields, and time-dependent variations in the tritium loading within the target. The latter was clearly the most significant source of uncertainty and was also the most difficult to assign, since there is no direct measure of it. It was ultimately decided that the variation in yield that was observed between the first run with a new target and the final run was the best measure of this uncertainty. A variation of approximately 20% was observed. The uncertainty in extracting the density from the measured yields was also difficult to assign. This uncertainty was estimated to be 15% after observing the effect of using the different loading profiles detailed in Section 4.5.2 on the extracted cross section. The other source of uncertainty came from determining the solid angle of the solid state detector. This uncertainty was somewhat large due to the geometry of the setup. All of these uncertainties were combined in a quadrature. This result was then used as a single source of uncertainty in extracting the cross section from the γ-ray yields for the ^{3}H(p,γ)^{4}He reaction.

The other sources of uncertainty in the determination of the cross section are related to measuring the γ-ray yield for the ^{3}H(p,γ)^{4}He reaction. This includes uncertainties in the solid angle of the NaI detector and its efficiency. Other sources of systematic uncertainties which were determined to be negligible include the uncertainty in the total charge collected, yield extraction and background effects in the spectra, and the γ-ray attenuation. A summary of the uncertainties are shown in Table 4.6. The total error comes from all of the errors taken in quadrature. This result was then used as the uncertainty for the yields which were input into the S-factor fitting routine detailed in Section 4.5.3. Consequently, these errors determine

Tritium density	
Source	Uncertainty
Target variation	20%
Extracting density	15%
Solid Angle (α-particle detector)	8.6%
Total	26.4%

Cross section	
Source	Uncertainty
Tritium density	26.4%
Solid Angle (NaI detector)	5.0%
Efficiency (NaI detector)	5.0%
Statistical	2.0%
Total	27.4%

Table 4.6: Summary of the uncertainties for the absolute cross section measurement. The top section details source of uncertainty related to determining the tritium density in the target. The bottom section details the sources of uncertainty in determining the cross section. Other uncertainties, such as uncertainties in the total charge collected, yield extraction, and the γ-ray attenuation were determined to be negligible.

the uncertainties for the parameters shown in Table 4.4.

Chapter 5

Analysis of the Data

In the previous section, the process of extracting the cross section and analyzing powers was described. While these representations are useful and can be compared with theoretical results, it is also useful to present them in forms that can be more critically compared with theories and from which we can obtain physical insight. A transition matrix element (TME) analysis was performed on the data to extract the complex TMEs for the $^3\mathrm{H}(\vec{\mathrm{p}},\gamma)^4\mathrm{He}$ reaction. These TMEs can be compared to simple theories available now, and in the future the results can be compared to more sophisticated theories that are under development.

5.1 Legendre Polynomial Expansion

Once the angular distributions for the analyzing power and the cross section have been extracted from the data, they can be expanded in terms of Legendre polynomials. This is useful because the order of the expansion can be related to an expansion in

units of angular momentum of the transitions that are involved in the reaction. By studying the significance of individual Legendre polynomials in the expansion, it is possible to infer which transitions are likely to be involved in the process.

An expansion of the unpolarized cross section in terms of Legendre polynomials can be performed and results in the following form,

$$\sigma(\theta) = \left(\frac{\lambda\!\!\!^{-2}}{4(2x+1)(2a+1)}\right) \sum_{k=0}^{n} \mathrm{Q}_k \mathrm{a}_k \mathrm{P}_k(\cos\theta) \tag{5.1}$$

where Q_0 and P_0 are defined to be 1, $\lambda\!\!\!^{-}$ is the reduced wavelength of the incident particle, x is the spin of the incident particle, a is the spin of the target nucleus, Q_k are the finite geometry correction factors (see Section 5.1.1), a_k are the Legendre polynomial coefficients, and P_k are the Legendre polynomials. Similarly, the product of the cross section and the analyzing power can be expanded in terms of first associated Legendre polynomials. This results in the following,

$$\sigma(\theta)\mathrm{A}_y(\theta) = \left(\frac{\lambda\!\!\!^{-2}}{4(2x+1)(2a+1)}\right) \sum_{k=0}^{n} \mathrm{Q}_k \mathrm{b}_k \mathrm{P}_k^1(\cos\theta). \tag{5.2}$$

In both Equation 5.1 and Equation 5.2, the sums are carried out up to some value n. For an exact solution this would entail summing to infinity. However, at even moderate energies (less than several MeV), this series can be truncated. At low energies, such as those used in the current experiment, only a few terms are typically needed to describe the data to within the errors of the measurements. This is because as the energy is reduced, the barrier created by the relative orbital angular momentum, l, limits the values of l which are significantly involved. Since k is determined by l ($k \leq 2l$), only a few terms are required in these expansions at very low energies. At energies below a 100 keV, limiting the sum to a k of 2 or 3 is often sufficient.

The total cross section, σ_T, can be determined by integrating Equation 5.1 over all angles θ and ϕ to arrive at the following form,

$$\sigma_T = \int_0^{2\pi} \int_0^{\pi} \sigma(\theta) \sin\theta \; d\theta \; d\phi = 4\pi \left(\frac{\lambda\!\!\!^{-2}}{4(2x+1)(2a+1)} \right) \mathrm{a}_0 \tag{5.3}$$

If the following definition is made,

$$\mathrm{A}_0 = \left(\frac{\lambda\!\!\!^{-2}}{4(2x+1)(2a+1)} \right) \mathrm{a}_0 \tag{5.4}$$

then the total cross section can be stated as follows,

$$\sigma_T = 4\pi \mathrm{A}_0. \tag{5.5}$$

5.1.1 The Q_k Coefficients

As was mentioned above, one aspect of the experiment that must be taken into account during the analysis is the finite size of the detectors. While a measurement made by a detector is often used to describe an observable for a specific angle, a detector's finite size causes it to include a range of angles. If a detector covers a large solid angle because it is large or very close to the target, the finite size may have a dramatic effect on the result. The Q_k coefficients shown in Equation 5.1 correct for finite detector geometry effects. This can be done because of mathematical properties of the Legendre polynomials. For a more complete discussion see [Ros53, Fer65]. The Q_k coefficients are defined as follows,

$$\mathrm{Q}_k = \frac{\mathrm{J}_k}{\mathrm{J}_0} \tag{5.6}$$

where

$$\mathrm{J}_k = \int_0^{\pi} \epsilon(\beta) \mathrm{P}_k \; \mathrm{d}(\cos\beta), \tag{5.7}$$

β is the angle of incidence of the γ-ray with axis of symmetry for the γ-ray detector, and $\epsilon(\beta)$ describes the probability of detection of the γ-ray for the angle β.

The probability of detection is described fairly well by using the γ-ray attenuation coefficients for the detector material. Using this method leads to

$$\epsilon(\beta) = 1 - e^{-\tau x(\beta)} \tag{5.8}$$

where τ is the γ-ray attenuation coefficient and $x(\beta)$ is the detector thickness corresponding to the angle β. For NaI, τ is 0.272 cm^{-1} for a 19.8 MeV γ-ray. For an uncollimated detector (see Figure 5.1) which is a distance d from the target, has a radius r, and a thickness t, the path length is the following,

$$\begin{aligned} x(\beta) &= \frac{t}{\cos\beta} \qquad \text{when} \quad \tan\beta < \frac{r}{d+t} \\ x(\beta) &= \frac{r}{\sin\beta} - \frac{d}{\cos\beta} \qquad \text{when} \quad \tan\beta < \frac{r}{d} \text{ and } \tan\beta > \frac{r}{d+t} \\ x(\beta) &= 0 \qquad \text{when} \tan\beta > \frac{r}{d}. \end{aligned} \tag{5.9}$$

Studying Equation 5.6, Equation 5.8, and Equation 5.9, it can be seen that as the detector is placed further away, the integral is performed over a more shallow range of β and the Q_k's will get closer to 1. This is as it should be, since the Q_k's are a measure of how point-like the detectors are. For a true point detector, all of the integrals would be 0 and, in this limit, all the Q_k's would be 1. Also, it can be seen that if the detectors are collimated, the integral is only performed over a region where the probability of detection is largest (since the thinner sections are not included). This has the same overall effect as moving the detectors back, since it leads to larger Q_k's.

To give an idea of the magnitude of the Q_k's for a typical detector, Table 5.1

k	Q_k uncollimated	Q_k collimated
0	1.0	1.0
1	0.96	0.97
2	0.88	0.92
3	0.77	0.85

Table 5.1: Q_k's for a 10" x 10" NaI detector placed 10" from the target.

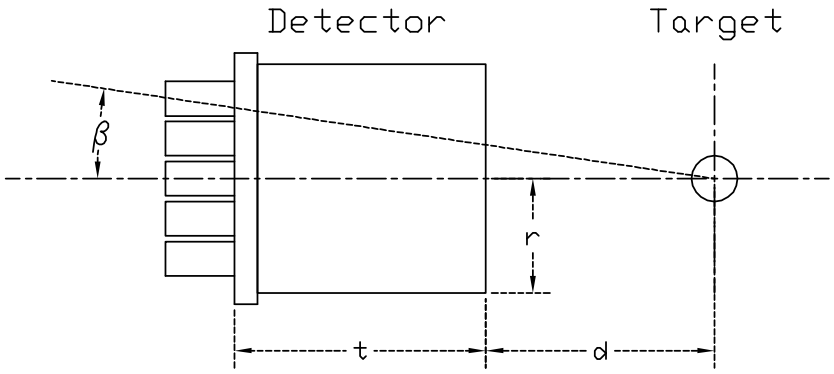

Figure 5.1: Illustrations of the dimensions used in the computation of the Q_k coefficients.

shows the Q_k's for a collimated and uncollimated 10"x10" NaI detector placed 10" from a target, where the collimated detector is collimated in such a manner that the back face of the detector is fully illuminated.

5.1.2 Extracting the Legendre Coefficients

Finding the appropriate Legendre polynomial coefficients for a data set requires performing a matrix inversion of a matrix constructed from the data. To understand why this matrix inversion works, consider performing a χ^2 fit of the data to a Legendre polynomial expansion. Since the expansion of $\sigma(\theta)$ and $A_y(\theta)\sigma(\theta)$ are linear with the a_k's and b_k's, minimizing the χ^2 simply requires finding where the first derivative of the χ^2 is 0. The χ^2 for $\sigma(\theta)$ can be stated as follows,

$$\chi^2 = \sum_t \frac{\left(\frac{A_0}{a_0}\sum_k Q_k a_k P_{k,t}(\cos\theta) - \sigma_t\right)^2}{(\Delta\sigma_t)^2}, \tag{5.10}$$

where the subscript t denotes the measurement that would have a lab angle θ_t, cross section σ_t, and an error $\Delta\sigma_t$. Following the prescription laid out above, taking the first derivative of Equation 5.10 with respect to a_m and setting it equal to 0, the following equation is obtained,

$$\sum_k \sum_t (a_k)\left(\frac{A_0 P_{k,t} P_{m,t}}{(\Delta\sigma_t)^2}\right) = \sum_t \left(\frac{\sigma_t P_{m,t}}{(\Delta\sigma_t)^2}\right). \tag{5.11}$$

Equation 5.11 can be restated in matrix form as

$$a\mathbf{B} = c \tag{5.12}$$

where from Equation 5.11 a is the vector of the a_k coefficients, $\mathbf{B}$ is a matrix of the (k, m) elements in the second parenthesis on the left hand side, and c is the vector of m elements on the right hand side. Stated in this form, the solution for the a_k's is simply,

$$a = c\mathbf{B}^{-1}. \tag{5.13}$$

where $\mathbf{B}^{-1}$ is the inverse of $\mathbf{B}$.

The errors for the a_k's, Δa_k, can be determined by computing the variances in the a_k coefficients. If the matrix $\mathbf{D}$ is defined as $\mathbf{B}^{-1}$, then the following relation can be made,

$$a_k = \sum_m \sum_t \frac{\sigma_t P_{m,t}}{(\Delta\sigma_t)^2} \mathbf{D}_{m,k}. \tag{5.14}$$

The variances of the a_k coefficients can then be stated as follows,

$$(\Delta a_k)^2 = \sum_{m,m'} D_{m,k} \left[\sum_{t,t'} \frac{P_{m,t} P_{m',t'}}{(\Delta\sigma_t)(\Delta\sigma_{t'})} \right] D_{m',k}. \tag{5.15}$$

Since the errors for the different angles are uncorrelated, Equation 5.15 can be simplified as follows,

$$(\Delta a_k)^2 = \sum_{m,m'} D_{m,k} \left[\frac{P_{m,t} P_{m',t}}{(\Delta\sigma_t)^2} \right] D_{m',k}. \tag{5.16}$$

The quantity in brackets is simply the matrix $\mathbf{B}$ divided by A_0. Since $\mathbf{B}$ is also the inverse of $\mathbf{D}$, Equation 5.16 simplifies as follows,

$$(\Delta a_k)^2 = \frac{1}{A_0} \sum_{m,m'} D_{m,k} D^{-1}_{m,m'} D_{m',k} = \frac{1}{A_0} \sum_{m,m'} D_{m,k} \delta_{m,k} = \frac{D_{k,k}}{A_0}. \tag{5.17}$$

Thus the errors in the a_k coefficients are simply the diagonal elements in the $\mathbf{D}$ matrix divided by A_0.

Coefficient	80 keV (unconstrained)	80 keV (constrained)	40 keV (constrained)
a_1	0.003±0.002	0.0 (fixed)	0.0 (fixed)
a_2	1.045±0.002	1.045±0.002	1.049±0.012
b_1	0.056±0.021	0.053±0.021	0.101±0.065
b_2	-0.001±0.010	0.0 (fixed)	0.0 (fixed)
χ^2/ν in $\sigma(\theta)$	9.68	8.95	1.90
χ^2/ν in $\sigma(\theta)\mathrm{A}_y(\theta)$	0.11	0.14	0.22

Table 5.2: Summary of coefficients for Legendre Polynomial expansion for data taken at a beam energy of 80 keV ($\tilde{\mathrm{E}}_{cm}$=31.15keV) and 40 keV ($\tilde{\mathrm{E}}_{cm}$=12.26 keV).

A similar procedure can be performed to determine the b_k coefficients. Obviously the appropriate substitutions must be made, such as substituting $\mathrm{A}_y(\theta)_t\ \sigma(\theta)_t$ for $\sigma(\theta)_t$ and the 1st associated Legendre polynomials for the regular Legendre polynomials. The Q_k factors are the same for the associated Legendre polynomials as for the regular Legendre polynomials.

After performing the analysis described above on the data obtained at a beam energy of 40 keV and 80 keV, the results summarized in Table 5.2 were obtained. The table summarizes several fits and the χ^2 per degree of freedom for each case. In one fit, several terms have been ignored or fixed in this expansion based on some assumptions about the reaction. Fixing a_1 to 0.0 amounts to not allowing a fore-aft asymmetry in the expansion of the cross section. For this asymmetry to come about, certain transitions must contribute which are expected to be heavily suppressed. As can be seen from the magnitude of a_1 in the unconstrained expansion, this assumption appears to be reasonable, although a_1 is over one standard deviation away from being equal to zero. The smaller total χ^2/ν also supports this assumption. The justification for limiting the expansion to only the first few terms comes from the assumption that higher order terms will be heavily suppressed due to the large angular momentum

barrier. Only the constrained fit is performed for the E_b=40 keV data due to number of data points. Plots of the constrained expansion of the 80 keV data along with the data are shown in Figure 5.2. Plots of the constrained expansion of the 40 keV data along with the data are shown in Figure 5.3.

5.2 Transition Matrix Element Expansion

The ultimate goal of an experiment is to understand the physics involved in a system and to test current theories against these observations. Therefore it is desirable to represent the observations in a form that gives some understanding of the underlying dynamics and that can be easily compared with theoretical predictions. An expansion in transition matrix elements is a standard representation employed in nuclear physics.

A TME expansion attempts to write the reaction as a set of amplitudes and phases of the relevant transition matrix elements. Each of these elements is identified by its quantum numbers in the channel spin coupling scheme for the continuum state. In this scheme the individual spins of the target and projectile nuclei couple to a channel spin, s. The relative orbital angular momentum between the two bodies, l, couples with the channel spin to give a total spin for the system, J. A given matrix element can be described by these three quantum numbers, l, s, and J, along with the mode (E or M) and multipolarity (1,2,3,etc.) of the electromagnetic transition to the final state.

The TMEs can be projected into a Legendre polynomial expansion [Sey79]. The

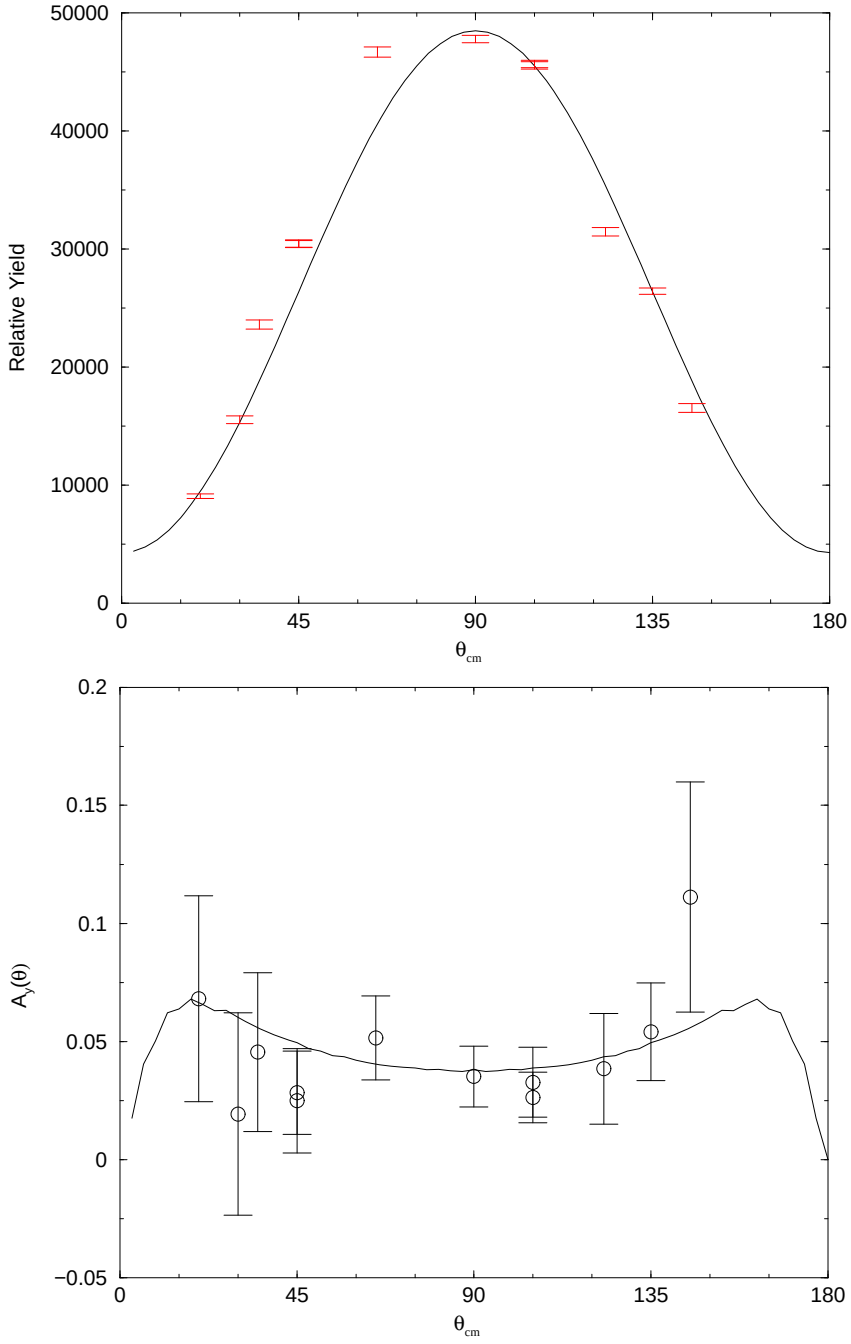

Figure 5.2: The solid lines are the results of the constrained Legendre polynomial fits to the extracted data at a beam energy of 80 keV for the angular distribution of the cross section (top) and of the analyzing power (bottom). The results are summarized in Table 5.2. The error bars account for the statistical uncertainty associated with the data points.

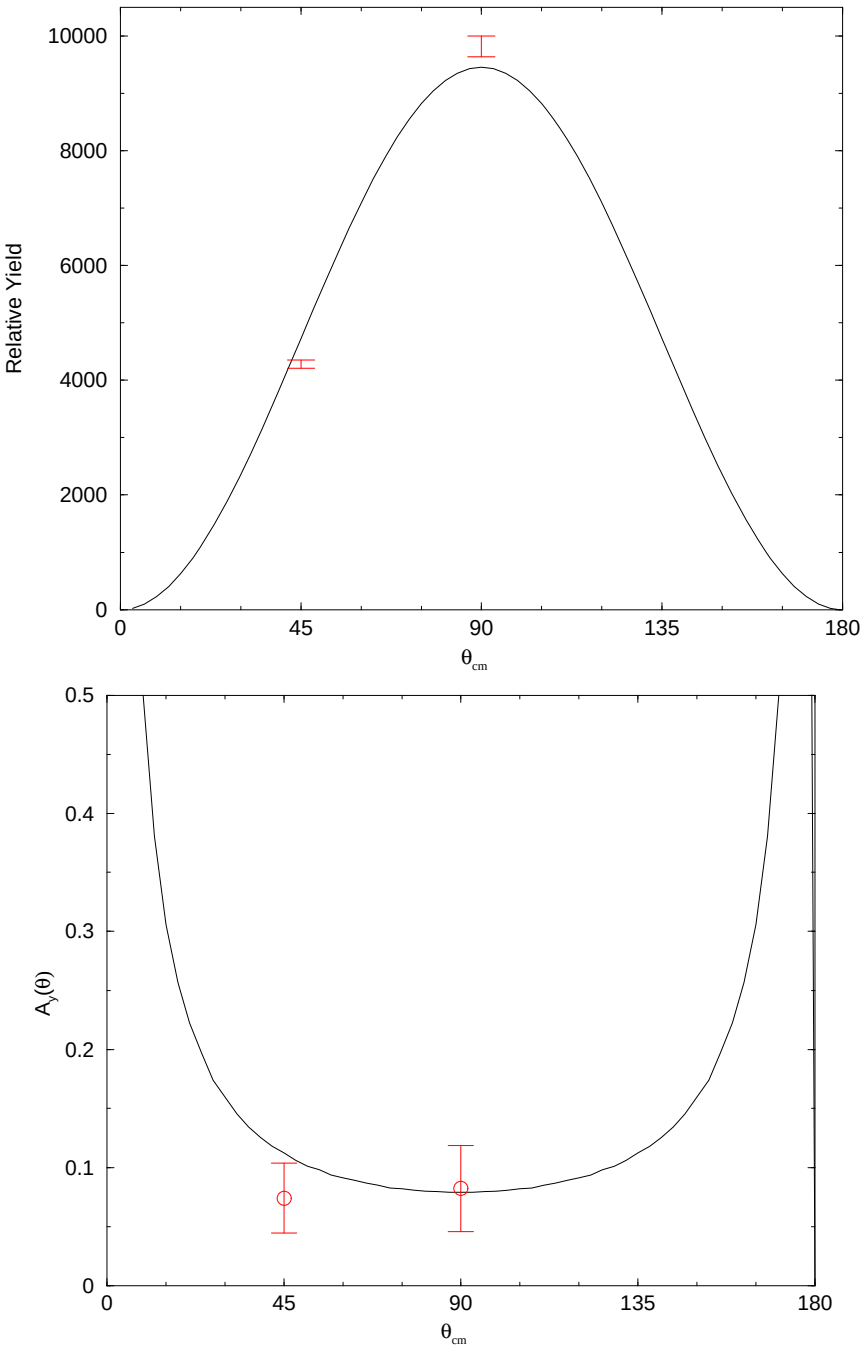

Figure 5.3: The solid lines are the results of the constrained Legendre polynomial fits to the extracted data at a beam energy of 40 keV for the angular distribution of the cross section (top) and of the analyzing power (bottom). The results are summarized in Table 5.2. The error bars account for the statistical uncertainty associated with the data points.

following results are found for the ^{3}H(p,γ)^{4}He reaction:

$$A_0 = 3(|^1\mathrm{P}_1|^2 + |^3\mathrm{P}_1|^2 + |^3\mathrm{S}_1|^2) \tag{5.18}$$

$$a_1 = -\sqrt{54}|^3\mathrm{P}_1||^3\mathrm{S}_1|\cos(\phi_{^3\mathrm{P}_1} - \phi_{^3\mathrm{S}_1}) \tag{5.19}$$

$$a_2 = -3|^1\mathrm{P}_1|^2 + \frac{3}{2}|^3\mathrm{P}_1|^2 \tag{5.20}$$

$$b_1 = -\sqrt{27}|^1\mathrm{P}_1||^3\mathrm{S}_1|\sin(\phi_{^1\mathrm{P}_1} - \phi_{^3\mathrm{S}_1}) + \sqrt{\frac{27}{2}}|^3\mathrm{P}_1||^3\mathrm{S}_1|\sin(\phi_{^3\mathrm{P}_1} - \phi_{^3\mathrm{S}_1}) \tag{5.21}$$

$$b_2 = \sqrt{\frac{9}{2}}|^1\mathrm{P}_1||^3\mathrm{P}_1|\sin(\phi_{^1\mathrm{P}_1} - \phi_{^3\mathrm{P}_1}) \tag{5.22}$$

where the amplitudes are presented using the notation $^{2S+1}l_J$ and the associated phase is denoted in a similar manner. Also, note that the ^{3}d$_1$ M1 transition has been dropped for simplicity. A justification for this omission will be given later. A few observations can be made about this expansion. One, the coefficient a$_0$ (Equation 5.1) can be written as follows:

$$\mathrm{a}_0 = \sum^{t}(2J+1)\,|R_t|^2\,. \tag{5.23}$$

Secondly, the a$_k$'s depend on the real part of the product of the matrix elements (Re T T'*), while the b$_k$'s (Equation 5.2) depend on the imaginary part of the product of the matrix elements (Re (iT T'*)). This implies that the a$_k$'s will depend on the cosine of the relative phase between two TMEs, while the b$_k$'s will depend on the sine of the relative phase between the two TMEs. Since the expansion of $\sigma(\theta)$ depends on the a$_k$ coefficients (Equation 5.1), it will depend on the cosine of the relative phases as well. Likewise, since the expansion of $\sigma(\theta)\mathrm{A}_y(\theta)$ involves b$_k$ coefficients (Equation 5.2), it will depend on the sine of the relative phases.

5.3 TMEs for the ^{3}H(p,γ)^{4}He reaction

Before proceeding with the TME analysis, the relevant terms need to be specified. Angular momentum and parity conservation can be used to restrict the elements involved in the expansion. Furthermore, from studying the Legendre polynomial expansion of the observables and considering the energy of the reaction, the magnitude of the relative angular momentum, l, can be limited.

In ^{3}H(p,γ)^{4}He, the spin of the proton, $i^\pi = 1/2^+$, couples with the spin of the triton, $I^\pi = 1/2^+$, to give a "channel spin" of S=0 or 1. This combines with the relative orbital angular momentum, l, to give a total angular momentum of the scattering state, J $(= l + s)$. Parity is also conserved. The parity of the continuum state is given by the parity of the relative orbital angular momentum, $(-1)^l$, since the intrinsic parity of both the proton and triton are positive. These continuum states then undergo a transition to the ground state of ^{4}He, $J^\pi = 0^+$ by emitting a γ-ray. The ground state of ^{4}He is known to be dominated by the $(1s_{1/2})^4$ configuration, which is the $^1S_0$ configuration in L-S coupling. At low energies, such as the energies used in this experiment, typically s-wave capture dominates. This is due to the angular momentum barrier created by higher order transitions. However, since there are no s-wave E1 transitions, p-waves, which permit E1 transitions, must be considered. It is important that E1 transitions be allowed since electric terms are typically stronger than their magnetic counterpart. There are two transitions that allow an electric dipole transition for small l. One of these transitions has a $\Delta S = 1$, which is referred to as a spin-flip E1. It can be shown that the ratio of the amplitude for the spin-flip to non-spin-flip E1 transitions is roughly given by: $E_\gamma/m_p \sim 1/50$ [Bri68]. Since the cross section depends on the square of the TMEs, the contribution to the cross

section will be approximately 1/2500, which can reasonably be neglected.

The M1 transitions are also expected to contribute to the reaction, since the only allowed transition following s-wave capture corresponds to an M1 transition. However, as discussed earlier, a quasi-orthogonality exists in the case of M1 transitions if one only considers one-body current operators. This orthogonality reduces the overall M1 strength, since nearly all of the M1 strength must come from two-body current effects. Therefore the M1 strength could be small depending on the magnitude of the two-body currents.

A summary of the transitions that will be considered in the TME fit and their expected strength are shown in Table 5.3.

Scattering state	Corresponding Transition	Comments
$^3S_1$	M1	Could be small due to quasi-orthogonality
$^3P_1$	E1	Spin-flip, small
$^1P_1$	E1	Expected to dominate

Table 5.3: A summary of the transitions that are considered in the TME analysis.

5.3.1 Performing the TME Fit

A fit was performed on the data in order to determine the TME parameters. The fit was performed using MINUIT, the minimization package from CERN. The code takes an initial set of parameters (amplitudes and phases) and, using precomputed angular momentum coupling coefficients, determines the cross section and analyzing power as a function of angle. The angular distributions for the initial set of parameters are then compared with the measured angular distributions and a χ^2 is computed. The parameters are varied until a local minimum is found in the χ^2. The parameters

for this minimum are then returned.

5.4 TME Analysis Results

If the spin-flip E1 term is neglected, then there are four parameters that can be varied: the $^3S_1$ amplitude and phase and the $^1P_1$ amplitude and phase. However, the observables do not depend directly on individual phases, instead they depend on the relative phase between the transitions. Therefore, one of the phases can be fixed. Performing the fit with only this constraint yields the results shown in Table 5.4. A plot of the fit along with the data is shown in Figure 5.4.

Parameter	Value
$^3S_1$ fraction	1.6±0.2%
$^1P_1$ fraction	98.4±1.9%
$^3S_1$ phase	0° fixed
$^1P_1$ phase	12.4±2.8°

Table 5.4: TME fit with the relative phase unconstrained for 80 keV.

While this fit seems reasonable, it is found that the fit is not strongly determined. This can be understood by simplifying Equation 5.18 through Equation 5.21 assuming that the $^3P_1$ transition can be ignored. If this is done, the following relations are

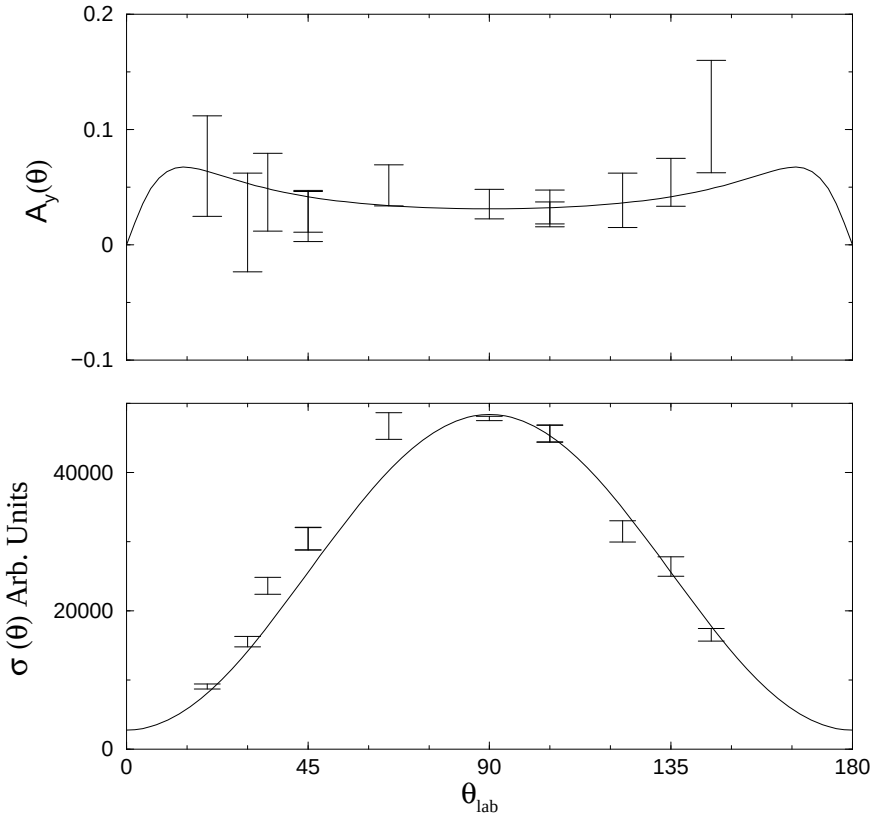

Figure 5.4: The solid lines are the result of the TME fits to the data at E_b=80 keV for the case where the phases are left unconstrained. The errors bars indicate the statistical uncertainty for the data points.

obtained:

$$\begin{aligned} A_0 &= 3(E1)^2 + 3(M1)^2 \\ a_1 &= 0 \\ a_2 &= -3(E1)^2 \\ b_1 &= -\sqrt{27}(E1)(M1)sin\delta, \\ b_2 &= = 0 \end{aligned} \tag{5.24}$$

(5.25)

where these are the Legendre coefficients and E1 ($^1P_1$) and M1 ($^3S_1$) are the TME amplitudes and δ is the relative phase between the two TMEs. Note that a_1 is identically zero here because states of different channel spins do not interfere in the cross section. Since the angular distribution of the cross section is dominated by the E1 strength ($\sin^2\theta$), only precise measurements in far forward angles and the far back angles can help extract the M1 strength (isotropic here) from the cross section. Therefore, the M1 strength must be extracted predominantly from the analyzing power. However, since the relative phase, δ, is not constrained, the two parameters, M1 and δ can be varied over a wide range to yield the same value of b_1. Therefore some additional constraint would be helpful.

One lesson that was learned in studies of the $^2H(p,\gamma)^3He$ reaction was that the Coulomb phase shifts dominate the nuclear phase shifts at these very low energies [Wul99a]. Also, it can be shown that the phases of the TMEs in capture reactions are related to the phase shifts in the associated scattering reaction at these energies [Wat54]. The $^3H(p,\gamma)^4He$ system is expected to behave in a similar manner. The nuclear phase shifts for proton scattering off tritium were found at these energies to be extremely small (less than a degree) [Hal99]. Meanwhile recalling the formula for

the relative Coulomb phase shift,

$$\sigma_l - \sigma_0 = \sum_{s=1}^{l} \arctan \frac{\eta}{s} \tag{5.26}$$

where σ is the Coulomb phase shift and η is the Sommerfeld parameter which is defined as the dimensionless quantity:

$$\eta = 31.29 \frac{Z_1 Z_2}{2\pi} \sqrt{\frac{\mu}{E_{cm}}}, \tag{5.27}$$

it is seen that the Coulomb phase shift is tens of degrees at the relevant energies. Table 5.5 summarizes the phase shifts for the beam energies used in the experiment. The phases have been computed in two different manners. Since the beam stops in the target, the Coulomb phase shift must be computed at all of the energies from the beam energy down to zero. Therefore, one approach involves computing the phase at each energy and applying the appropriate weight based on the contribution to the total yield at that energy. The weight comes from Equation 4.12. The weight is defined as follows:

$$W(E) = \frac{NL(d(E))\sigma(E)}{STP(E)} \tag{5.28}$$

where N is a normalization constant, L is the tritium loading profile as a function of depth (see Section 4.5.2), d is the depth associated with the energy E (see Equation 4.13), and σ is the cross section. The normalization constant, N, is defined such that:

$$\int_0^{\mathrm{E}_b} W(E) dE = 1. \tag{5.29}$$

As a result, the units for $W(E)$ must be inverse energy in order to cancel out with the units of dE. This weight is then multiplied by the phase shift for the energy E

E_p (keV)	$\tilde{E}_{cm}$(keV)	δ method 1	δ method 2
40	12.26	51.7 °	51.0 °
80	31.15	38.7 °	37.8 °

Table 5.5: A summary of the Coulomb phase shifts for the beam energies used in the experiment. The phases were computed at the mean energy of the beam which is also included in the table.

and integrated as follows:

$$\delta = \int_0^{E_b} W(E)\delta_c(E)dE. \tag{5.30}$$

where δ is the average phase, and δ_c is the Coulomb phase at energy E. The result is shown under the column "method 1" in Table 5.5.

The other approach simply computes the Coulomb phase at the average beam energy. Recall that the average beam energy is determined by integrating Equation 4.12 from zero up to an energy where half the total yield has been accumulated. Using the definitions from above, the average beam energy is defined as follows:

$$\int_{\tilde{E}_b}^{E_b} W(E)dE = \frac{1}{2} \tag{5.31}$$

where $\tilde{E}_b$is the average beam energy in the lab frame. The results for this method are down as "method 2" in Table 5.5. The phase shift is computed using both methods for case where E_b=40 keV and E_b=80 keV. As can be seen, the difference between the two methods is fairly small. Therefore the result from the average beam energy method will be used after rounding to the nearest degree.

Since the phase shifts are expected to be Coulomb-like at this energy, they can be used to further constrain the TME fit. After applying the Coulomb phase shift constraint, the fit results in the parameters shown in Table 5.6. A plot of the fit against the data taken at a beam energy of 80 keV is shown in Figure 5.5. Both

Parameter	Value E_p=40 keV	Value E_p=80 keV
$^3S_1$ fraction	0.44±0.28%	0.20±0.06%
$^1P_1$ fraction	99.56±0.28%	99.80±0.06%
$^3S_1$ phase (fixed)	0°	0°
$^1P_1$ phase (fixed)	51°	38°

Table 5.6: TME fit with the relative phase constrained to the value given by Equation 5.26.

fits look reasonably good. However, the case where the phase is fixed is most likely a more accurate description of the TMEs. One result of this constraint is that the M1 strength is much smaller. The magnitude of these strengths will be discussed in Section 5.5.2. A similar plot of the fit against the data taken at a beam energy of 40 keV is shown in Figure 5.6.

5.5 Comparison with theory

As was stated earlier, while much work is being done on extending theories which describe three-body systems to cases of four-body systems, this work is still in its infancy. However, some basic and well tested theoretical ideas can be used to evaluate the measurements. One model that can be tested is the direct capture model that was described in Section 2.2. Another test involves comparing the results from ^{3}H(p, γ)^{4}He and ^{2}H(p, γ)^{3}He with their mirror reactions, ^{3}He(n, γ)^{4}He and ^{2}H(n, γ)^{3}H.

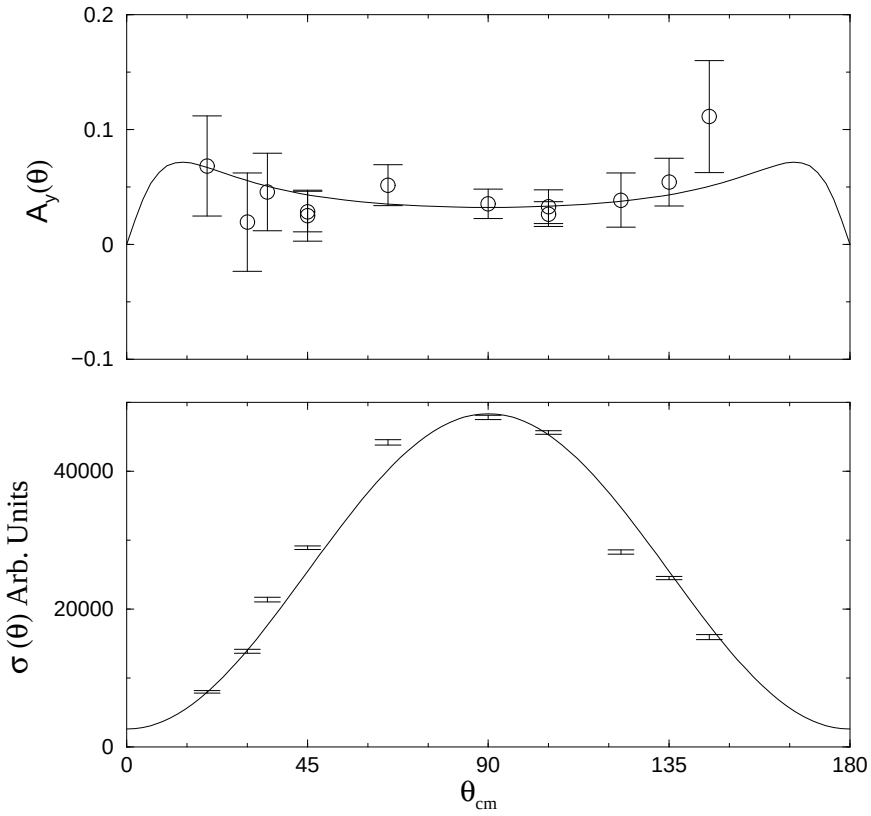

Figure 5.5: The solid lines are the result of the TME fit against the data at E_b=80 keV for the case where the phases are constrained to the Coulomb phase shift. The results are summarized in Table 5.5. The error bars indicate the statistical uncertainty for the data points.

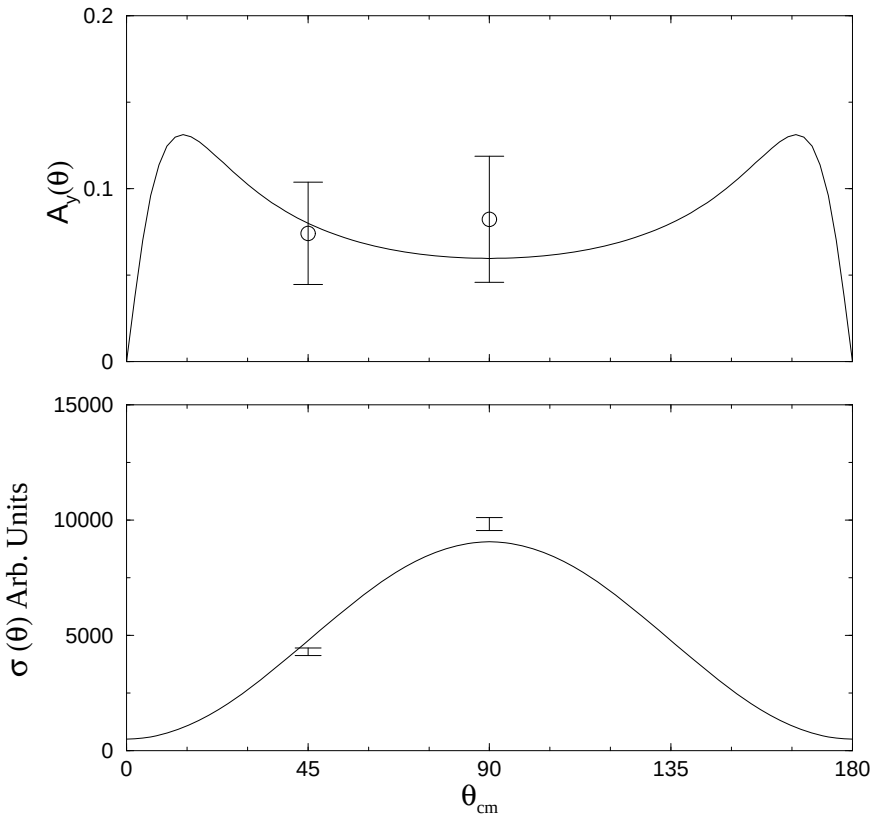

Figure 5.6: The solid lines are the result of the TME fit against the data at E_b=40 keV for the case where the phases are constrained to the Coulomb phase shift. The results are summarized in Table 5.5. The error bars include the statistical uncertainty for the data points.

5.5.1 Comparison with Direct Capture

As was mentioned in Section 2.2, the direct capture model has been very successful at describing many capture reactions. As was also pointed out, the lack of MEC effects in the model is one of its shortcomings. However, since the M1 strength has been found to be very small, the direct capture model should be able to describe the absolute cross section as well as the angular distribution of the cross section very accurately. It is worth noting that although MEC effects are not included in the M1 portion of the direct capture calculations, since the direct capture model invokes Siegert's theorem, MEC effects are included in the E1 transitions. Siegert's theorem can be derived from the continuity equation and states that in certain circumstances it is possible to replace the current operator with the charge density operator. Since the charge density operator will include the effects of MECs, these effects will be included in the determination of the electric transitions. However, the theorem cannot be used for the magnetic transitions, so the MEC effects must be explicitly added to the calculations for the magnetic transitions in order for these effects to be included.

A determination of the parameters needed for a direct capture model calculation in the present case can be performed using p-T capture measurements performed at higher energies. A summary of the parameters as well as a plot of the results are shown in Table 5.7 and Figure 5.7 respectively. There are two sets of values shown in Table 5.7. One set is the parameters for the real portion of the optical potential and the other set is the parameters for the bound state potential. Each set includes a radius parameter (r_o), a diffuseness parameter (a), a Coulomb radius parameter (r_c), and a potential strength (V). Most parameters were extracted from [Kin84]. The remaining parameters were adjusted to fit data from the current experiment and [Hah95]. The adjusted parameters are indicated in Table 5.7.

Parameter	Real Potential Value	Bound State Value
r_o	1.4 fm	0.96 fm (adjusted)
a	0.65 fm	0.66 fm (adjusted)
r_c	1.2 fm	1.2 fm
V	70 MeV (adjusted)	63 MeV

Table 5.7: A summary of the parameters used in the direct capture calculation to describe the total cross section in the $^3\mathrm{H}(\mathrm{p},\gamma)^4\mathrm{He}$ reaction. Most values were extracted from [Kin84]. Other parameters were adjusted to fit the new data as well as data from [Hah95]. The adjusted parameters are indicated in the table.

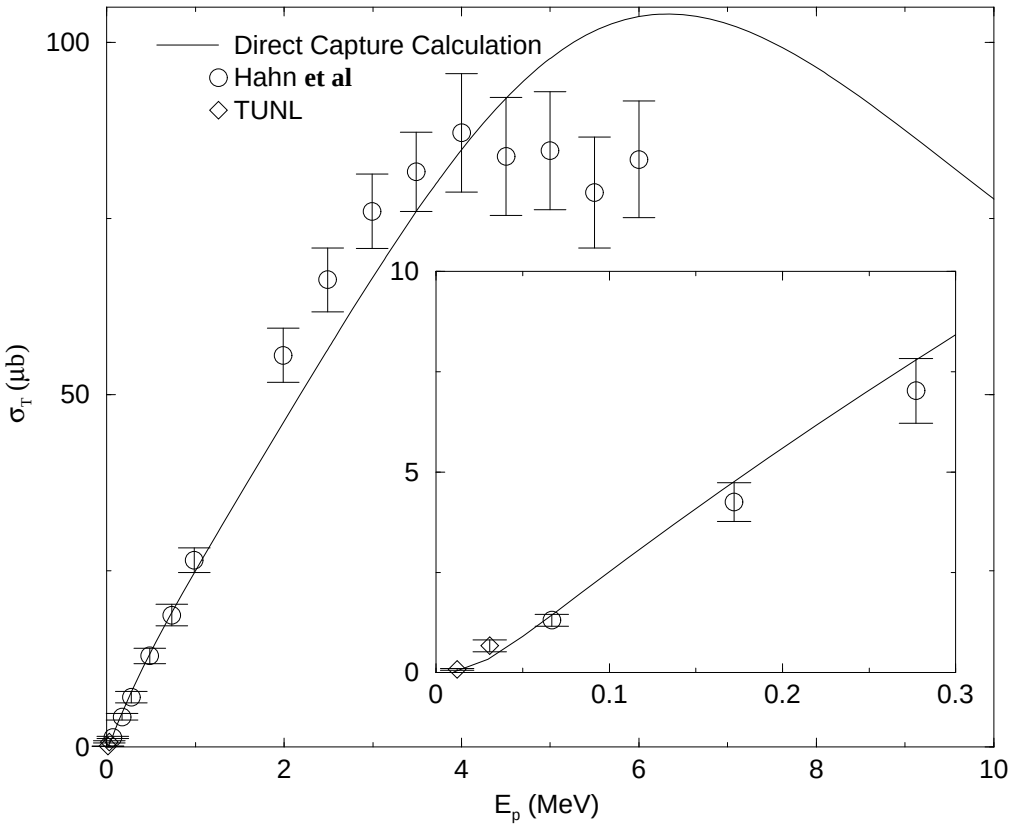

Figure 5.7: The solid line represents the result of a direct capture calculation of the total cross section as a function of the proton energy in the $^3\mathrm{H}(\mathrm{p},\gamma)^4\mathrm{He}$ reaction. The circle data points along with their uncertainties were extracted from [Hah95]. The diamond data points are from the current study. The errors bars for these data include both statistical and systematic uncertainties. The inset plot is a blow up of the low energy region. The axes, units, and data sets are the same as the larger plot.

The TME analysis in Section 5.2 indicated the presence of a small amount of M1 strength in the ^{3}H(p,γ)^{4}He reaction. Since the M1 strength is quenched for the 1-body M1 operator, the M1 strength is expected to arise mostly from 2-body currents. Since the direct capture model does not include these effects, it cannot accurately predict the M1 strength. This leads to an incorrect prediction for the analyzing power, since in this reaction the analyzing power is the result of the interference between the M1 and E1 transitions. So, although the model is successful in describing the total cross section (which is dominated by E1 radiation in the energy range shown in Figure 5.7), it fails to describe the analyzing power.

5.5.2 Comparison with Similar Reactions

Having obtained an M1 strength from the TME analysis, it is desirable to assess whether the value is reasonable and what mechanisms are contributing to its strength. Since theorists have yet to perform calculations for this reaction with current models, one must look to other reactions to determine if the value agrees with expectations.

From Table 5.6 and the cross sections determined in Section 4.5.3, it is possible to extract the absolute M1 strength at the measured energies. For example, we see that for E_b=80 keV the data indicate that the M1 strength corresponds to 0.20±0.06% of the total cross section. This corresponds to the cross section observed when stopping the 80 keV beam in the target. The effective energy for this cross section, $\tilde{E}_{cm}$, (see Equation 5.31) is 31.15 keV in the center-of-mass frame. Translating the S-factor (see Section 4.5.3) into a cross section at this energy and multiplying times the M1 fraction of the total cross section, we find an M1 cross section of 1.28±0.8 nb. The result is S_s(E_b=80 keV)= 0.005±0.003 eV b. A similar analysis of the 40 keV data gives a value of S_s(E_b=40 keV)=0.010±0.006. Since we are assuming a constant S-

factor, we average these two results together to obtain a final value of S_s=0.008±0.004 eV b.

The ^{3}He(n,γ)^{4}He reaction is a mirror reaction of the ^{3}H(p,γ)^{4}He reaction. The ^{3}He(n,γ)^{4}He reaction has been carefully studied both experimentally and theoretically, especially at thermal energies [Car90]. At these energies this reaction is essentially purely s-wave capture, due to the p-wave component vanishing as one approaches zero energy. Since the spin and parity assignments are the same as the ^{3}H(p,γ)^{4}He reaction, the s-wave capture also corresponds to an M1 transition. Also like the ^{3}H(p,γ)^{4}He reaction, the contribution from the one-body M1 operator is heavily suppressed. In fact, theoretical analysis of the ^{3}He(n,γ)^{4}He reaction has determined that the M1 strength is almost entirely ($\sim$90%) due to two-body currents (MECs) [Car90]. Obviously it would be useful to compare the extracted M1 strength for the ^{3}H(p,γ)^{4}He reaction to the M1 strength observed and calculated in this reaction. Unfortunately, because this reaction is a neutron capture reaction, it is difficult to make a simple comparison, since correctly accounting for the Coulomb effects is non-trivial. However, if there is another set of reactions that have a similar relationship then it may be possible to use this second set of reactions to relate the two four-body reactions. The ^{2}H(p,γ)^{3}He and ^{2}H(n,γ)^{3}H reactions will be used because they possess similar characteristics to the four-body reactions. For example, the product of the charges of the target and the projectile (Z_1Z_2)are the same in the three- and four-body proton capture reactions ($Z_1Z_2 = (1)(1) = 1$) and in the three- and four-body neutron capture reactions ($Z_1Z_2 = (0)(1) = 0$).

The ^{2}H(p,γ)^{3}He and ^{2}H(n,γ)^{3}H reactions have also been well studied both experimentally and theoretically. Experiments measuring the ^{2}H(p,γ)^{3}He reaction at low energies by Wulf and Schmid have already been mentioned [Sch97, Wul99b].

Similar to the ^{3}He(n,γ)^{4}He reaction, several studies of the ^{2}H(n,γ)^{3}H reaction at thermal energies have been performed [Fri90]. While the magnitudes of the s-wave (M1) portion of the p-d reaction is considerably smaller than the n-d reaction (as expected due to the Coulomb barrier), theoretical studies have determined that in each case 50% of the M1 strength is attributed to MECs.

So the course of action is as follows,

- Use the p-d and n-d capture reactions to determine the ratio of the s-wave portion of the cross section in the neutron capture reaction to the s-wave portion of the S-factor in the proton capture reaction. It is desirable to use the S-factor representation for the proton capture reactions since this representation removes the Coulomb barrier effects present in the cross section and therefore is not so rapidly changing with proton energy.
- Multiply this factor by the (s-wave) cross section in the n-^{3}He capture reaction.
- Compare the above value to the s-wave portion of the S-factor in the p-T capture reaction.

Following the procedure outlined above, the following is obtained,

$$\begin{aligned} S_s(p-t) &= \frac{S_s(p-d)}{\sigma_{thermal}(d-n)}\sigma_{thermal}(n-{}^3\mathrm{He}) \\ &= \frac{0.055\ eVb}{254\mu b}54\mu b \\ &= 0.012 \pm 0.003\ eVb. \end{aligned} \tag{5.32}$$

This agrees within error with the value extracted of 0.008$\pm$0.004 eV b.

Since the value of $S_s(p-T)$ calculated in this manner agrees with the experimentally determined value, this implies that, like the n-^{3}He capture reaction, the s-wave

capture portion of the reaction is due almost entirely (∼90%) to MECs. The fact that the three-body reactions (n-d and p-d capture) have equivalent relative MEC contributions (∼50%) at low energies also supports this assertion. In addition, it is assumed that S_s will exhibit the same constant behavior with energy that has been observed in the ^{2}H(p,γ)^{3}He reaction. This seems reasonable judging from the extracted values from the data. However, due to the large error bars in the extracted values, the present data do not, by themselves, verify this. A summary of the values used in this analysis are shown in Table 5.8.

While this is obviously not a rigorous proof of the dominance of MECs in the M1 cross section for the ^{3}H(p,γ)^{4}He reaction below 100 keV, it does demonstrate that the absolute cross sections which have been measured are consistent with the results expected based on the M1 being dominated by MEC in the ^{3}H(p,γ)^{4}He reaction. Future detailed theoretical calculations should be able to confirm this result.

Capture type	Reaction	σ or S_s-factor	Ratio
Proton capture	^{3}H(p,γ)^{4}He ^{2}H(p,γ)^{3}He	0.008±0.004 ev b 0.055±0.005 ev b [Sch97]	6.9±4.7
Neutron capture	^{3}He(n,γ)^{4}He ^{2}H(n,γ)^{3}H	54±6 μb [Car90] 254±8 μb [Fri90]	4.7±0.7

Table 5.8: Summary of low energy neutron and proton capture for three and four body systems. Thermal capture cross sections and the s-wave part of the astrophysical S-factor (S_s) are given.

Chapter 6

Conclusions

A brief summary of the important results will be presented in this chapter. Measurements of the angular distributions in the cross section and analyzing power for the ^{3}H(p,γ)^{4}He reaction at proton energies of 40 keV and 80 keV have been obtained. From these measurements, a transition matrix element (TME) analysis was performed. One result from this analysis, the absolute M1 strength, was compared with predictions for this strength based on other reactions. The comparison suggests that a dominant contribution to this strength comes from meson exchange currents. The absolute cross section for the ^{3}H(p,γ)^{4}He reaction was also measured using beams of 40 keV and 80 keV protons. A new parameterization of the astrophysical S-factor was obtained from these data. The lack of any theoretical results from modern techniques and potentials for this reaction prohibits a detailed comparison with theoretical results.

6.1 Discussion of Results

This study measured the absolute cross section of the ^{3}H(p,γ)^{4}He reaction lower in energy than any other previous study. Measuring a charged particle capture reaction at such a low energy (E_p=40 keV) is rare, due to the rapid drop in the cross section caused by the Coulomb barrier. Extracting the absolute cross section and the astrophysical S-factor from the measured yields required some careful consideration. Since the beam stops within the target, the yields represent the range of energies from the beam energy down to zero. Since the cross section was not constant with energy, the absolute cross section could not simply be factored out of the yields. Instead it was necessary to fold in the data from previous measurements to determine the energy dependence of the cross section. Even this folding procedure had to be done with careful consideration, since some of the previous measurements were also performed at low energies. The implication being that changing the expected low energy behavior of the cross section from what was determined in a previous study could affect the interpretation of the previous results. Table 4.4 summarizes the results of various approaches to determining the parameterized S-factor.

The angular distributions in the cross section and analyzing power were determined at 40 keV and 80 keV and a Legendre polynomial expansion of these data was performed. The expansion of $\sigma(\theta)$ only required terms up to $k = 2$. This was expected since higher l-values (and hence higher order (k) Legendre polynomials) are generally suppressed at low energies by the angular momentum barrier. In addition, it was found that excluding the $k = 1$ term lowered the χ^2 per degree of freedom. This result confirmed the expectation that the spin-flip E1 transition was heavily suppressed, since this transition would likely result in a noticeable $k = 1$ term in

the Legendre expansion as well as a $k = 2$ term (finite b_2) in the expansion of the analyzing power. So the only significant terms in the expansion of $\sigma(\theta)$ were the a_0 and a_2 terms. For $A_y(\theta)$, it was found that only the b_1 term was needed. Including the b_2 term did not dramatically improve the fit, and including terms beyond $k = 2$ was found to be statistically unjustified.

A TME analysis on the angular distributions of the cross section and analyzing power at 40 keV and 80 keV was performed. The angular distribution in the cross section for this reaction has a $A + B\sin^2\theta$ form. The constant portion comes from s-wave (M1) capture, while the $\sin^2\theta$ form comes from p-wave (E1) capture. Since the s-wave capture strength is extremely small (less than 1%) the underlying constant portion of the angular distribution is difficult to measure. This would require detectors to be placed at the extreme forward and back angles where the yield is very small. Furthermore, the detectors would need to be heavily collimated which would further reduce the count rate. It is for this reason that measuring the analyzing power was so effective. Since the analyzing power at θ=90°measures interference between transitions with opposite parity, a weak transition of opposite parity can be amplified by a stronger transition. In the case of the $^3\mathrm{H}(\mathrm{p},\gamma)^4\mathrm{He}$ reaction, the weak M1 transition interferes with the strong E1 transition to create an analyzing power at 90°that can be accurately measured. The analyzing power at 90°can be stated as,

$$A_y(90^\circ) = \mathrm{E1M1}\sin\delta, \tag{6.1}$$

where E1 and M1 are the transition amplitudes and δ is the relative phase between the transitions. Determining the relative phase directly from the data would require some determination of the M1 strength from the angular distribution in the cross section. This is difficult since it requires precise measurements at forward and back angles. However, previous studies of other capture reactions at low energies have indicated

that the relative phase can be determined to a reasonable accuracy by computing the Coulomb phase shift.

Perhaps the most interesting result from this study is the extracted s-wave capture strength and its implications for the presence of meson exchange currents(MEC). A prediction of the s-wave portion of the S-factor of 0.012±0.003 eV b based on the mirror reaction, ^{3}He(n, γ)^{4}He, agrees well with the value extracted from the data of 0.008±0.004 eV b. Furthermore, theorists have concluded that nearly all of the s-wave capture in the ^{3}He(n, γ)^{4}He reaction is due to MEC effects. The ^{3}H(p, γ)^{4}He reaction is expected to behave in a similar manner, and these results support that expectation. The good agreement found here also lends credibility to the absolute cross section results for the entire reaction, since they are used in obtaining this result.

At this time there are no detailed four-body theoretical results to compare these results against. However, theorists are actively studying four-body nuclear systems. Rigorous calculations of the alpha particle binding energy with realistic nucleon-nucleon (NN) potentials have been performed [Pud97, Cie98]. In addition, scattering reactions such as n-^{3}He and p-^{3}He have been studied with realistic NN potentials [Cie98, Viv98, Fon99]. Some of these studies have already resulted in important findings. The calculations detailed in [Pud97] were able to reproduce the α-particle binding energy without requiring four-body forces. In contrast, the need for a three body force was first demonstrated by similar calculations performed on 3-body bound states. The studies of the bound state and scattering states have employed a variety of approaches, such as: using the Green's function Monte Carlo algorithm, solving the Faddeev-Yakubovsky (FY) equations for four nucleons, using the Kohn variational principle, or solving the Alt, Grassberger, and Sandhas (AGS) equations. While each approach has achieved some success, certain difficulties have arisen. Some of

these difficulties may affect the potential success for an approach in describing the $^3\mathrm{H}(\mathrm{p},\gamma)^4\mathrm{He}$ reaction. For example, in both the FY and AGS methods, properly dealing with the Coulomb term could pose problems. For this reason, perhaps the most promising approach appears to be the Kohn variational method. The success of this method in reproducing data from p-d capture studies bolsters this expectation.

6.2 In Closing

The results from this study of the $^3\mathrm{H}(\mathrm{p},\gamma)^4\mathrm{He}$ reaction should provide some solid testing ground for developing four-body theoretical methods. The reaction should be useful in gauging the potential success of new models and techniques. The explicit results on the M1 cross section require a detailed four-body calculation which includes MEC effects. The lack of open channels in the energy region of this study should make this an appealing test case for examining the capture mechanisms within a possible theory. In addition, the results from this study should be especially useful for examining the handling of Coulomb related effects in new theories and techniques. Theoretical work on four-body systems is advancing quickly and, hopefully, the full benefit of this study will soon be realized.

Bibliography

[And77] H. H. Andersen and J. F. Ziegler. *Hydrogen Stopping Powers and Ranges in All Elements*, volume 3 of *The Stopping and Ranges of Ions in Matter*. Pergamon Press, New York, 1977.

[BH71] H. H. Barschall and W. Haeberli, editors. *Polarization Phenomena in Nuclear Reactions*, page xxv. University of Wisconson Press, Madison, Wisconsin, 1971.

[Bri68] D. M. Brink and G. R. Satchler. *Angular Momentum*. Clarendon Press, 2nd edition, 1968.

[Bro87] R. E. Brown, N. Jarmie, and G. M. Hale. Phys. Rev. C, **35**(1987) 1999.

[Cal83] J. R. Calarco, B. L. Berman, and T .W. Donnelly. Phys. Rev. C, **27**(1983) 1866.

[Car90] J. Carlson, D. Riska, and R. Schiavilla. Phys. Rev. C, **42**(1990).

[Cie98] F. Ciesielski and J. Carbonell. Phys. Rev. C, **58**(1998) 58.

[Coe83] H. T. Coelho, T. K. Das, and M. R. Robilotta. Phys. Rev. C, **28**(1983) 1812.

[Coo79] S. A. Coon, M. D. Scadron, P. C. McNamee, et al. Nucl. Phys., **A317**(1979) 242.

[Fad60] L. D. Faddeev. Zh. Eksp. Teor. FIz., **39**(1960) 1459.

[Fer65] A. J. Ferguson. *Angular Correlation Methods in Gamma-Ray Spectroscopy*. John Wiley & Sons, New York, 1965.

[Fon99] A. C. Fonseca. PRL, **83**(1999) 4021.

[Fow67] W. A. Fowler, G. R. Caughlan, and B. A. Zimmerman. Ann. Rev. Astronomy and Astrophysics, **6**(1967) 525.

[Fri90] J. L. Friar, B. F. Gibson, and G. L. Payne. Phys. Lett., **B251**(1990) 11.

[Fri91] J. L. Friar, B. F. Gibson, H. C. Jean, and G. L. Payne. Phys. Rev. Lett., **66**(1991) 1827.

[Gam28] G. Z. Gamow. Z. Phys, **51**(1928) 204.

[Hah95] K. I. Hahn, C. R. Brune, and R. W. Kavanagh. Phys. Rev. C, **51**(1995) 1624.

[Hal99] G. M. Hale, 1999. Private Communication.

[Hüb98] D. Hüber and J. L. Friar. Phys. Rev. C, **58**(1998) 674.

[Kie93] A. Kievsky, M. Viviani, and S. Rosati. Nucl. Phys., **A551**(1993) 241.

[Kie94] A. Kievsky, M. Viviani, and S. Rosati. Nucl. Phys., **A557**(1994).

[Kie95] A. Kievsky, M. Viviani, and S. Rosati. Phys. Rev. C, **52**(1995) R15.

[Kie96] A. Kievsky, S. Rosati, W. Tornow, and M. Viviani. Nucl. Phys., **A607**(1996) 402.

[Kie99a] Kievsky, 1999. Private Communication.

[Kie99b] A. Kievsky. Phys. Rev. C, **60**(1999) 34001.

[Kin84] S. E. King. Ph.D. thesis, Duke University, 1984.

[Knu99] L. D. Knutson. Phys. Rev. C, **59**(1999) 2152.

[Laf82] J. M. Lafferty and S. R. Cotanch. Nucl. Phys., **A373**(1982) 363.

[Leo94] W. R. Leo. *Techniques for Nuclear and Particle Physics Experiments.* Springer-Verlag, second revised edition, 1994.

[McA94] J. E. McAninch, L. O. Lamm, and W. Haeberli. Phys. Rev. C, **50**(1994) 589.

[McC68] I. E. McCarthy. *Introduction to Nuclear Theory.* John Wiley and Sons, Inc., 1968.

[Men96] A. J. Mendez, C.D. Roper, J. D. Dunham, and T .B. Clegg. Rev. Sci. Instrum., **67**(1996).

[Nel85] W. R. Nelson. *EGS4 User Manual*, 1985.

[Pay86] G. L. Payne. *Faddeev Equations for Bound and Scattering States.* In *Theoretical and Experimental Investigations of Hadronic Few-Body Systems*, page 53, 1986.

[Per55] J. E. Perry and S. J. Bame Jr. Phys. Rev., **99**(1955) 1368.

[Phi87] R. J. Philpott. NIM, **A259**(1987) 317–323.

[Poo91] A. W. P. Poon. Ph.D. thesis, The University of British Columbia, 1991.

[Pud97] B. S. Pudliner et al. Phys. Rev. C, **56**(1997) 1720.

[Rol77] C. Rolfs. Nucl. Phys., **A217**(1977) 29.

[Rol88] C. E. Rolfs and W. S. Rodney. *Cauldrons in the Cosmos.* University of Chicago Press, Chicago, 1988.

[Ros53] M. E. Rose. Phys. Rev., **91**(1953) 610.

[Roy67] R. R. Roy and B. P. Nigam. *Nuclear Physics.* Wiley, 1967.

[Sch37] L. I. Schiff. Phys. Rev., **52**(1937) 242.

[Sch97] G. J. Schmid, B. J. Rice, R. M Chastler, M. A. Godwin, G C. Kiang, L. L. Kiang, C. M. Laymon, R. M. Prior, D. R. Tilley, and H. R. Weller. Phys. Rev. C, **56**(1997) 2565.

[Sey79] R. G. Seyler and H. R. Weller. Phys. Rev. C, **20**(1979) 453.

[Sha80] R. Shankar. *Principles of Quantum Mechanics.* Plenum, 1980.

[Shi95] S. Shimizu, H. Nakamura K. Sagara, K. Maeda, T. Miwa, N. Nishimori S. Ueno, T. Nakashima, and Morinobu. Phys. Rev. C, **52**(1995) 1193.

[Tor83] J. Torre and B. Goulard. Phys. Rev. C, **28**(1983) 529.

[Tor98] W. Tornow and H. Witala. Nucl. Phys., **A637**(1998) 280.

[Ver50] M. Verde. Helv. Phys. Acta, **23**(1950) 453.

[Viv96] M. Viviani, R. Schiavilla, and A. Kievsky. Phys. Rev. C, **54**(1996) 534.

[Viv98] M. Viviani, S. Rosati, and A .Kievsky. PRL, **81**(1998) 1580.

[Wat54] K. M. Watson. Phys. Rev., **95**(1954) 228.

[Wel82] H. R. Weller et al. Phys. Rev. C, **25**(1982) 2921.

[Wir95] R. B. Wiringa, V. G. J. Stoks, and R. Schiavilla. Phys. Rev. C, **51**(1995) 38.

[Wul99a] E. A. Wulf. Ph.D. thesis, Duke University, 1999.

[Wul99b] E. A. Wulf et al. Phys. Rev. C, **61**(1999) 61.

[Yak67] O. A. Yakubowsky. Sov. J. Nucl. Phys, **5**(1967) 937.

Biography

Richard Shane Canon

Personal

- Born in Fort Leonardwood, MO on August 15, 1971

Education

- B.S. Physics, Auburn University Auburn, Alabama, 1993
- A.M. Physics, Duke University, Durham, North Carolina, 1997

Positions

- Teaching Assistant, Duke University, 1994-1996
- Research Assistant, Duke University, TUNL, 1995-1999

Publications

Direct determination of the doublet and quartet M1 cross sections in p-d radiative capture at near-thermal energies
B. J. Rice *et al.* Phys. Rev. C, **56**(1997) 2917.

Gamma-ray Production in a Storage Ring Free-Electron Laser
V. N. Litvinenko *et al.* Phys. Rev. Lett. **78** (1997) 4569

First Measurement of the Near-threshold $^2H(\vec{\gamma},n)p$ Analyzing Power using a Free-Electron Laser Based Gamma-ray Source
E. C. Schreiber, *et al.* Phys. Rev. C, **61** (2000) 61604

Two-deuteron photodisintegration of ^4He at E_γ = 150-250 MeV
B. J. Rice *et al.* Phys. Rev. C, **61** (200) 64612